UNIVERSITAT POLITÈCNICA DE CATALUNYA

Risk Managment of Complex Aquifers Contaminated by Chemical Mixtures:

Numerical Tools and Human Health Risk Assessment

by

Christopher V. Henri

Advised by Dr. Daniel Fernàndez-Garcia

A thesis submitted to the doctoral school of the
Universitat Politècnica de Catalunya
in partial fulfillment for the degree of Doctor of Philosophy

in the

Department of Geotechnical Engineering and Geo-Sciences

Grup d'Hidrologia Subterrània
UNIVERSITAT POLITÈCNICA DE CATALUNYA

"L'art est fait pour troubler. La science rassure."

"Art is made to disturb. Science reassures."

Georges Braque

UNIVERSITAT POLITÈCNICA DE CATALUNYA

Abstract

Department of Geotechnical Engineering and Geo-Sciences

Doctor of Philosophy

by Christopher V. Henri

Human impact on groundwater resources has led to a rapid growth of social concerns worldwide owing to an increasing presence of toxic chemicals released in the subsurface. Risk assessment provides the scientific tool needed to quantify the actual thread that these potential hazards pose to human health. Specifically, risk analysis enables decision makers to answer: What can happen? How likely is it to happen? What can be the consequences? Risk assessment is in this context essential. However, modeling efforts involve in risk analysis are still facing several problems. Among them, in some cases, degradation products can constitute new noxious chemical compounds not necessarily less toxic than their parent product. Thus, the original pollutants and their daughter products are susceptible to co-exist in the aquifer forming a hazardous chemical mixture composed of products of different toxicity. This renders the quantification and interpretation of human health risk a non-trivial and challenging task. Also, the lack of information in the hydraulic and biochemical properties renders transport predictions to be highly uncertain. Stochastic human health risk assessment incorporates hydrogeological uncertainty in human health predictions. This way, probabilistic risk models can be used to determine the likelihood of risk exceeding a given regulatory threshold value or the expected threat to the exposed population and its uncertainty. Unfortunately, these approaches are very computationally demanding. Moreover, the diverse mineralogical composition of a real soil and the complex spatial variability of aquifer properties can produce a mixture of rates of mass transfer between regions of mobile and immobile contaminants. This calls for more sophisticated or alternative transport models such as those that conceptualize the porous medium as a multi-porosity system. Finally, risk predictions are typically challenged by the complexity of the source zone condition. Dense non-aqueous dense

liquids illustrate perfectly this complexity by causing a slow release of contaminants into the aquifer according to a depletion rate that strongly depends on the architecture of the source zone.

Existing reactive transport models based on Eulerian methods still undergo computational burden and numerical problems when modeling strong hydro-biochemical heterogeneities with complex reactions in multi-porosity systems. In this context, Particle Tracking Methods constitute a feasible alternative but these methods are limited in the range of applicability. The work presented in this thesis proposes an efficient particle tracking solution capable to simulate serial-parallel degradation reactions in multiple porosity systems with rate-limited mass transfer and strong heterogeneities. The approach is based on the development of transition probabilities that describe the probabilities that particles belonging to a given state (species and mobile/immobile region) at a given time will be transformed into another state in a later time. The method is then used to characterize the human health risk posed by chemical mixtures in highly heterogeneous porous media under complex source zone conditions. In particular, we systematically investigate the interaction between aquifer heterogeneity, connectivity, contaminant injection mode and chemical toxicity in the probabilistic characterization of health risk. We illustrate how chemical-specific travel times control the regime of the expected risk and its corresponding uncertainties. Results indicate conditions where preferential flow paths can favor the reduction of the overall risk of the chemical mixture. The overall human risk response to aquifer connectivity is shown to be non-trivial for multi-species transport. This non-triviality is a result of the interaction between aquifer heterogeneity and chemical toxicity. To quantify the joint effect of connectivity and toxicity in health risk, we propose a toxicity-based Damköhler number. Furthermore, we provide a statistical characterization in terms of low-order moments and the probability density function of the individual and total risks. Results also show that the degradation capacity of immobile water regions and the mass depletion model can play a significant role on the spatiotemporal behavior of the contaminant mixture. Our work also highlights the potential impact of the water flux passing through the source zone on the effective increased lifetime cancer risk due to a reactive chemical mixture. Counter-intuitively, the source zone efficiency is shown to have a beneficial effect on the risk. The total risk tends indeed to decrease for high source zone efficiency due to the consequential decrease in travel times near the source zone, which may limit the production of highly toxic daughter products.

UNIVERSITAT POLITÈCNICA DE CATALUNYA

Resumen

Departamento de Ingeniería del Terreno, Cartográfica y Geofísica

por Christopher V. Henri

El impacto humano sobre los recursos hídricos que forman los acuíferos es actualmente una de las grandes preocupaciones sociales en crecimiento debido a la presencia antrópica cada vez mayor de productos químicos tóxicos liberados en el subsuelo. El análisis de riesgo proporciona la herramienta científica necesaria para cuantificar el peligro real que estos contaminantes suponen para la salud humana. En concreto, el análisis de riesgo permite tomar decisiones que respondan a las siguientes preguntas: Qué puede pasar? Qué tan probable es que suceda? Cuál pueden ser las consecuencias? El análisis de riesgo es una herramienta clave en este sentido. Sin embargo, los esfuerzos de modelación necesarios para llevar a cabo el análisis de riesgo se enfrentan con varios problemas. Entre ellos, algunos productos tóxicos de degradación pueden constituir nuevos compuestos químicos nocivos no necesariamente menos tóxico que su producto padre. Por lo tanto, los contaminantes originales y sus productos hijos son susceptibles de coexistir en los acuíferos formando una mezcla de compuestos químicos de diferente toxicidad. Esto hace que la cuantificación e interpretación del riesgo para la salud humana sea una tarea no trivial y desafiante. Por otra parte, la falta de información en las propiedades hidráulicas y bioquímicos hace que las predicciones sobre el comportamiento de dichos contaminantes en el subsuelo sean altamente inciertas. El análisis de riesgo estocástico incorpora de forma natural la incertidumbre hidrogeológica que existe en las predicciones de riesgo para la salud humana. De esta manera, estos modelos pueden ser utilizados para determinar la probabilidad de que el riesgo supere un valor umbral o el valor esperado del riesgo y su incertidumbre. Desafortunadamente, estos enfoques son muy exigentes en tiempo de cálculo. Además de estas dos problemáticas, también se tiene que tener en cuenta que la composición mineralógica de un suelo real es diversa y variable en el espacio. Muchas veces esto implica la transferencia de masa entre zonas de contaminantes móviles e inmóviles.

Esto ltimo exige modelos sofisticados de transporte que, por ejemplo, conceptualicen el medio poroso como un sistema multi-porosidad. Finalmente, la complejidad que existe en el comportamiento del foco de contaminación hace complicado un análisis de riesgo. Los líquidos tóxicos densos y no acuosos ilustran perfectamente esta complejidad. Una vez en el subsuelo, estos líquidos liberación lentamente los contaminantes dentro del acuífero de acuerdo con una tasa de agotamiento que depende fuertemente de la arquitectura errática del foco de contaminación.

Los modelos de transporte reactivo Eulerianos tienen problemas numéricos cuando se simulan fuertes heterogeneidades hidro-bioquímicos en el terreno al mismo tiempo que reacciones químicas complejas en sistemas multi-porosidad. En este contexto, los métodos de trayectorias de partículas constituyen una alternativa viable. Sin embargo, estos métodos pueden tener en cuenta un rango pequeo de reacciones químicas. El trabajo presentado en esta tesis propone una solución a estos problemas mediante un método de trayectoria de partículas. El método es eficiente y capaz de simular cadenas y redes de degradación en sistemas heterogéneos con porosidad mltiples. El método se basa en el desarrollo de probabilidades de transición que describen las probabilidades de que las partículas que pertenecen a un estado determinado (producto químico y región móvil / inmóvil) en un momento dado se transformará en otro estado en un momento posterior. El método se utiliza para caracterizar el riesgo para la salud humana que representan las mezclas de degradación en medios porosos altamente heterogéneos derivados de focos de contaminación complejos. En particular, se investiga la interacción entre la heterogeneidad, la conectividad, el modo de inyección de los contaminantes y su toxicidad química con respecto a la caracterización probabilística del riesgo para la salud humana. Los resultados indican las condiciones mediante las cuales las vías de flujo preferencial pueden favorecer la reducción del riesgo para la salud humana. La dependencia de la conectividad con el riego se demuestra que no es nada trivial cuando se trata de mezclas de compuestos químicos. Esta no trivialidad es el resultado de la interacción entre la heterogeneidad del acuífero y la toxicidad de los compuestos químicos. Para cuantificar el efecto conjunto de la conectividad y la toxicidad en el riesgo para la salud, se propone un nmero de Damköhler nuevo que tiene en cuenta la toxicidad. Además, el riesgo también se caracteriza en términos estadísticos mediante momentos de bajo orden y funciones de densidad de probabilidad. Los resultados también muestran que tanto la capacidad de degradación de zonas inmóviles como los modelos existentes de agotamiento del foco pueden desempear

un papel muy significativo en el análisis espacio-temporal del riesgo. Este trabajo también muestra que la eficiencia del foco de contaminación para concentrar el flujo puede tener un efecto beneficioso sobre el riesgo. El riesgo total de hecho tiende a disminuir para eficiencias grandes debido a la disminución consecuente en tiempos de viaje cerca del foco de contaminación, limitando la producción de productos de degradación más tóxicos.

Acknowledgements

Now that these four beautiful years of work (and so much more) have passed, many people are to be thanked and I would first of all like to apology for any oversight. How to not start by deeply acknowledging my advisor Daniel Fernàndez-Garcia. Literally none of the following pages would have been possible without his support since the very first days, his precious advises and his brilliant mind. His never-ending patience and cheerfulness despite the countless hours of work are still surprising me today. It would in fact have been impossible for me to find a better supervisor than Dani and I am forever grateful for having been his student.

During the two last years, I had the chance to work with Felipe de Barros that became a precious collaborator, helping me on a large part of this thesis. More importantly, Felipe became also a great friend. I wish that we could have jammed more often, me trying to follow his guitar riff. I would like to thank him for all the kind support and for giving me the opportunity to work in his research group at the University of Southern California. This experience in the crazy city of Los Angeles is unforgettable for me.

I would like furthermore to deeply acknowledge all the members, past and present, of the Hydrogeology Group. I grown up there as a researcher and it has been a pleasure to spend these years surrounded by such interesting and stimulating persons. While thinking back about the group, I must particularly acknowledge Teresa for all the precious help since my arrival in Barcelona. I had the chance to meet wonderful friends at UPC. Daniele, Francesca and many others, I will miss these moments celebrating the bright days and discussing the darker ones. Thanks to all of you.

À ma famille. Maman, si j'en suis où j'en suis aujourd'hui, c'est peut-être dû à la chance, peut-être à une certaine forme de mérite, si mérite il existe, mais c'est certainement grâce à toi. Tu nous a guidé à travers bien des tempêtes. Vincent, Stéphanie, Marie, il y a peu de mots pour dire ce que je vous dois. Ces pages sont écrites parce que vous êtes et avez toujours été là pour moi. Merci pour tout.

I thank Maria for having made these four years such a beautiful adventure, for her unconditional support and for making the future look so bright.

Contents

List of Figures

List of Tables

Abbreviations

BTC	Breakthrough curve
CBTC	Cumulative breakthrough curve
CD	Constant displacement
CIM	Classical injection mode
CP	Control plane
CPF	Cancer potency factor
CPU	Central processing unit
DCE	Dichloroethylene
DNAPL	Dense non-aqueous phase liquid
EPA	(United States) Environmental Protection Agency
FWIM	Flux-weighted injection mode
GTP	Ganglia To Pool
ILCR	Increased lifetime cancer risk
NRMSD	Normalized root mean square deviation
MCL	Maximum contaminant level
ODE	Ordinary differential equations

PCE	Perchloroethylene or Trichloroethylene
PDF	Probability density function
PTM	Particle tracking methods
RAM	Random-access memory
RME	Relative mass (discharge) error
TCE	Trichloroethylene
VC	Vinyl chloride

À ma mère, mon frère, mes soeurs.
Til Maria.

Context and Objectives

Groundwater Contaminations. The groundwater resource, largest volume of readily accessible fresh water on Earth, is an essential factor of societies stability by securing water supplies in a large portion of the globe [UNESCO, 2012]. However, in a context of quantitatively limited natural resources, always increasing world population and past lack of environmental consciousness, the pressure that human societies have imposed to its groundwater led to important environmental and public health issues. Indeed, the resource is currently presenting a worrying qualitative state in many inhabited areas despite a relatively late industrialization of human societies. To date, no less than 342,000 sites has been estimated to be contaminated across the European Union [Panagos et al., 2013] (see Figure 1 for more detailed numbers about groundwater contamination in the E.U.). Aquifer contamination presents a wide variety of origin, from noxious agricultural practice (e.g. nitrate or pesticides), insecure landfills (e.g. chlorinated solvents), uncontrolled hazardous waste sites or leakage of sub-products from the nuclear industry. Issues related to the deterioration of the groundwater state are therefore numerous and public concerns are widely increasing with the advances in the resource qualitative characterization. Moreover, the groundwater, being in permanent motion, represents a particularly efficient vector of pathogens or toxic agents from an isolated contaminated site toward human populations [World Health Organization, 2006].

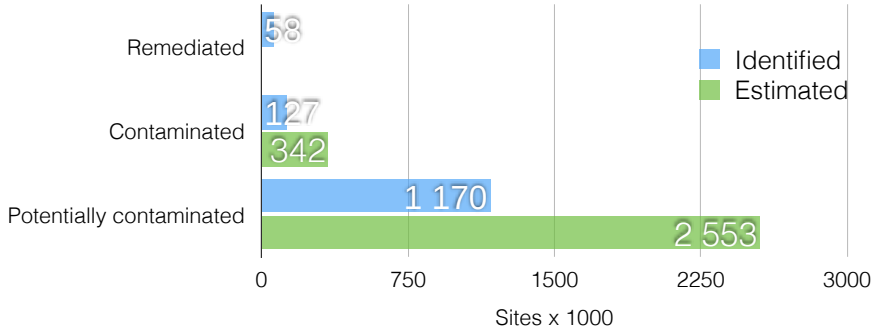

FIGURE 1: Number of remediated, contaminated and potentially contaminated sites in the European Union based on identification and estimation (from Panagos et al. [2013]).

Risk Management. As a response to this threat, regulators and hydrogeologists have contributed since few decades to the elaboration of a large arsenal of legislative and scientific tools aiming to minimize the risk posed by groundwater on the human health while preserving an acceptable cost-efficiency in the contamination monitoring. A large number of the pre-cited contamination cases leads to a serious degradation of groundwater quality over decades. In this context, the importance of a predictive effort is primordial for engineers to limit the long-term harmful consequences of a groundwater contamination. This need coupled to the impressively rapid development and democratizing of computer technologies makes that the numerical modeling of biochemical reaction and transport of solute contaminants into aquifers is taking an ever increasing importance in the decision-making process. The risk for a given human population to develop diseases from the ingestion, inhalation or dermal exposures to a predicted amount of contaminant can then be evaluated. This evaluated risk can then serve as a base for decision makers to adapt the aquifer decontamination strategy to socioeconomic constraints. We can therefore distinguish two key steps of a risk management: (1) the prediction of the contaminant evolution in time and space, and (2) the quantification of the consequences on the human health of an exposure to this contaminant leading to a decision making.

Complexity. This two-step process hides unfortunately a highly complex set of interdependence between physical, biochemical, toxicological, physiological and societal parameters. This need for a multiprocess analysis makes risk management a perfect example of

the necessary integration of the concept of *complex thinking* in environmental sciences, which makes the interlinking between disciplines a norm to face future challenges [Morin, 1990]. Among the multiplicity of key processes complexifying the spatiotemporal propagation of human health risk in aquifers, two can been highlighted as significant controlling factors: the chemical, biochemical or physicochemical reactions of contaminants and the heterogeneities in the hydraulic properties of the porous media.

Chemical Mixtures. A significant number of polluting agents are chemically and/or biologically reactive in the subsurface. Moreover, many reactive (bio)chemical processes such as the radioactive decay, the reductive dechlorination of chlorinated organic compounds, the oxidative pathway of pesticide and the sequential nitrate reduction consists in the isotopic or molecular transformation of an original contaminant into one or a series of subspecies. Both parent species and transformation product(s) are then susceptible to coexist in the porous media to form what one could call a *chemical mixture*. The risk posed by an exposure to this chemical mixture is controlled by a series of species-dependent reaction rates and toxicities that will complicate significantly both the reactive transport modeling and the spatiotemporal prediction of the effective risk that the multispecies contamination may pose to the human health.

Heterogeneity. On the other hand, the locally specific physico- and bio-chemical conditions and the heterogeneity in the hydraulic properties of the aquifer [Dagan, 1989] render spatial variability a highly controling factor of groundwater contamination spatiotemporal evolution. Dealing with heterogeneous hydraulic properties is particularly challenging owing to its intrinsic multiscale nature and complex characterization. Observed from the scale of lithological formations to the scale of pores organization, heterogeneities are shown to favor the development of a complex network of high velocity channels, areas of low water flow, and even zones of near-zero flow where only diffusive processes effectively occurs. This complex spatial distribution of water velocities will impact significantly the focus and spread of the transported contaminant plume(s), and by consequent the risk posed to the exposed population.

Conceptualization. Contaminated hydrogeological systems carry therefore divers degrees of complexity that makes the representation of *reality* barely thinkable. Our engineering field seeks to face these scientific and societal challenges by proposing useful and

accurate tools to the civil society. The conceptualization of the problem is the cornerstone of this task. One could define engineering as a rigorous art of conceptualization, whom reaching the highest degree of simplification while conserving accuracy in the analysis conclusions is the goal. Both concepts of porous media heterogeneities and biochemical reactions have been subject to an important effort of conceptualization by our scientific community.

Heterogeneity representation. In a modeling purpose, it is convenient to account for the heterogeneity in the hydraulic conductivity by discretizing the problem into a number of cells whom the spatial organization of their specific hydraulic properties will follow a pre-characterized lithology. However, incorporating this certain degree of complexity in the treatment of hydrogeological problems implies often to accept facing and quantifying uncertainties [Gómez-Hernández, 2006]. Indeed, the full characterization of the spatial distribution of the hydraulic conductivity at the model grid-size resolution is technologically untreatable and, even imagining an utopian advancement of characterization techniques, the enormous allocation of economical resources that it would require would have great chances to make the task societally unacceptable. In this context, quantifying the uncertainty made on this conceptual representation and on the consequential risk estimation can seem the wiser strategy to adopt. Stochastic approaches emerged then to propose the description of aquifer systems by a series of equiprobable scenarios respecting relatively characterizable properties and suspected spatial correlation [Rubin, 2003].

However, even described stochastically, the finite discretization of hydraulic properties integrate inevitably heterogeneities at smaller scale than the grid-cell size. While the methods developed to solve this upscaling problem focused successfully on flow representation, their application highlighted the partial inadequacy of the classic advection-dispersion equation to model solute transport. Fitted transport parameters failed indeed to reproduce late time contaminant arrivals taking because of the slow diffusion of mass from and into non-represented small-scale zones of very low or near-zero velocity. More sophisticated conceptual models of solute transport emerged subsequently coupling a diffusive mass transfer from/into "immobile" zones to the advection-dispersion model [Haggerty and Gorelick, 1995; Carrera et al., 1998].

This significant effort of conceptualization achieved great success to assess the risk posed by single non-reactive contaminants but a void exists in the consideration of multispecies

reactive contamination in such complex aquifers.

Biochemical Models. Regarding the actual state of the field, our capacity to couple "physically complex" aquifers to "biochemically complex" reactive systems in an accurate manner passes also by a strong conceptual simplification of the biochemical problem. The accuracy of a numerical method passes by its numerical stability and an algorithm efficiency making the model applicable. The pre-discussed stochastic description of the hydraulic properties involves significant computational efforts and makes the efficiency of the reactive transport model a particularly important aspect of its applicability. Highly complex biochemical reactive systems has been satisfactorily simplified by empirical models such as the Michaelis-Menten model for enzyme kinetics or the Monod model for microorganisms growth. However, their application in stochastic modeling of complex aquifer systems may render the task certainly interesting in a theoretical sense, but also highly time-consuming and therefore poorly applicable for engineering purposes. On the other hand, the approximation of biochemical reactions by a simplified first-order decay is frequently used by stakeholders to represent complex network of interacting chemicals. This approach has several advantages such as the limitation of the number of parameters and the linearity conservation of the ordinary differential equation systems that is often synonymous with a great efficiency in the solving process while preserving the most important features of the problem.

Random Walk Particle Tracking. Envisaging a stochastic modeling and risk assessment of such complex systems passes by the development of highly efficient numerical method capable to simulate simplified reaction network in aquifers presenting multiscale heterogeneities while preserving trustable predictions. A large diversity of numerical methods exists to model multispecies reactive systems. However, their application in finely discretized and three-dimensional heterogeneous porous media shows a relatively poor efficiency and numerical issues that can make the prediction misleading. Random walk particle tracking approaches have demonstrated to be a powerful alternative presenting a high computational efficiency and solution stability even for models with millions of grid cells [Salamon et al., 2006b].

Thesis objectives and organization. This thesis aims to develop novel numerical methods and assisting tools for human health risk assessment in case of complex aquifer contamination by multispecies chemical systems. The attention is particularly focused on conserving efficiency and accuracy in the numerical solutions in order to be applied in a probabilistic assessment of the human health risk. This assessment seeks to illustrate the capability of the novel method, and more importantly, to develop practical tool and metrics adapted to the risk management of aquifer contamination by reactive chemical mixtures. The thesis is therefore oriented around two main parts respectively focusing on: (1) the development of accurate tools for modeling multispecies reactive systems in heterogeneous conditions and (2) the characterization of the human health risk propagation related to the presence of noxious chemical mixtures released from complex source zones in heterogeneous aquifers. Each part is composed of two chapters. Each chapter takes the form of an article aimed to be published in an international journal.

The first chapter proposes a novel random walk particle tracking method to simulate the transport of chemicals affected by first-order decay network. The novel method is shown to be stable and efficient in three-dimensional and well discretized heterogeneous flow conditions and the peculiar impact of heterogeneity on reactive plumes is furthermore exposed.

In chapter 2, the novel particle based method for multispecies reactive systems is extended to include mass transfer processes. The coupling of the multirate mass transfer model associated to first-order decay network reaction gives the choice between a large variety of scenarios, both in the "architecture" definition of the reaction network and in the conceptualization of the immobile domain. The method is applied with finely defined and heterogeneous hydraulic properties and decay rates to illustrate the potential joint effect of mass transfer and degradation in the immobile domain on a multispecies contamination.

The third chapter, initiating the second part of the thesis, focuses on the stochastic characterization of the human health risk related to a chemical mixtures. After discussing the particular spatial and/or temporal behavior of the statistics and probability functions of selected risk metrics, some main controlling factors of the risk propagation are identified in order to develop specific tools for the risk management of reactive mixtures.

All along the thesis, the particular case of contamination by the chlorinated solvent Perchloroethylene (PCE) is illustratively used. Under specific anaerobic conditions, PCE initiate a sequential reductive dechlorination that has for main consequence the production of a series of noxious sub-compounds before reaching a harmless chemical form. This behavior is a very often encountered example of formation of a chemical mixture. Moreover, PCE, as a well-known dense-nonaqueous phase liquid (DNAPL), is characterized by a particularly problematical release of mass from the contamination source to the groundwater body. To conclude, the fourth chapter proposes an analysis of the impact of DNAPL mass release mode on the propagation of the human health risk in heterogeneous aquifers. In line with the global philosophy, practical observations on the controlling factors of risk propagation are finally delivered.

CHAPTER 2

A Random Walk Solution for Modeling Solute Transport with Network Reactions and Multi-Rate Mass Transfer in Heterogeneous Systems: Impact of Biofilms

Contents

Henri, C. V. and D. Fernàndez-Garcia, submitted in Advances in Water Resources.

2.1 Introduction

The assessment of groundwater polluted systems requires efficient and trustable predictive models. By efficient, we usually mean a small computational cost, and by trustable the proper representation of all key processes controlling the fate and transport of contaminants. Unfortunately, these two desirable properties contrast with the common adage opposing efficiency and complexity in transport simulations. Model complexity often arises from the need to jointly incorporate, in three dimensions, the spatial variability of aquifer properties and numerous chemical reactions into the same multi-species reactive transport model. Thus, properties such as the hydraulic conductivity and the different degradation rates can vary several orders of magnitude in an aquifer [e.g., Rubin, 2003; Fennell et al., 2001; Sandrin et al., 2004]. Even though the description of the spatial variability of all these properties at high resolution is crucial for making contaminant predictions [e.g., Feehley et al., 2000; Salamon et al., 2007; Riva et al., 2008; Llopis-Albert and Capilla, 2009], its implementation in transport models typically leads to numerical problems.

Contaminants in the subsurface are also affected by chemical reactions. Among them, network reactions have been used to model a large variety of contaminants. This includes the degradation of chlorinated solvents [e.g., Clement, 1997, 2001], the decay of radioactive species [e.g., Painter et al., 2008], and the transformation of pesticides, organic phosphates and nitrogen in the environment [e.g., van Genuchten, 1985; Mishra and Mishra, 1991; Vishwanathan et al., 1998]. When contaminant concentrations are small, i.e., less than the Michaelis half-saturation constant in the Monod or Michaelis-Menten enzyme kinetic model, the microbial biotransformation rates can be described by pseudo-first-order reaction rates [e.g., Bouwer et al., 1981; Vogel et al., 1987; Haston and McCarty, 1999; Burnell et al., 2014]. In this context, organic chlorinated solvents are often described by first-order reaction chains schematically described by $A \rightarrow B \rightarrow C \rightarrow D$, meaning that species A is transformed into species B, B into C and so on. The quantification of the risk posed by these contaminants is not a trivial problem [Benekos et al., 2006; Henri and Fernàndez-Garcia, 2014]. The degradation products can constitute new noxious chemical compounds not necessarily less toxic than its parent product. Even though analytical solutions [e.g., Sun et al., 1999; Zhang and Woodbury, 2002; Sun and Buscheck, 2003;

Falta et al., 2002] have been routinely employed by decision makers to efficiently manage the risk posed by these contaminants, the spatial variability of aquifer properties, always observed in natural systems, have seriously questioned the application of such simple approaches [Adrian et al., 1994; Miralles-Wilhelm and Gelhar, 1996; Scholl, 2000; Cunningham and Fadel, 2007; Henri and Fernàndez-Garcia, 2014].

The presence of low permeability regions where contaminants can be temporarily trapped by diffusion typically reduces the efficiency of in situ cleanup technologies [e.g., Soga et al., 2004; Stroo et al., 2012]. To represent this situation in a macroscopic transport model, the porous medium is typically conceptualized as a multi-porosity system that partitions the domain into one region formed by mobile water where advection and dispersion can take place, and another region with relatively immobile water where transport is diffusion limited [van Genuchten and Wierenga, 1976; Neretnieks, 1980; Cunningham et al., 1997; Carrera et al., 1998; Zinn and Harvey, 2003]. This conceptual model has received great attention in the last decades for its success in reproducing tailing and anomalous transport [Harvey and Gorelick, 2000; Huang and Hu, 2000; Li and Brusseau, 2000; Haggerty et al., 2000]. Albeit mass transfer models were originally formulated with a single mass transfer coefficient, i.e., a double porosity system [van Genuchten and Wierenga, 1976; Neretnieks, 1980; Harvey and Gorelick, 2000], this particular model has shown drastic limitations in characterizing the long-term behavior of solute transport [Young and Ball, 1995; Haggerty and Gorelick, 1995; Haggerty et al., 2000]. The main reason is that the diverse mineralogical composition of a real soil and the complex spatial variability of aquifer properties can produce a mixture of mass transfer processes occurring over multiple scales. To overcome this limitation, the multirate mass transfer model was later on developed by Haggerty and Gorelick [1995], who extended the double porosity model to multiple immobile domains. The multirate mass transfer model represents a complete and practical answer to the complexity of a natural groundwater polluted system. For instance, by choosing appropriate parameter values, this model can simulate a large variety of diffusion processes such as diffusion into cylinders, spheres, layers, rock matrices, and others [Haggerty and Gorelick, 1995; Carrera et al., 1998]. Moreover, various authors [e.g. Zinn and Harvey, 2003; G. et al., 2004; Fernàndez-Garcia et al., 2009] have demonstrated, that solute transport can be properly upscaled using a multirate mass transfer model.

The incorporation of all theses processes highly complicates numerical simulations. Reactive transport codes based on Eulerian methods (finite differences or finite-elements) typically encounter numerical problems and suffer from computational burden when dealing with strong heterogeneities [Salamon et al., 2006a; Boso et al., 2013]. These limitations have been largely emphasized by the recent need to conduct integrated risk analysis studies with many uncertain parameters at high resolution [Maxwell et al., 2008; de Barros et al., 2009; Benekos et al., 2006]. In this context, Particle Tracking Methods (PTMs) constitute an efficient numerical alternative to simulate reactive transport [Kitanidis, 1994; Salamon et al., 2006a; Henri and Fernàndez-Garcia, 2014]. Even though a large variety of methods exist to simulate rate-limited mass transfer processes with particle tracking [Benson and Meerschaert, 2009; De Simoni et al., 2001; M. and Berkowitz, 2003; Salamon et al., 2006b; Tsang and Tsang, 2001a], this method is still limited in the type of chemical reactions available, which include sorption [Tompson, 1993; Valocchi and Quinodoz, 1989; Michalak and Kitanidis, 2000], radioactive decay [Wen and Gómez-Hernández, 1996; Painter et al., 2008], first-order network reactions [Burnell et al., 2014; Henri and Fernàndez-Garcia, 2014], and simple bimolecular reactions [Benson and Meerschaert, 2008a; Ding et al., 2013; Edery et al., 2009, 2010; Paster et al., 2014] among others. None of the methods available nowadays supports multi-porosity systems with network reactions in three-dimensional randomly heterogeneous porous media.

We present a new particle tracking method that efficiently handles hydro-biogeochemical spatial variability, multi-rate mass transfer processes and first-order network reactions. The approach is based on the development of transition probabilities that describe the likelihood that particles belonging to a given species and mobile/immobile domain at a given time will be transformed into another species and mobile/immobile domain afterwards. These probabilities are derived from the solution matrix of the spatial moments governing equations. The organization of the paper is as follows. First, sections 2.2 and 2.3 respectively present the governing transport equations and the development of transition probabilities. These probabilities are then used in section 2.4 to incorporate mass transfer processes and network reactions into a random walk model. Finally, a 3D high-resolution synthetic example is presented to investigate the impact that the different sources of variability have on the fate and transport of tetrachloroethylene (PCE) and its degradation products in a groundwater polluted system.

2.2 The Multirate Model with Network Reactions

2.2.1 Conceptual Model

The multirate mass transfer model has been extensively presented in the literature [Haggerty and Gorelick, 1995; Haggerty et al., 2000; Donado et al., 2009]. Here, we extend the model for use in modeling contaminant transport with network reaction systems. The porous medium is conceptualized as a multi-porosity system consisting of one mobile water region where solute moves by advection and dispersion, and any number of immobile water regions where solute transport is diffusion limited. A series of mass transfer equations describe the mass exchange between the mobile and any number of immobile regions. Considering this conceptualization of the porous medium, Figure 2.1 shows a schematic representation of a chain reaction ($A \rightarrow B \rightarrow C$) in this system. This figure represents several physical and biochemical processes that occur simultaneously in porous media. At the large scale, contaminants can diffuse into clay layers/lenses or get transferred into low conductivity regions by slow advection. In this context, it is generally observed that biotransformation rates in the mobile and immobile regions can be substantially different. The main reason is that biotransformation rates and bacterial activity largely depends on the clay content, being often smaller in confining beds than in more permeable systems [Chapelle, 2001]. Because bacteria generally have diameters that range between 0.1 and 1 microns, the small effective porosity of clays typically restricts the ability of bacteria to move and reproduce effectively. Also, the natural occurrence of preferential flow channels in porous media (typically represented as a mobile region in the multirate model) favors the movement of groundwater and dissolved elements through certain pathways, which typically harbor larger bacterial densities and microbial activities compare to the adjacent porous media [Pivetz and Steenhuis, 1995; Mallawatantri et al., 1996; Rubol et al., 2014]. In fact, Vinther et al. [1999] and Bundt et al. [2001] found that both substrate availability and nutrient supply are largest in preferential flow paths, enhancing bacterial biomass and associated microbial processes. Similar processes occur at a smaller scale where contaminants may diffuse into stagnant water (intraaggregate or dead-end pores) or/and inside biofilms attached to the aquifer soil surface. In this case, the rate of contaminant degradation mainly occurs in the active biofilm rather than in the bulk aqueous phase [Rittmann and McCarty, 1980; Baveye and Valocchi, 1989; Cunningham

and Mendoza-Sanchez, 2006]. Based on these observations, the reactive multirate model proposed here considers that network reactions can simultaneously occur over multiple scales with different biotransformation rates in the mobile and immobile regions.

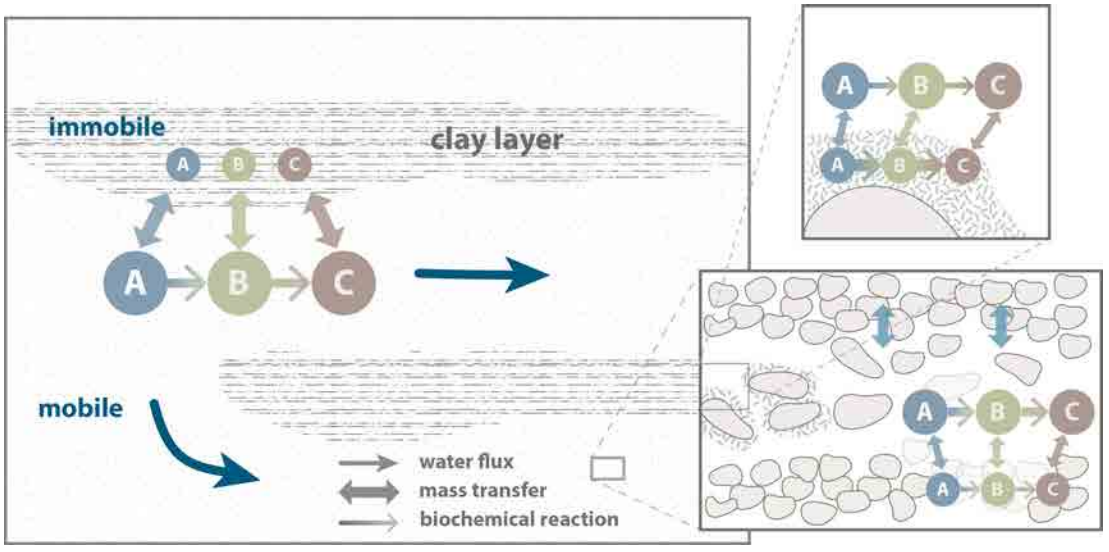

FIGURE 2.1: Illustration of mass transfer occurring at different scales and rates in case of a sequential three-species reactive system (A → B → C). The thickness of the bicolor arrow representing biochemical reaction is proportional to the expected intensity of the reaction. The bottom right magnifying frame illustrates the heterogeneity in the grain distribution and related contaminant diffusion from/into aggregates. The top right magnifying frame illustrates the potential diffusion-rate limited transfer of contaminant toward an active biofilm and the subsequent enhanced degradation.

2.2.2 Governing Equations

We consider a network reaction system formed by N_s species moving through a mobile domain of porosity ϕ_0 and N_{im} immobile domains of porosity $(\phi_1, ..., \phi_{N_{im}})$. Let us denote the biotransformation rate associated with species i and j in the ℓ domain by

$$r_{ij\ell} = y_{ij} k_{j\ell} \phi_\ell c_{j\ell}, \tag{2.1}$$

where $r_{ij\ell}$ is the production of mass of the ith species per unit of time and aquifer volume $\left[ML^{-3}T^{-1}\right]$ due to the degradation of the jth species in the ℓ domain, $k_{i\ell}$ $\left[T^{-1}\right]$ is the

first-order contaminant destruction rate constant of the ith species in the ℓ domain, y_{ij} $\left[M\,M^{-1}\right]$ is the effective yield coefficient for any reactant or product pair (i,j). This coefficient is a stoichiometric coefficient defined as the ratio of mass of species i generated to the amount of mass of species j consumed. The yield coefficients y_{ii} is equal to -1 and represent the first-order decay of the ith species. Similar reaction terms have been presented by many authors [Clement, 1997, 2001; Sun et al., 1999; Falta et al., 2002].

The multirate mass transfer model with network reactions can be written as the following system of equations

$$\phi_0 R_{i0}\frac{\partial c_{i0}}{\partial t}+\sum_{l=1}^{N_{im}}\phi_\ell R_{i\ell}\frac{\partial c_{i\ell}}{\partial t}=\mathscr{L}(c_{i0})+\sum_{j=1}^{N_s}\sum_{\ell=0}^{N_{im}} r_{ij\ell},\qquad i=1,N_s, \tag{2.2}$$

$$\phi_\ell R_{i\ell}\frac{\partial c_{i\ell}}{\partial t}=\phi_\ell\alpha'_{i\ell}\left(c_{i0}-c_{i\ell}\right)+\sum_{j=1}^{N_s} r_{ij\ell},\qquad \ell=1,N_{im},\qquad i=1,N_s. \tag{2.3}$$

Without the chemical reaction term $r_{ij\ell}$, these equations form the standard multirate mass transfer model [Haggerty and Gorelick, 1995] that describes advective-dispersive transport with rate-limited mass transfer between a mobile domain and any number of immobile domains for each species. In these equations, the variable c_{i0} $\left[M\,L^{-3}\right]$ is the concentration of the ith species in the mobile domain (denoted always by the subscript index $\ell=0$), $c_{i\ell}$ $\left[M\,L^{-3}\right]$ is the concentration of the ith species in the ℓth immobile domain ($\ell=1,...,N_{im}$), R_{i0} (*dimensionless*) is the retardation factor of the ith species in the mobile domain, and $R_{i\ell}$ (*dimensionless*) is the retardation factor of the ith species in the ℓth immobile domain ($\ell=1,...,N_{im}$). Sorption is considered in local equilibrium (linear isotherm), and $\mathscr{L}(c)$ is the transport operator of the mobile concentrations defined by

$$\mathscr{L}(c)=\nabla\cdot(\phi_0\mathbf{D}\nabla c)-\nabla\cdot(\mathbf{q}c)\,, \tag{2.4}$$

where $\mathbf{q}$ $\left[L\,T^{-1}\right]$ is the groundwater flux, and $\mathbf{D}$ is the dispersion tensor $\left[L^2\,T^{-1}\right]$. The first equation (2.2) is actually the mass balance associated with any of the species involved in the network reaction system, and equation (2.3) describes the mass transfer of the ith

species between the mobile domain and the ℓth immobile domain. We have assumed that only aqueous concentrations are susceptible to undergo chemical reactions, i.e., no biodegradation in the sorbed phase occurs. Nevertheless, we note that other situations can be simulated by properly redefining the degradation rates [van Genuchten, 1985].

2.3 Development of Transition Probabilities

Transition probabilities denote the probability that a system that was in a given state at time $t = 0$ jumps to another state at some later time $t > 0$ [e.g., Ross, 2003]. In subsurface hydrology, this concept has been used in the past to simulate solute transport with sorption/desorption processes [Valocchi and Quinodoz, 1989; Michalak and Kitanidis, 2000], rate-limited mass transfer processes [Salamon et al., 2006b], and kinetic network reactions [Henri and Fernàndez-Garcia, 2014]. Following Michalak and Kitanidis [2000] and Henri and Fernàndez-Garcia [2014], transition probabilities can be determined from the evolution of the zeroth spatial moments of the solute plume. This is the procedure employed here.

Let us express the governing system of equations (2.2)-(2.3) in terms of the total densities, $\rho_{i\ell}$, defined as the total amount of aqueous and sorbed mass of a given species i per unit volume in the ℓ domain, i.e., $\rho_{i\ell} = \phi_\ell R_{i\ell} c_{i\ell}$. From this, the transport equation reads as

$$\sum_{\ell=0}^{N_{im}} \frac{\partial \rho_{i\ell}}{\partial t} = \mathscr{L}\left(\frac{\rho_{i0}}{\phi_0 R_{i0}}\right) + \sum_{j=1}^{N_s}\sum_{\ell=0}^{N_{im}} K_{ij\ell}\rho_{j\ell}, \qquad i = 1, N_s, \tag{2.5}$$

$$\frac{\partial \rho_{i\ell}}{\partial t} = \alpha_{i\ell}\beta_{i\ell}\rho_{i0} - \alpha_{i\ell}\rho_{i\ell} + \sum_{j=1}^{N_s} K_{ij\ell}\rho_{j\ell}, \qquad \ell = 1, N_{im}, \qquad i = 1, N_s, \tag{2.6}$$

where $K_{ij\ell} = y_{ij}k_{j\ell}/R_{j\ell}$, $\beta_{i\ell}$ is the field capacity coefficient of the ith species in the ℓ immobile domain, and $\alpha_{i\ell}$ is the apparent mass transfer coefficient of the ith species in the ℓ immobile domain,

$$\beta_{i\ell} = \frac{\phi_\ell R_{i\ell}}{\phi_0 R_{i0}}, \tag{2.7}$$

$$\alpha_{i\ell} = \frac{\alpha'_{i\ell}}{R_{i\ell}}. \tag{2.8}$$

Let us also define the zeroth spatial moment of the solute plumes associated to species i in the mobile or any immobile domain ℓ by,

$$\mu_{i\ell}(t) = \int_V \rho_{i\ell}(\mathbf{x}, t) dV, \qquad \ell = 0, N_{im}, \qquad i = 1, N_s, \tag{2.9}$$

where V is the volume of the domain. Knowing that a particle located at position $\mathbf{x}_t$ at time t can be seen as an infinitely small plume [Kitanidis, 1994], the total density of the particle in either the mobile or immobile domain can be represented by

$$\rho_{i\ell}(\mathbf{x}, t) = \mu_{i\ell}(t)\delta(\mathbf{x} - \mathbf{x}_t), \qquad \ell = 0, N_{im}, \qquad i = 1, N_s, \tag{2.10}$$

The governing equations of the spatial moments can be derived by integrating by parts the transport equations given by (2.2)-(2.3). This leads to

$$\sum_{\ell=0}^{N_{im}} \frac{d\mu_{i\ell}(t)}{dt} = \sum_{j=1}^{N_s} \sum_{\ell=0}^{N_{im}} K_{ij\ell}(\mathbf{x}_t)\mu_{j\ell}(t), \qquad \forall\ i = 1, N_s, \tag{2.11}$$

$$\frac{d\mu_{i\ell}}{dt} = \alpha_{i\ell}\beta_{i\ell}\mu_{i0} - \alpha_{i\ell}\mu_{i\ell} + \sum_{j=1}^{N_s} K_{ij\ell}\mu_{j\ell}, \qquad \ell = 1, N_{im}, \qquad i = 1, N_s. \tag{2.12}$$

Let us now define the vector $\mathbf{m}_t$ of size $n = N_s(1 + N_{im})$ as

$$\mathbf{m}_t = \begin{bmatrix} \mathbf{m}_1(t) \\ \vdots \\ \mathbf{m}_{N_s}(t) \end{bmatrix}, \quad \text{where} \quad \mathbf{m}_i(t) = \begin{bmatrix} \mu_{i0}(t) \\ \mu_{i1}(t) \\ \vdots \\ \mu_{iN_{im}}(t) \end{bmatrix}. \tag{2.13}$$

The system of equations (2.11)-(2.12) can then be expressed in matrix format as

$$\mathbf{A}\frac{d\mathbf{m}_t}{dt} = \mathbf{B}(\mathbf{x}_t)\mathbf{m}_t. \tag{2.14}$$

Note that the subscript $\mathbf{x}_t$ expresses that the matrix is evaluated at the particle position $\mathbf{x}_t$. The $\mathbf{A}$ matrix is an $n \times n$ block diagonal matrix defined as

$$\mathbf{A} = \begin{bmatrix} \mathbf{A}'_{11} & \mathbf{0} & \cdots & \mathbf{0} \\ \mathbf{0} & \mathbf{A}'_{22} & \ddots & \vdots \\ \vdots & \ddots & \ddots & \mathbf{0} \\ \mathbf{0} & \cdots & \mathbf{0} & \mathbf{A}'_{N_s N_s} \end{bmatrix}, \tag{2.15}$$

where $\mathbf{0}$ is the zero matrix of size $(1 + N_{im}) \times (1 + N_{im})$, and $\mathbf{A}'_{ii}$ $\{i = 1, ..., N_s\}$, is the following $(1 + N_{im}) \times (1 + N_{im})$ constant matrix

$$\mathbf{A}'_{ii} = \begin{bmatrix} 1 & 1 & \cdots & 1 \\ 0 & 1 & 0 & 0 \\ \vdots & \ddots & \ddots & 0 \\ 0 & \cdots & 0 & 1 \end{bmatrix}. \tag{2.16}$$

The $\mathbf{B}(\mathbf{x}_t)$ matrix is the following $n \times n$ block matrix evaluated at the $\mathbf{x}_t$ location,

$$\mathbf{B}(\mathbf{x}_t) = \begin{bmatrix} \mathbf{B}'_{1\,1} & \cdots & \mathbf{B}'_{1\,N_s} \\ \vdots & \ddots & \vdots \\ \mathbf{B}'_{N_s\,1} & \cdots & \mathbf{B}'_{N_s\,N_s} \end{bmatrix}_{\mathbf{x}_t}, \tag{2.17}$$

where $\mathbf{B'}_{ij}(\mathbf{x}_t)$ are matrices of size $(1 + N_{im}) \times (1 + N_{im})$ whose diagonal blocks $\mathbf{B'}_{ii}$ $(i = j)$ are defined by

$$\mathbf{B}'_{ii}(\mathbf{x}_t) = \begin{bmatrix} K_{ii0} & K_{ii1} & \cdots & K_{iiN_{im}} \\ \alpha_{i1}\beta_{i1} & -\alpha_{i1} + K_{iik} & \ddots & 0 \\ \vdots & 0 & \ddots & 0 \\ \alpha_{iN_{im}}\beta_{iN_{im}} & \cdots & 0 & -\alpha_{iN_{im}} + K_{iiN_{im}} \end{bmatrix}_{\mathbf{x}_t}, \tag{2.18}$$

and whose non-diagonal blocks $\mathbf{B'}_{ij}$ $(i \neq j)$ are written as

$$\mathbf{B'}_{ij}(\mathbf{x}_t) = \begin{bmatrix} K_{ij0} & K_{ij1} & \cdots & K_{ijN_{im}} \\ 0 & K_{ij1} & \ddots & \vdots \\ \vdots & \ddots & \ddots & 0 \\ 0 & \cdots & 0 & K_{ijN_{im}} \end{bmatrix}_{\mathbf{x}_t} . \tag{2.19}$$

The solution of the linear system of differential equations (2.14) form an n-dimensional complex linear vector space. That is to say that n linearly independent solutions of (2.14) exist so that

$$\mathbf{m}_t = \sum_{j=1}^{n} c_j \mathbf{m}_t^{(j)}, \tag{2.20}$$

where c_j are time-independent coefficients and $\mathbf{m}_t^{(j)}$ is the jth solution vector of the system. It is often convenient to lump the independent solution vectors together in a so-called *solution matrix*, denoted here as $\mathbf{P}_t$ in view of its future use as the state transition probability matrix

$$\mathbf{P}_t = \left(\mathbf{m}_t^{(1)}, \ldots , \mathbf{m}_t^{(n)} \right). \tag{2.21}$$

From (2.14), this solution matrix also obeys the differential equation

$$\frac{d\mathbf{P}_t}{dt} = \mathbf{A}^{-1}\mathbf{B}(\mathbf{x}_t)\mathbf{P}_t \tag{2.22}$$

The *Picard-Lindel*öf theorem establishes that a unique solution matrix exist for a given initial condition. From Henri and Fernàndez-Garcia [2014], the solution matrix that satisfies the initial condition $\mathbf{P}_t(t = 0) = \mathbf{Id}$ can be assimilated to a state transition probability matrix. This is easily seen by noticing that the system of equations (2.22) can be interpreted as the *forward kolmogorov equations* of a continuous-time markov chain in which the state space is formed by the N_s species involved in the reaction network and the $1 + N_{im}$ mobile and immobile domains.

This can also be explained by physical principles. Consider, for instance, a reactive system that evolves from an initial condition given by $m_t(t=0) = (\ 1 \quad 0 \quad ... \quad 0\ )^t$, i.e., only the first species in the mobile domain exists, initially. When all particles have the same mass, the probability $P_{i1}(t)$ that a particle initially being species 1 in the mobile domain is transformed and move into another species and domain at a later time t can be estimated by the mass fraction of the species involved, given by $m_t(t)$. Repeating this for any given initial species in the mobile or immobile domain leads to the transition probability matrix $\mathbf{P}_t$.

For chemically heterogeneous systems, the solution of (2.22) is given by the *Peano-Baker* series

$$\mathbf{P}_t = \mathbf{Id} + \int_0^t \mathbf{A}^{-1}\mathbf{B}(\mathbf{x}_{\tau_1})\, d\tau_1 + \int_0^t \mathbf{A}^{-1}\mathbf{B}(\mathbf{x}_{\tau_1})\, d\tau_1 \int_0^{\tau_1} \mathbf{A}^{-1}\mathbf{B}\, d\tau_1 d\tau_2 + \dots \tag{2.23}$$

Nevertheless, for small times (as typically used in particle tracking simulations) or locally homogeneous media, equation (2.23) can be approximate by

$$\mathbf{P}_t = \exp\left(\mathbf{A}^{-1}\mathbf{B}(\mathbf{x}_t)t\right). \tag{2.24}$$

The challenge here is then to compute the exponential of the matrix $\mathbf{A}^{-1}\mathbf{B}$. A large diversity of methods exist to solve such a matrix [Moler and van Loan, 2003]. Not all methods are equivalent in terms of applicability, precision and efficiency. In this work, we found that *diagonalization methods* are convenient and computationally efficient compared to other approaches, such as the PADE approximation.

Suppose that the eigenvalues of $\mathbf{A}^{-1}\mathbf{B}$ are real and distinct. Then, there is a non-singular $n \times n$ matrix $\mathbf{S}$ and a diagonal $n \times n$ matrix $\mathbf{D}$ such that $\mathbf{A}^{-1}\mathbf{B} = \mathbf{SDS}^{-1}$. The matrix $\mathbf{S}$ has as its columns the n eigenvectors for the n eigenvalues of $\mathbf{A}^{-1}\mathbf{B}$. From this, the exponential of such matrix can be written for small times as

$$\mathbf{P}_t = \mathbf{S}(\mathbf{x}_t)\exp(\mathbf{D}(\mathbf{x}_t)t)\mathbf{S}^{-1}(\mathbf{x}_t) \tag{2.25}$$

The advantages of the diagonalization method in particle tracking are numerous: (1) The exponential of a diagonal matrix is the exponential of each component, which is cheaply computed; (2) In heterogeneous systems with spatially varying chemical coefficients the eigensystem has to be determined only once per cell or per parameter zone; (3) The method permits to efficiently use a constant displacement scheme [Wen and Gómez-Hernández, 1996], which adjusts automatically the time step size according to the grid courant number in order to decrease computational effort; (4) Eigensystems of general matrices can be computed efficiently and with accuracy by subroutine libraries such as LAPACK [Anderson et al., 1999].

2.4 Implementation into the Random Walk Method

2.4.1 The Algorithm

The random walk particle tracking method is based on the apportionment of the transported total mass into a large number of representative particles that move randomly in space. Thus, a particle moves by simple relationships and is characterized by an evolving state which in our case is defined by two variables: the particle species i and the domain ℓ through which the particle is moving. The change of the particle state is given by the state transition probability matrix $\mathbf{P}_t$, which can be conveniently written as the following block matrix

$$\mathbf{P}_t = \begin{bmatrix} \mathbf{P}_{1\,1} & \cdots & \mathbf{P}_{1\,N_s} \\ \vdots & \ddots & \vdots \\ \mathbf{P}_{N_s\,1} & \cdots & \mathbf{P}_{N_s\,N_s} \end{bmatrix}, \tag{2.26}$$

where $\mathbf{P}_{ij}$ are the matrices

$$\mathbf{P}_{ij} = \begin{bmatrix} P_{ij,00} & P_{ij,01} & \cdots & P_{ij,0N_{im}} \\ P_{ij,10} & P_{ij,11} & \cdots & \vdots \\ \vdots & \vdots & \ddots & \vdots \\ P_{ij,1N_{im}} & \cdots & \cdots & P_{ij,N_{im}N_{im}} \end{bmatrix}. \tag{2.27}$$

The element $P_{ij,k\ell}(t)$ of the matrix $\mathbf{P}_t$ is the probability that a particle being initially at species j and domain ℓ will turn into species i and domain k in a later time t. Let us define m as an index number denoting all the potential states (i,k) in which a particle initially belonging to species j and domain ℓ can turn into after a time dt,

$$m(i,k) = N_s(i-1) + k. \tag{2.28}$$

Knowing m, the corresponding particle species i and domain k can be estimated as

$$i(m) = \mathcal{F}\left(\frac{m}{1+N_{im}}\right) + 1, \tag{2.29}$$

$$k(m) = m - N_s\left(i(m) - 1\right), \tag{2.30}$$

where $\mathcal{F}(x)$ is the floor function that determines the largest integer not greater than the real number x. According to the state transition probability matrix evaluated at the particle position $\mathbf{x}_t$, the new particle state is defined by the index number η that satisfies the following equation

$$\sum_{m=1}^{\eta-1} P_{i(m)j,k(m)\ell}(dt) \; < r \; \leq \sum_{m=1}^{\eta} P_{i(m)j,k(m)\ell}(dt). \tag{2.31}$$

where r is a random number generated from an uniform distribution in a unit interval. The new species i and domain k will be given by $i(\eta)$ and $k(\eta)$, respectively. Once the new state of the particle is known, those particles associated to the mobile domain ($k=0$) will be allowed to move by advection and dispersion following the random-walk scheme developed by Henri and Fernàndez-Garcia [2014] for network reactions

$$\mathbf{x}_{t+dt} = \mathbf{x}_t + \mathbf{A}_{ij}(\mathbf{x}_t, t)\, dt + \mathbf{B}_{ij}^{1/2}(\mathbf{x}_t, dt) \cdot \boldsymbol{\xi}(t)\, \sqrt{dt} \tag{2.32}$$

where

$$\mathbf{A}_{ij}(t) = \frac{\mathbf{q}_p}{\phi\, \mathcal{R}^e_{ij}}, \tag{2.33}$$

$$\mathbf{B}_{ij} \cdot \mathbf{B}_{ij}{}^t = \frac{2\,\mathbf{D}}{\mathcal{R}^e_{ij}}, \tag{2.34}$$

where the vector $\mathbf{A}_{ij}$ and $\mathbf{B}_{ij}$ are the drift and the dispersion displacement associated to a particle that initially belongs to species j and is transformed into species i during an elapsed time dt, and $\boldsymbol{\xi}$ is a vector of independent and normally distributed random variables characterized by a zero mean and a unit variance. The dispersion matrix used here has the form given by Lichtner et al. [2002]. The parameter R^e_{ij} is the effective retardation factor that evolves as a result of the differential retardation effects among the species involved in the chemical network reaction system [Henri and Fernàndez-Garcia, 2014]. These authors showed that, for small time steps, the harmonic mean of the retardation values of the species involved in the chemical reaction is a good estimate of the effective retardation factor. Given that random walk simulations typically use reasonably small time step, this was the method chosen in this work. This algorithm was implemented into the RW3D particle tracking code [Fernàndez-Garcia et al., 2005a; Salamon et al., 2006b; Henri and Fernàndez-Garcia, 2014].

2.4.2 Numerical Details

The choice of the time step dt is an important issue in particle tracking methods. This parameter largely controls the efficiency and performance of the simulation. In advective-dominated transport problems, it is convenient to estimate dt so as to satisfy that the grid courant number C_g is a small value

$$C_g = \frac{v dt}{ds} < 0.1 \tag{2.35}$$

where v is the particle velocity, dt is the time step, and ds is the size of the grid cell. This maintains accuracy and efficiency in heterogeneous porous media where, otherwise, areas with small velocities will slow down the simulation [Wen and Gómez-Hernández,

1996]. On the other hand, Salamon et al. [2006b] showed that if the time step size is not sufficiently small to properly characterize mass transfer the detention of particles in immobile domains will artificially increase producing artificial dispersion and tailing. To avoid this problem, the grid mass transfer Damköhler number D_gI should also fulfill the following criteria

$$D_gI = \alpha_{i\ell}(\beta_{i\ell} + 1)R_{i0}dt < 10 \tag{2.36}$$

Moreover, Henri and Fernàndez-Garcia [2014] demonstrated that if the time step size is not small enough to properly characterize first-order network reactions particles will artificially increase chemical reactions. To overcome this problem, the time step should also satisfy that the grid chemical Damköhler number D_gII is smaller than 0.1, i.e.,

$$D_gII = \frac{k_i}{R_{i\ell}}dt < 0.5 \tag{2.37}$$

The latter criteria can be substantially relaxed if higher-order moments are used to modify the drift and the dispersion displacement of the particle movement [Henri and Fernàndez-Garcia, 2014]. In the limit, when the number of particles tends to infinity, the particle density that evolves from the repeated application of (2.31) and (2.32) satisfies the system of reactive transport equations (2.2)-(2.3). However, since a discrete number of particles is always used, the particle tracking simulation will suffer from problems originating from sub-sampling, i.e., statistical fluctuations produced by the reconstruction of concentrations from discrete information. Smoothing techniques must then be used to improve the performance of the method [Fernàndez-Garcia and Sanchez-Vila, 2011]. Once the total density fields $\rho_{i\ell}(\mathbf{x}, t)$ are estimated, concentrations can be calculated as $c_{i\ell}(\mathbf{x}, t) = \rho_{i\ell}(\mathbf{x}, t)/(\phi_\ell(\mathbf{x})R_{i\ell}(\mathbf{x}))$.

2.5 Temporal Evolution of the Transition Probabilities

This section analyzes the relative influence of biochemical reactions and mass transfer on the functional form of the transition probabilities. We will show that the distribution of

mass among species and domains strongly depends on the interplay between these two processes. To simplified the problem, we consider a double porosity media with a simple chemical reaction, i.e., species 1 is transformed into species 2. The analysis assumes that the mass transfer coefficient (α), the retardation factor in the mobile domain (R_m) and the retardation factor in the immobile domain (R_{im}) are the same for all species. Based on this, the system of equations (2.12)-(2.11) can be written in dimensionless form (see Appendix C) using the following variables,

$$\tau = \frac{k_m}{R_m} t, \tag{2.38}$$

$$\chi = \frac{R_m k_{im}}{R_{im} k_m}, \tag{2.39}$$

$$Da_{II} = \frac{k_m}{\alpha R_m}, \tag{2.40}$$

The variable Da_{II} can be seen as the second Damkhöler number defined as the ratio of the chemical reaction rate to the mass transfer rate. The variable χ is the ratio between the immobile and the mobile decay rate. As shown in Appendix C, in this case, the transition probability matrix $\mathbf{P}_t$ can be explicitly determined. From this, we evaluate the influence of Da_{II} and χ on the temporal evolution of $\mathbf{P}_t$ associated with a particle initially belonging to species 1 and the mobile domain. The effect that the field capacity β has on the transition probabilities is similar to the effect induced by the Damkhöler number and is therefore not shown.

Figure 2.2 shows the influence of mass transfer on the temporal evolution of $\mathbf{P}_t$ for $\chi = 1$ and $\beta = 10$. When the mass transfer rate is larger than the decay rate in the mobile domain (i.e., $Da_{II} < 1$), the probability to remain in the mobile domain (Figure 2.2a) drops to an early equilibrium between the mobile and the immobile domain. After this, biochemical reactions start dominating and this probability decays with time to almost zero. In accordance with this result, the probability that species 1 is in the immobile domain after time t increases to a plateau until chemical reactions take place at $\tau \approx 1$ (Figure 2.2b). Consequently, the probability that this particle is in the immobile domain

increases with the mass transfer rate (inverse of Da_{II}). Interestingly, at early times, mass transfer is still not active and the probability that species 1 turns into 2 in the mobile domain does not depend on Da_{II} (Figure 2.2c). This probability increases linearly with time due to the degradation of species 1 in the mobile domain. When $Da_{II} < 1$ and mass transfer starts to take place there are less particles of species 1 to degrade in the mobile domain and the probability stabilizes. With time, this effect vanishes and the probability increases again linearly with time until species 2 starts to degrade.

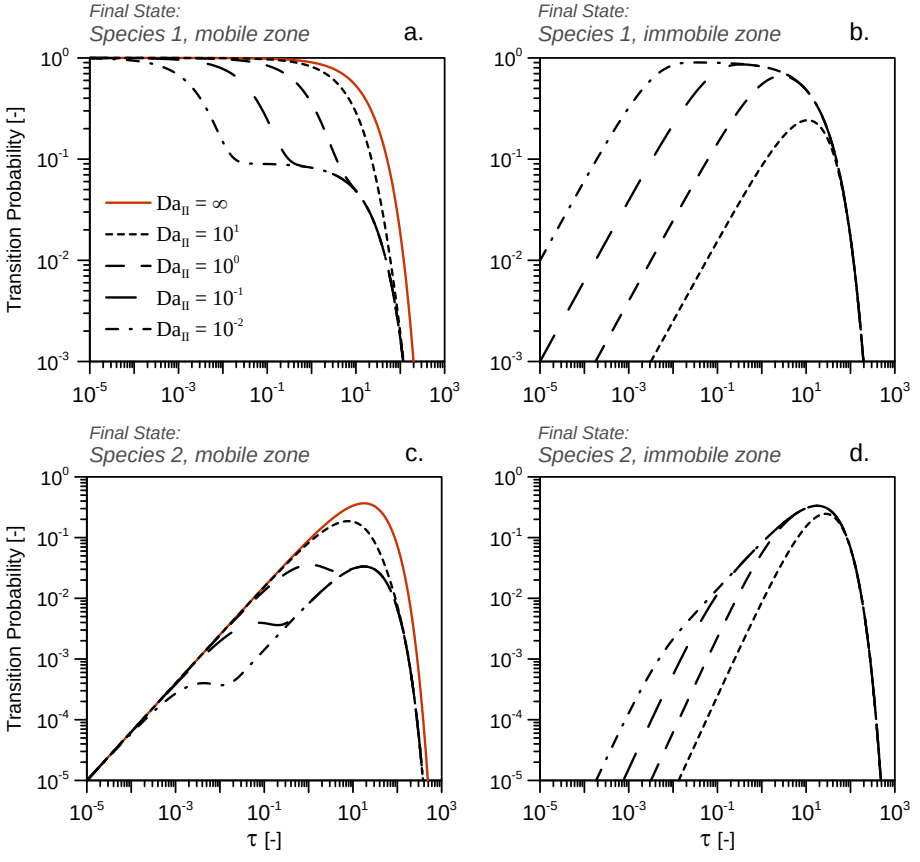

FIGURE 2.2: Impact of the second Damköhler number on the transition probability of a particle initially being species 1 in the mobile domain: (a) probability to stay in the initial state after a time t; (b) probability to be transferred to species 1 in the immobile domain; (c) probability to turn into species 2 in the mobile domain; and (d) probability to turn into species 2 in the immobile domain.

A decay difference between the mobile and immobile domain ($\chi \neq 1$) can also have relevant consequences on the temporal evolution of $\mathbf{P}_t$. This is shown in Figure 2.3 for $Da_{II} = 1$

and $\beta = 10$ (rate-limited mass transfer). The probability that the particle still belongs to species 1 in the mobile domain after a time t is shown in Figure 2.3a. Results show that when degradation in the immobile domain is smaller than that of the mobile domain ($\chi < 1$), for example due to the presence of an aquitard, the early equilibrium between the mobile and the immobile domain discussed previously is also observed. However, when degradation is higher in the immobile domain ($\chi > 1$), for example due to the presence of biofilms at the pore-scale, the mass transferred into the immobile domain will be rapidly consumed (see Figure 2.3b), preventing the previously observed mass transfer equilibrium (Figure 2.3a).

During pump-and-treat remediation strategies, it is often observed that once pumping ceases, a rebound of concentrations at the well takes place [e.g., de Barros et al., 2013]. Figure 2.3c shows that in a double-porosity system with network reactions this effect can also occur without any change in the pumping regime. We call this effect "natural rebound" which is explained as it follows. When degradation is active in the immobile domain, the parent species transferred into the immobile domain will be transformed into degradation products. Once the reaction chain in the mobile domain has occurred, these products will be allowed to back diffuse into the mobile domain causing the rebound of concentrations. This explains the double peak observed in Figure 2.3c for the degradation product. When degradation is not active in the immobile domain, a double peak is also observed at a later time ($\chi = 0$). In this case, once the chain reaction in the mobile domain has occurred, a second chain reaction in the mobile domain can be triggered by the release of the parent species previously stored in the immobile domain due to back-diffusion.

2.6 An Example of Application: Effect of the parameters spatial variability

2.6.1 Problem Setup

The main advantage of our method is the possibility to simultaneously represent mass transfer, spatially varying properties (heterogeneity) and network reactions without numerical problems. To illustrate this, we consider a three-dimensional high-resolution

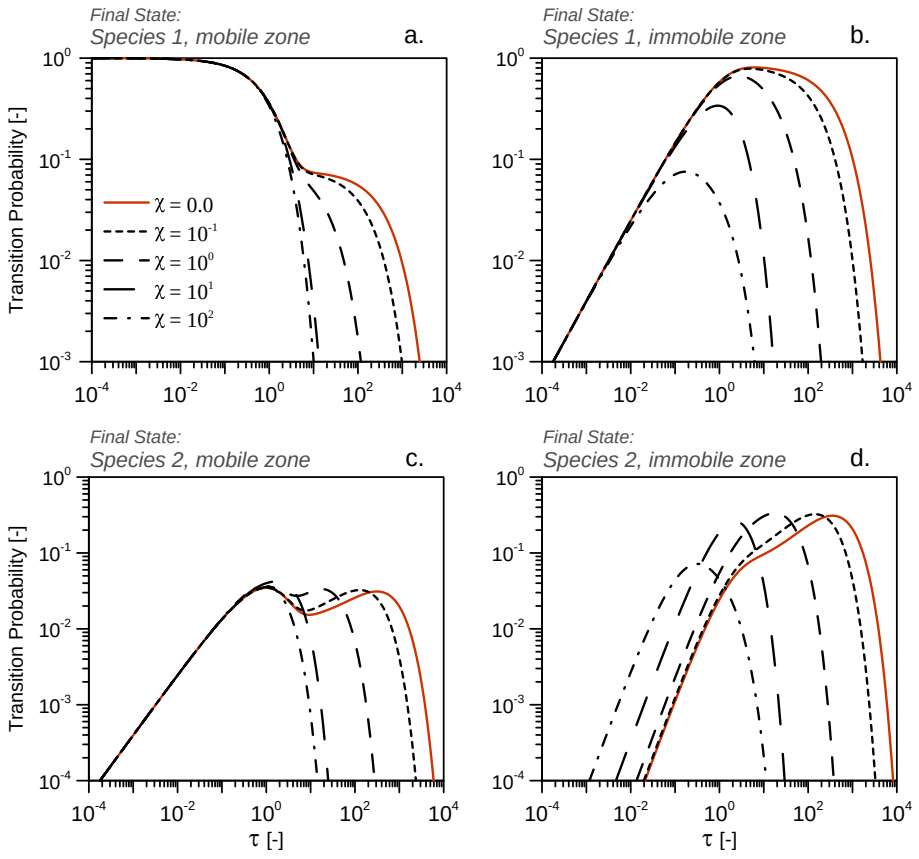

FIGURE 2.3: Impact of the ratio between decay rate in the mobile and immobile domain on the transition probability of a particle initially being species 1 in the mobile domain: (a) probability to stay in the initial state after a time t; (b) probability to be transferred to species 1 in the immobile domain; (c) probability to turn into species 2 in the mobile domain; and (d) probability to turn into species 2 in the immobile domain.

synthetic aquifer initially contaminated by tetrachloroethylene (PCE) and affected by rate-limited mass transfer and degradation. With time, PCE is sequentially transformed into TCE (trichloroethylene), TCE into DCE (*cis*-Dichloroethylene), and DCE into VC (vinyl chloride). Groundwater flow takes place in a heterogeneous hydraulic conductivity field obtained from a single realization of a sequential Gaussian simulation. The natural logarithm of the hydraulic conductivity ($\ln K$) is described by a random function of mean 3.55 m/d and an isotropic variogram of range 10.0 m and variance of 2.5. The domain is a rectangular block of $120\times100\times40$ m^3, descritized into $300\times250\times100$ cubic grid cells of size 0.4 m (Figure 2.4). The flow is driven by a hydraulic gradient of 0.01 oriented

along the x-axis and solved using the finite difference code Modflow [Harbaugh et al., 2000]. The transport parameters adopted are summarized in Table 2.1. Porosity, local dispersivities and retardation factors are always considered homogeneous. The source of contamination is represented by a PCE instantaneous point injection in the mobile domain (x=20,y=50,z=20) of unit mass equally partitioned into 100,000 particles. Concentration breakthrough curves of all species (BTCs) were recorded at two control planes located at 1 and 5 variogram ranges from the injection location (see Figure 2.4).

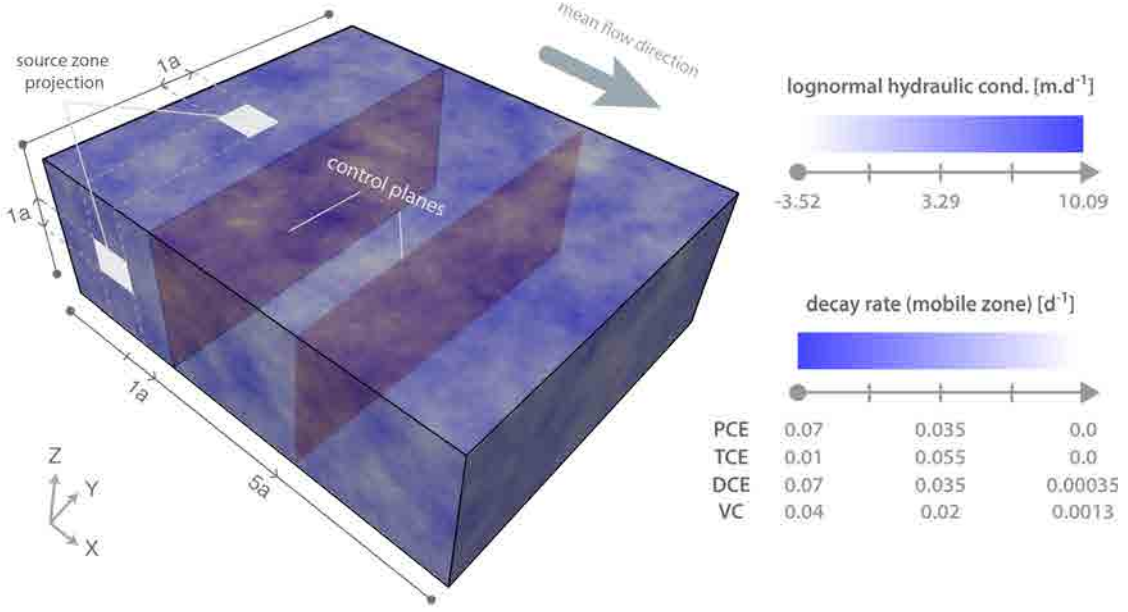

FIGURE 2.4: Simulation setup displaying the lognormal distribution of the hydraulic conductivity and first-order degradation rates of PCE, TCE, DCE and VC.

Rate-limited mass transfer is simulated using the spherical diffusion model presented by Rao et al. [1980]. Haggerty and Gorelick [1995] showed that this model and the multi-rate model are mathematically equivalent provided that the series of porosities and mass transfer coefficients are specifically chosen. For practical purposes, the series has to be truncated to a discrete number. Haggerty [2009] explained that the truncation of the multi-rate series becomes an acceptable approximation when the final term is defined in an appropriate manner. Table 2.2 shows the series of mass transfer and porosities for spherical diffusion. The number of terms used is 10. The total field capacity (β_{tot}) is fixed to 1.0 and the apparent pore diffusion (D_p/a^2) is set to 0.0023. These properties

TABLE 2.1: Physical parameters used for the illustrative simulations

Parameter	Value
Flow problem	
Average hydraulic gradient $[-]$	0.01
Longitudinal dispersivity $[m]$	0.05
Transversal dispersivity in the horizontal plane $[m]$	0.01
Transversal dispersivity in the vertical plane $[m]$	0.005
Porosity $[-]$	0.3
Heterogeneous field	
Variogram type	spherical
Geometric mean of ln K $[m/d]$	3.55
Variance of ln K	2.5
Range, a $[m]$	10.0
Domain discretization	
Number of cells in x direction, $n_x \times n_y \times n_z$	$300 \times 250 \times 100$
Cell dimension, $\Delta_x \times \Delta_y \times \Delta_z$ $[m \times m \times m]$	$0.4 \times 0.4 \times 0.4$

TABLE 2.2: Multi-rate Series for spherical diffusion[a]

	α_{ij}	β_{ij}[b]
for j $= 1, \ldots, N_{im} - 1$	$j^2\pi^2 \left(D_a/a^2\right)_i$	$\dfrac{6}{j^2\pi^2}(\beta_{tot})_i$
for j $= N_{im}$	$\dfrac{15 \left(D_a/a^2\right)_i \left[1 - \sum_{j=1}^{N_{im}-1} \dfrac{6}{j^2\pi^2}\right]}{1 - \sum_{j=1}^{N_{im}-1} \dfrac{90}{j^4\pi^4}}$	$\left[1 - \sum_{j=1}^{N_{im}-1} \dfrac{6}{j^2\pi^2}\right](\beta_{tot})_i$

[a] After Haggerty and Gorelick [1995].

[b] Where $(\beta_{tot})_i = \dfrac{\phi_{im} R_i^{im}}{\phi_m R_i^m}$ is the capacity ratio for a specie i.

were chosen from the review of mass transfer data given by Haggerty et al. [2004]. Mass transfer parameters are summarized in Table 2.3.

The degradation rates of contaminants in aquifers can substantially vary in space [Allen-King et al., 2006] due to, for instance, changes in the bacteria activity responsible for biodegradation [e.g., Fennell et al., 2001; Sandrin et al., 2004]. To represent this, we consider that a perfect negative linear correlation between ln K and the decay rates exist [Miralles-Wilhelm and Gelhar, 1996; Cunningham and Fadel, 2007]. We admit this way that small decay rates relate to high ln K values and vice versa. This can happen

TABLE 2.3: Reaction parameters used for the illustrative simulations

Parameter	Value			
Biochemical (mobile domain)	PCE	TCE	DCE	VC
Mean first-order decay, k_{i0} $[d^{-1}]$	0.0355	0.0055	0.0352	0.0206
Miminum first-order decay, min(k_{i0}) $[d^{-1}]$	0	0.001	0.00035	0.0013
Maximum first-order decay, max(k_{i0}) $[d^{-1}]$	0.071	0.01	0.07	0.04
First-order decay coefficient of variation $[-]$	0.19	0.16	0.19	0.18
Yield coefficient, $y_{i/j}$ $[mol\ mol^{-1}]$	$\times$	0.79	0.74	0.64
Retardation factor, R_{i0} $[-]$	7.1	2.9	2.8	1.4
Multirate Mass Transfer				
Type	spherical diffusion			
Number of multi-rate series, N_{im}	10			
Total capacity ration, β_{tot}	0.17			
Apparent pore diffusion, D_p/a^2	0.0023			

for instance when water fluxes can effectively deplete electron acceptors/donors in the porous medium [Cunningham and Fadel, 2007]. The minimum and maximum values of PCE, TCE, DCE and VC decay rates were defined based on the range of possible values provided by the U.S. Environmental Protection Agency as a support to decision makers [Environmantal Protection Agency (EPA), 1999; , EPA]. Thus, decay rates reflect those obtained in several field sites and laboratory observations. The statistics of the decay rates are given in Table 2.3. The spatial distribution of the lnK and the decay rates in the mobile domain is shown in Figure 2.4. Two different conceptual models for the degradation in the immobile domain were considered. The first model assumes that degradation is not taking place in the immobile domain. This represents for instance the presence of small clay layers or pods in the aquifer, preventing bacteria to move and reproduce effectively. The second model considers the enhancement of degradation due to the existence of an active biofilm at the pore scale. In this case, the decay rate in the immobile domain is assumed to be 10 times larger than in the mobile domain.

2.6.2 Results and Discussion

The distribution of mobile and immobile particles simulated with the proposed random walk method is respectively shown in Figure 2.5 and 2.6 for two different times. The species compound is denoted by the particle color. The particle size is proportional to

the log of the cancer potency factor to visually display not only the density of particles (concentrations) but also the potential threat that these contaminants pose to human health. Important differences between the two conceptual models can be distinguished. The biofilm model clearly displays an enhancement of degradation which now mostly occurs in the immobile domain. Comparing the two models, we see that, in the biofilm model, a larger portion of the PCE has been already transformed into daughter products at time t=160 d. This means that daughter products can now be produced at earlier times and closer to the source area than expected from the mere diffusion of products into clay regions. This has important consequences for risk assessment. In heterogeneous porous media without local mass transfer effects, Henri et al. [2015] have demonstrated that the hot spot of the risk posed by a chemical mixture (co-existence of the original pollutants and their daughter products) depends on the joint effect of degradation, advection and toxicity. Results here show that the conceptualization of the immobile domain as an active degradation region can largely complicate the quantification and interpretation of human health risk.

The concentration breakthrough curves of all the species obtained at two different control planes during the simulations are shown in Figure 2.7. Results show that the biofilm model and the clay model give also very distinct signals. The clay model displays breakthrough curves with long tails due to rate-limited mass transfer. In this model, particles can be temporally trapped in the immobile domain by diffusion without undergoing degradation in this region. These particles will be capable to back diffuse into the mobile region at a later time. However, in the biofilm model, these trapped particles can be transformed into daughter products. This process prevents tailing and increases the amount of degradation products that can be transferred later on by diffusion into the mobile domain. This explains why the breakthrough curves in the biofilm model display more peaked distributions with more mass and less tailing.

2.7 Conclusions

The interaction between the spatial variability of aquifer properties, mass transfer and chemical reactions often complicates reactive transport simulations. It is well documented that hydro-biochemical properties are ubiquitously heterogeneous and that rate-limited

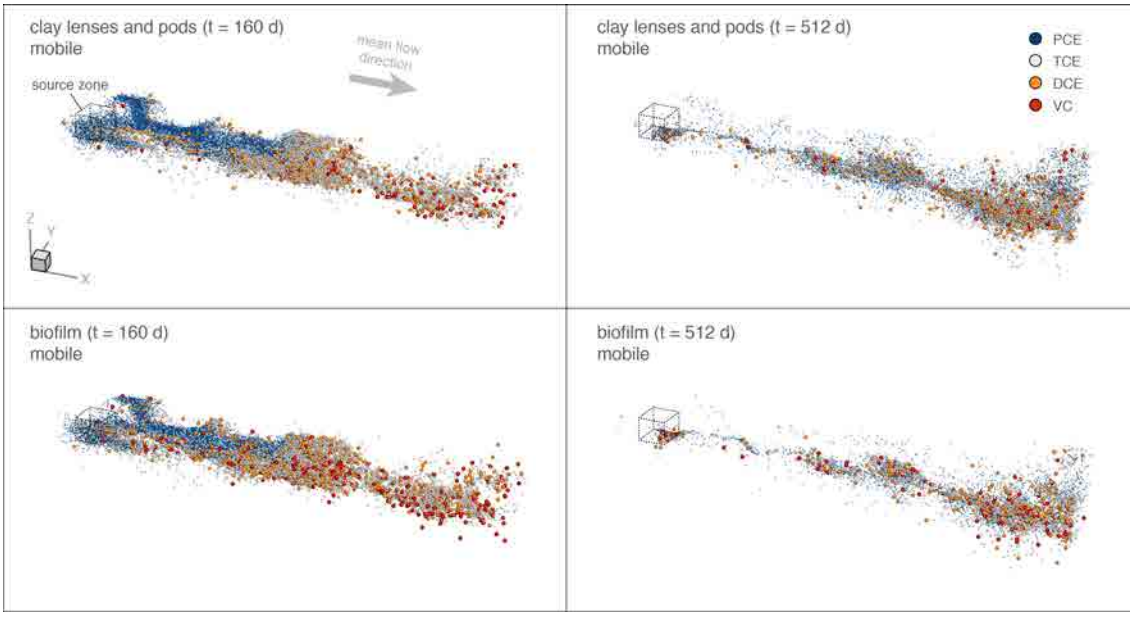

FIGURE 2.5: Snapshots of the plume of mobile particles illustrating the impact of degradation in the immobile domain at t=160 days (left hand frames) and t=512 days (right hand frames). Blue spheres represent PCE particles; silver spheres represent TCE particles; golden spheres represent DCE particles; and red spheres represent VC particles. The size of the spheres are proportional to the log of the cancer potency factors related to the species. In other terms, the toxicity of the compounds are correlated to the particle sizes.

mass transfer typically leads to the conceptualization of an aquifer as a multi-porosity system. In this conceptual model, contaminants can be transferred to a number of immobile water regions so as to represent different phenomena observed at multiple scales, i.e., diffusion into stagnant water at the pore-scale, diffusion into biofilms attached to soil surface, diffusion into low permeability inclusions at the centimeter to meter scale, and diffusion into aquitards or the rock matrix of a fractured system. Importantly, the chemical reactions taking place in these mobile/immobile water regions can be substantially different between each other. Along this line, we have presented a random walk solution that is capable to efficiently simulate multi-rate mass transfer and first-order network reactions in heterogeneous porous media without restrictions in the spatial variability of biochemical and hydrodynamic properties. First-order rate coefficients vary in space and the type of water region involved. The approach is based on the development of transition probabilities that describe the likelihood that particles belonging to a given species and mobile/immobile domain at a given time will be transformed into another species

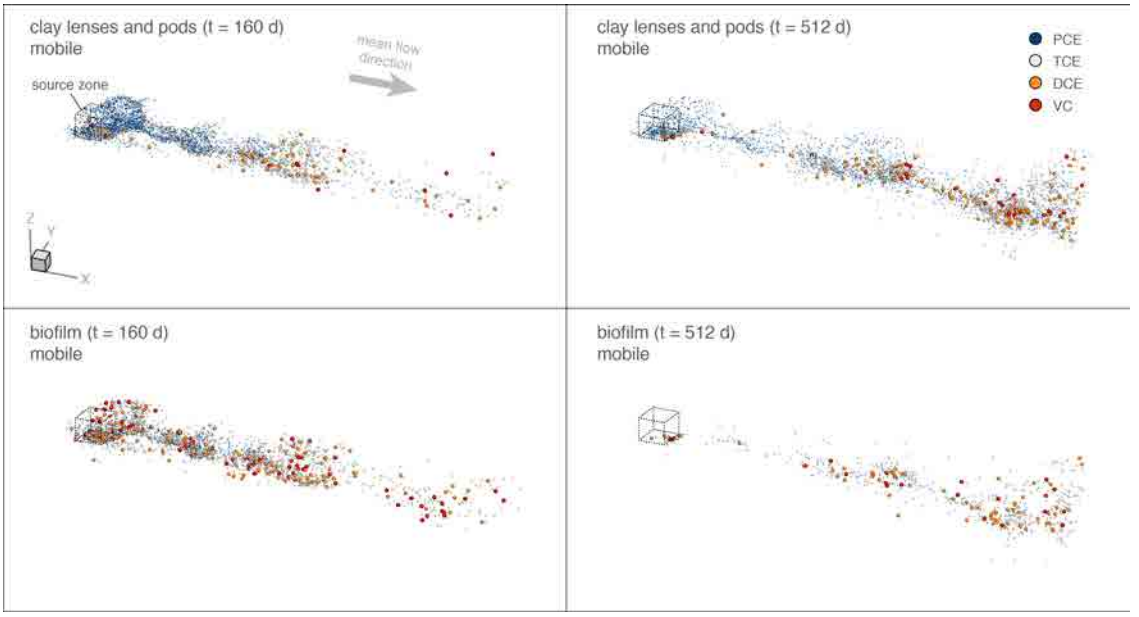

FIGURE 2.6: Snapshots of the plume of immobile particles illustrating the impact of degradation in the immobile domain at t=160 days (left hand frames) and t=512 days (right hand frames). Blue spheres represent PCE particles; silver spheres represent TCE particles; golden spheres represent DCE particles; and red spheres represent VC particles. The size of the spheres are proportional to the log of the cancer potency factors related to the species. In other terms, the toxicity of the compounds are correlated to the particle sizes.

and mobile/immobile domain afterwards. This is important for assessing the risk posed by a large variety of chemical systems that otherwise suffer from numerical problems in dealing with heterogeneities during reactive transport modeling, e.g., the degradation of chlorinated solvents, the decay of radioactive species, and the transformation of pesticides, organic phosphates and nitrogen in the environment. The method is limited to first-order network reactions.

The approach is used to investigate the joint effect of network reactions and mass transfer on the spatiotemporal behavior of the sequential degradation of tetrachloroethylene(PCE). Transition probabilities show that a double peak of daughter products can occur when the degradation capacity in the immobile domain is relatively small. This late rebound of concentrations is not driven by any change in the flow regime (e.g., pumping

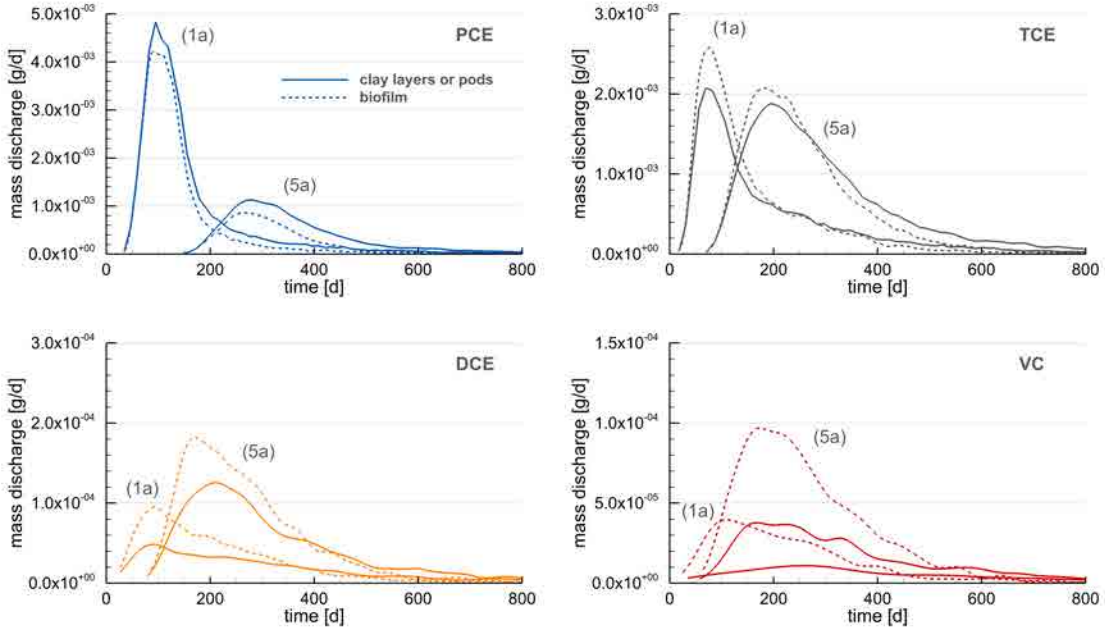

FIGURE 2.7: Breakthrough curves of the four chlorinated solvents (PCE, TCE, DCE and VC) at a distance of 1 and 5 variogram ranges from the source for the two degradation modes (active biofilms and clay pods).

ceases in the pump-and-treat remediation strategy) but due to the natural interplay between mass transfer and chemical reactions. To illustrate that the method can simultaneously represent mass transfer, spatially varying properties and network reactions without numerical problems, we have simulated the degradation of PCE in a three-dimensional fully heterogeneous aquifer subjected to rate-limited mass transfer. Two types of degradation modes were considered to compare the effect of an active biofilm with that of clay pods in the aquifer. Both hydraulic conductivity and biochemical parameters were considered spatially variable and described at high resolution. Results of the two scenarios display significant differences. Biofilms that promote the degradation of compounds in an immobile region are shown to significantly enhance degradation, rapidly producing daughter products and less tailing.

PART II

PROBABILISTIC HUMAN HEALTH RISK ASSESSMENT FOR COMPLEX CONTAMINATION SCENARIOS

La poetisa, 1940 by Joan Miro

CHAPTER 3

Probabilistic Human Health Risk Assessment of Degradation-Related Chemical Mixtures in Heterogeneous Aquifers: Risk Statistics, Hot Spots and Preferential Channels

Contents

Henri, C. V., D. Fernàndez-Garcia and F.P.J. de Barros (2015), Water Resour. Res, doi: 10.1002/2014WR016717.

3.1 Introduction

Monitored natural attenuation is an attractive cleanup technique commonly used to remediate organic and inorganic groundwater contaminants in field sites where biogeochemical conditions favor natural processes that degrade or immobilize harmful contaminants [MacDonald, 2000; Kitanidis and McCarty, 2012]. However, in some cases, before reaching a harmless chemical form, intermediate degradation products can constitute new noxious chemical compounds not necessarily less toxic than their parent product. In this situation, the original pollutants and their daughter products are susceptible to co-exist in the aquifer forming an hazardous chemical mixture composed of products of different toxicity [Environmantal Protection Agency (EPA), 2000]. This renders the quantification and interpretation of human health risk a non trivial and challenging task.

The complexity associated with human health risk assessment for chemical mixtures stems from the interaction between aquifer heterogeneity, its uncertainty and the contaminant conditions (source characteristics, mixture composition, toxicity, and biochemical properties). The spatial heterogeneity of the hydrogeological properties will dictate the relative importance of the degradation products to the total human health risk. In this context, the variability of the hydraulic properties typically leads to preferential flow channels and low permeability areas where contaminants can be temporarily trapped by rate-limited mass transfer [e.g., Gomez-Hernandez and Wen, 1998; Zinn and Harvey, 2003; Bianchi et al., 2011]. The formation of these fast flow channels is typically associated with the presence of well-connected, highly permeable geological bodies or structures that can concentrate flow and solute transport [e.g., Knudby and Carrera, 2005; Fernàndez-Garcia et al., 2010; Fiori and Jankovic, 2012; Renard and Allard, 2013]. These geological features are difficult to model since characterization data are scarce and limited by financial budgets. Therefore, risk predictions associated with aquifer contamination are subject to uncertainty [e.g., Rubin et al., 1994; Maxwell and Kastenberg, 1999].

Incorporating hydrogeological uncertainty in human health predictions has been a topic of intense research in the past [e.g., Andričević and Cvetković, 1996; Maxwell and Kastenberg, 1999; de Barros and Rubin, 2008; Cvetković and Molin, 2012; Rodak and Silliman, 2012; Andričević et al., 2012; Siirila and Maxwell, 2012; Atchley et al., 2013; de Barros and Fiori, 2014]. Probabilistic risk models allow one to determine the likelihood of risk

exceeding a given regulatory threshold value [Tartakosky, 2007], to delineate the spatial distribution of a plume for monitoring adaptation or intensification [James and Gorelick, 1994; Maxwell et al., 1999; Smalley et al., 2000; Maxwell et al., 2008; Fernàndez-Garcia et al., 2012] and to better allocate characterization efforts to reduce the overall uncertainty of a given environmental performance metric [e.g., de Barros et al., 2009]. Most of the studies related to probabilistic risk analysis focused on the evaluation of human health risk posed by a single toxic compound.

Stochastic methods account for parametric uncertainty by considering aquifer parameters to be random space functions [Rubin, 2003]. In general, the computational effort associated with stochastic simulations of multi-components reactive transport in three-dimensional heterogeneous aquifers has often limited risk analysis to simple scenarios. For example, a human health risk model related to multi-species groundwater contamination was reported by Benekos et al. [2006], who used a biochemical model to evaluate the human heath risk response to a bioremediation scenario in a two-dimensional aquifer contaminated by chlorinated solvents. Siirila et al. [2014] investigated the total risk posed by the mobilization of metals from the leakage of CO_2. To reduce computational needs, the multi-species reactive transport problem was tackled using a two-step approach that combined a simple one-dimensional geochemical model with fully three-dimensional transport simulations and sorption in local equilibrium. The role of kinetics was later on analyzed by Atchley et al. [2014], who used a simplified streamline approach. Despite the large body of literature related to human health risk assessment, there are research needs to further understand the joint effect of degradation-related chemical mixtures and physical heterogeneity on human health risk.

Another factor that can influence risk predictions of chemical mixtures is the contaminant release behavior at the source zone. The importance of the source behavior is an aspect often disregarded in risk management. However, previous works demonstrated that a mass release proportional to local groundwater fluxes shows a strong and persistent impact on the contaminant spread, concentration amplitude and peak predictability [Janković and Fiori, 2010]. We hypothesize that this source behavior, together with the heterogeneous structure of the aquifer, will play a significant role in the health risk.

Within this context, this work focuses on improving our understanding of how heterogeneity (and connectivity) and the contaminant injection mode contributes to the creation of high risk locations. To achieve our objective, we simulate high-resolution three-dimensional (3D) flow and multi-species reactive transport within a stochastic framework. Human health risk is spatially characterized by lower-order statistical moments and empirical probability density functions for each individual chemical species and the total chemical mixture. We show that the total risk posed by a chemical mixture can increase to a maximum at a critical distance controlled by a modified, toxicity-based, Damköhler number that accounts for the joint effect of contaminant mean travel times, reaction kinetics and chemical toxicity. Connectivity is shown to produce a non-trivial impact on risk measures, being potentially beneficial or detrimental depending on the proposed toxicity-based Damköhler number.

3.2 Problem Statement

This paper considers an aquifer contaminated by tetrachloroethylene (PCE), which is a common DNAPL product found in groundwater [Fay and Mumtaz, 1996]. PCE pure liquid is assumed to be already trapped (immobile) in the aquifer but slowly dissolving over time. This creates a long-term contamination plume downgradient. Under anaerobic conditions, chlorinated solvents dissolved in groundwater can undergo reductive dechlorination [Skeen et al., 1995; Jain and Criddle, 1995]. In such a case, PCE will be transformed into trichloroethylene (TCE), TCE will be degraded into *cis*-Dichloroethylene (DCE) (Dichloroethylene), DCE will react to produce vinyl chloride (VC) and, finally, VC will transform into a non-toxic compound, ethene. This constitutes a sequential reaction of the form PCE $\rightarrow$ TCE $\rightarrow$ DCE $\rightarrow$ VC $\rightarrow$ ethene. The four chlorinated compounds can cause a potential risk on human health that we aim to quantify here. PCE, TCE and DCE are categorized as probable human carcinogenic (e.g. limited evidence) by the Environmantal Protection Agency (EPA) [1997]. However, VC is categorized as a human carcinogen (sufficient human evidence for causal association between exposure and cancer) [Environmantal Protection Agency (EPA), 1997]. Parent and daughter species of different toxicity temporarily co-exist in a chemical mixture. A 3D snapshot of the contaminant and its daughter products is shown in Figure 3.1a. An illustrative example

of the spatial evolution of the human health risk for each chlorinated solvent can be seen in Figure 3.1b. Interestingly, a high risk zone can be expected far from the contaminant source.

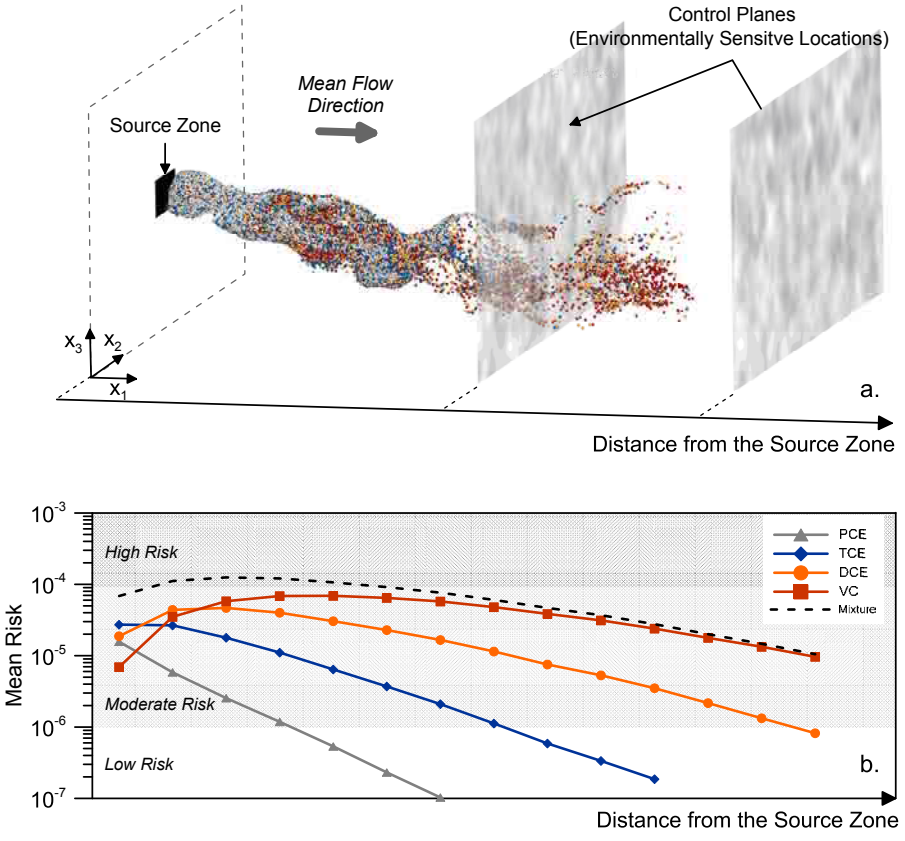

FIGURE 3.1: (a.) Snapshot of a contaminants mixture plume (grey: PCE, blue: TCE, orange: DCE, red: VC) approaching control planes and transported in a 3D heterogeneous hydraulic conductivity field. (b.) Expected risk profile along the contaminated site.

Given that a significant fraction of DNAPL mass is likely to remain in aquifers even after a given remediation treatment, Soga et al. [2004] proposed to consider what is an acceptable contamination level not based on the amount of DNAPL mass removed from the site but by measurements of dissolved concentrations downgradient. They called this methodology *the mass flux approach*. Here, following this strategy, the estimation

of human health risk is strictly based on integrated concentration breakthrough curves, which are obtained at x-control planes perpendicular to the mean flow direction.

3.2.1 Human Health Risk Model

In this work, we will focus on quantifying cancer risk due to chronic exposure to chlorinated solvents released in a spatially heterogeneous aquifer. The route of exposure is assumed to be only direct ingestion. Following the human health risk assessment guidance [Environmantal Protection Agency (EPA), 1989], carcinogenic health risk can be evaluated by a Poisson model for individual cancer occurrence, where $\mathrm{R}_i(x)$ is the incremental lifetime cancer risk (ILCR) to a contaminant i at a given longitudinal position x where the control plane is located. The ILCR can be formally written as

$$\mathrm{R}_i(x) = 1 - \exp[-ADD_i(x) \times CPF_i], \tag{3.1}$$

where CPF_i [kg d/mg] is the metabolized cancer potency factor related to the carcinogenic contaminant i, and ADD_i [mg/(kg d)] is the average daily dose of contaminant i. Here, we will only consider human exposure by direct ingestion so that

$$ADD_i(x) = \bar{c}_i(x) \left[\frac{IR}{BW}\right] \frac{ED \times EF}{AT}, \tag{3.2}$$

where IR is the ingestion rate of water [L/d], BW is the body weight [kg], AT is the expected lifetime [d], ED is the exposure duration [y], and EF is the daily exposure frequency [d/y]. These parameters are assumed constant and defined in Table 3.1. The key component in the evaluation of the average daily dose is $\bar{c}_i$ [mg/L], which is the critical (flux-averaged) concentration of the pollutant i at an environmentally sensitive location x. This parameter $\bar{c}_i$ can be seen as the maximum running averaged concentration of the concentration breakthrough curve obtained at the control plane (CP) over the exposure duration ED [Maxwell and Kastenberg, 1999]. Note that, by convention, lowercase and uppercase concentrations will respectively denote flux-averaged and resident concentrations throughout this work [Parker and van Genuchten, 1984]. The maximum running averaged concentration is mathematically expressed by

TABLE 3.1: Risk parameters

Parameter	Value			
Ingestion rate, IR [l/d]	1.4			
Body weight, BW [kg]	70.0			
Exposure duration, ED [y]	30.0			
Exposure frequency, EF [d/y]	350.0			
Average time of the expected lifetime, AT [d]	25550.0			
	PCE	TCE	DCE	VC
Cancer potency factor, CPF_i [kg d/mg]	0.0021	0.011	0.6	1.5
Maximum Contaminant Level, MCL_i, [μg/L]	5.0	5.0	7.0	2.0

$$\bar{c}_i(x) = \max_{t>0} \left\{ \frac{1}{ED} \int_t^{t+ED} c_i(\tau; x) d\tau \right\}, \tag{3.3}$$

where $c_i(\tau; x)$ is the flux-averaged concentration defined as the ratio of the mass discharge to the volumetric water flux at a control plane location x. We note that flux-averaged concentrations have been widely used in previous human health risk analysis [Andričević and Cvetković, 1996; de Barros and Rubin, 2008].

Another important metric is the total risk associated with the chemical mixture (e.g., PCE, TCE, DCE and VC). The total risk $\mathrm{R_T}$ defines the effective threat posed by the exposure to a chemical mixture. When contaminant concentrations are low enough (lower than 300 ppm), the total risk can be satisfactorily determined by the sum of individual risks [Speek, 1981],

$$\mathrm{R_T}(x) = \sum_{i=1}^{4} \mathrm{R}_i(x). \tag{3.4}$$

Stake-holders and regulators sometimes prefer to determine aquifer remediation goals in terms of maximum contaminant levels (MCLs), defined by the United States Environmental Protection Agency as the legal threshold limit of a contaminant concentration allowed in public water systems. To analyze this scenario, we also investigate the spatiotemporal behavior of the probability of exceedance of MCLs associated to each chemical species i,

$$\xi_{c_i}(x,t) = \mathrm{Prob}[c_i(t;x) > \mathrm{MCL}_i]. \tag{3.5}$$

From a practical perspective, an important issue for risk assessors is the characterization of *hot spots* and *hot moments*. A hot spot is typically defined as an area of elevated risk [Dilley et al., 2005]. The level at which the risk is considered elevated is usually determined by stakeholders and end-users during the risk assessment and decision making process. This concept will be used here to qualitatively highlight an area of maximum risk. When dealing with the ILCR, which is an integrated measure over time that only depends on x (see equation (3.3)), the corresponding hot spot will refer to the x-interval with maximum ILCR values. Instead, when dealing with the probability of exceedance of MCLs, the hot spot will indicate the spatial window for which $\xi_{c_i}(x,t)$ reaches a relatively large value at any given time. The temporal persistence of these high values is denoted as the *hot moment*, which is only an intrinsic property of $\xi_{c_i}(x,t)$. Importantly, results will show that the location of critical hot spots can drastically change with the risk metric employed (probability of exceedance of MCLs or increased lifetime cancer risk).

3.2.2 Flow and Transport Model

In order to determine $\bar{c}_i$ (3.3) we need to simulate flow and reactive transport. In this work, we consider a 3D confined aquifer. The Cartesian coordinate system is given by $\mathbf{x} = (x, y, z)$. The domain is a rectangular prism with length $L_x = 1600$ m, width $L_y = 800$ m, and thickness $L_z = 400$ m. The aquifer has constant head boundaries at $x = 0$ m and $x = 1600$ m and no-flow conditions at the remaining boundaries. Groundwater flow is at steady-state and driven by a mean horizontal hydraulic gradient given by $J = 0.07$ and oriented in the x direction. Groundwater fluxes are described by Darcy's law through,

$$\mathbf{q}(\mathbf{x}) = -K(\mathbf{x})\nabla h(\mathbf{x}), \tag{3.6}$$

where $\mathbf{q}$ [m d^{-1}] is the specific discharge, h [m] is the hydraulic head, and K [m d^{-1}] is the hydraulic conductivity at the $\mathbf{x}$ location. The hydraulic conductivity is assumed locally isotropic but spatially heterogeneous. In this case, the groundwater flow equation is

$$\nabla \cdot [K(\mathbf{x})\nabla h(\mathbf{x})] = 0. \tag{3.7}$$

The reductive dechlorination of PCE due to biodegradation can be approximated by a sequential first-order reaction kinetic model [e.g., Clement, 2001; Burnell et al., 2014]. This model assumes that contaminant concentrations are relatively low (below the Michaelis half-saturation constant) [Cunningham and Mendoza-Sanchez, 2006]. Reactive transport of PCE and its degradation products can be described by the following system of partial differential equations

$$\phi\mathcal{R}_i\frac{\partial C_i}{\partial t}-\nabla\cdot(\phi\mathbf{D}\nabla C_i)+\nabla\cdot(\mathbf{q}C_i)=y_i k_{i-1}\phi C_{i-1}-k_i\phi C_i+s(\mathbf{x},t)\delta_{i1},\ \forall i=1,\ldots,4, \quad (3.8)$$

where ϕ is the porosity, $\mathbf{D}$ [m^2 d^{-1}] is the hydrodynamic dispersion tensor, and δ_{i1} is the Kronecker delta function. The dispersion tensor $\mathbf{D}$ is oriented in the direction of flow with principal components determined by $D_L = \alpha_L v$, $D_{TH} = \alpha_{TH} v$, and $D_{TV} = \alpha_{TV} v$. Here, v [m/d] is the velocity of groundwater, α_L [m] is the longitudinal dispersivity, α_{TH} [m] is the horizontal transverse dispersivity, and α_{TV} is the vertical transverse dispersivity [m]. Dispersivity coefficients are assumed constants for all species and molecular diffusion is neglected. For each species i, $\mathcal{R}_i$ [$-$] is the retardation factor, C_i [g m^{-3}] is the resident concentration in the liquid phase, k_i [d^{-1}] is the first-order contaminant degradation rate constant, and y_i [g g^{-1}] is the effective yield coefficient for any reactant or product pair. These coefficients are defined as the ratio of mass of species i generated to the amount of mass of species $i-1$ consumed. Sorption reactions are assumed in local equilibrium and follow a linear sorption isotherm [Roberts et al., 1986]. Transport equations consider that no biodegradation occurs in the sorbed phase. Nevertheless, we note that other scenarios can be simulated by properly redefining the degradation rates.

The aquifer is considered to be initially clean (zero concentration of PCE and its degradation products at time $t = 0$) but subject to a PCE time-dependent source dissolution rate $s(\mathbf{x}, t)$ (mass per unit volume and time). This term represents the mass of dissolved PCE leaving the source zone through a rectangular area A_s. This area is centered within a vertical plane located at $x_{inj} = 200$ m and has a size of 96×48 m^2 (see Figure 3.1).

3.2.3 Source Mass Release Model

Several mass-depletion models have been proposed in the literature to effectively represent DNAPL dissolution at a contaminated site. Among them, we employ the power-law empirical model proposed by Rao et al. [2001] and Parker and Park [2004], which describes the relationship between the flux concentrations of the dissolved DNAPL leaving the source zone and the mass of DNAPL remaining in the source zone as

$$\frac{c_s(t)}{c_0} = \left(\frac{m(t)}{m_0}\right)^{\Gamma}, \tag{3.9}$$

where c_s is the averaged flux concentration of the dissolved DNAPL chemical (PCE) leaving the source zone, c_0 is the corresponding initial concentration, and Γ is the mass-depletion constant that accounts for changes in interfacial surface area as the source mass diminishes. Typically, Γ is larger than 1 for contaminated sites with finger-dominated residual DNAPL, and smaller than 1 for sites with prominence of DNAPL pools and lenses [Parker and Park, 2004]. This is due to the fact that finger-dominated sources generally exhibit higher initial mass transfer coefficients per unit mass than lens-dominated systems. Substituting (3.9) into the mass balance equation expressed at the source zone, the flux concentration of PCE leaving the source zone can be determined from Parker and Park [2004] as

$$c_s(t) = \frac{c_0}{m_0^{\Gamma}} \left\{ \frac{-Q_s c_0}{\lambda_s m_0^{\Gamma}} + \left(m_0^{1-\Gamma} + \frac{Q_s c_0}{\lambda_s m_0^{\Gamma}} \right) e^{(\Gamma-1)\lambda_s t} \right\}^{\frac{\Gamma}{1-\Gamma}}, \tag{3.10}$$

where m_0 is the initial mass of DNAPL at the source zone, Q_s is the groundwater volumetric discharge rate passing through the source zone, and λ_s is the first-order degradation constant of PCE at the source zone. Based on this, the time-dependent source dissolution rate $s(\mathbf{x}, t)$ can be written as

$$s(\mathbf{x}, t) = q_s c_s(t)\, \delta(x - x_{inj}) \Omega(\mathbf{x} \in A_s), \tag{3.11}$$

where $q_s = Q_s/A_s$, Q_s is the total flow passing through A_s, and $\Omega(\mathbf{x} \in A_s)$ is an indicator function that is equal to one when $\mathbf{x} \in A_s$ and zero otherwise.

It is common in modeling studies to distribute the total discharge mass of DNAPL leaving the source zone homogeneously in the outlet source area. However, spatial variations in the aquifer hydraulic properties may suggest more complicated source behaviors [Parker and van Genuchten, 1984; Fure et al., 2006]. Two scenarios will then be considered in this work: A *classical mass injection mode* (CIM) related to a homogeneous distribution and a *flux-weighted injection mode* (FWIM) related to a flux weighted distribution of PCE at the outlet source area.

3.3 Methodology

A stochastic framework is used to account for the uncertainty in the hydraulic conductivity field, which is described as a random space function. In this work, health risk statistics are characterized through numerical Monte Carlo simulations. Analytical stochastic approaches based on perturbation theory are available in the literature to estimate human health risk associated with individual species [e.g., Andričević and Cvetković, 1996; de Barros and Rubin, 2008; de Barros and Fiori, 2014] but few works have assessed the risk posed by chemical mixtures in highly heterogeneous 3D aquifers. For this work, the state variables (i.e., ILCR) are characterized by their statistical moments and empirical probability density functions (*pdf*s). Monte Carlo simulations consist of four sequential steps: (1) stochastic generation of equiprobable hydraulic conductivity fields; (2) solve the flow problem associated to each hydraulic conductivity field; (3) solve the reactive-transport problem for each flow field; and (4) estimate the corresponding ILCR at different control planes.

The log-conductivity field, denoted as $Y(\mathbf{x}) = \ln K(\mathbf{x})$, is considered to follow a multi-Gaussian random space function model characterized by an isotropic Gaussian covariance function with zero mean and an integral scale λ of 14.18 m. Two levels of heterogeneity of $Y(\mathbf{x})$ were explored: $\sigma^2_Y = 1$ and $\sigma^2_Y = 4$. These values were chosen to represent a mild and a highly heterogeneous aquifer scenario. The geostatistical parameters of the $Y(\mathbf{x})$ random field are summarized in Table 3.2. The domain is discretized into $400\times200\times100$ squared cells that form an 8 million cell problem. The Monte Carlo simulations considered 500 equiprobable realizations of the $Y(\mathbf{x})$ random field. The Monte Carlo convergence was

TABLE 3.2: Physical parameters adopted for simulating serial reaction transport in a 3D heterogeneous flow system

Parameter	Value
Flow problem	
Average hydraulic gradient [−]	0.07
Longitudinal dispersivity, α_L [m]	0.4
Transversal dispersivity in the horizontal plane, α_{TH} [m]	0.04
Transversal dispersivity in the vertical plane, α_{TV} [m]	0.01
Porosity, ϕ [−]	0.3
Heterogeneous field	
Variogram type	Gaussian
Mean of Y (Y=ln$K$) [m^2/d]	0.0
Variance of Y	1.0 and 4.0
Integral scales, λ_x=λ_y=λ_z [m]	14.18
Domain discretization	
Number of cells in x direction, n_x	400
Number of cells in y direction, n_y	220
Number of cells in z direction, n_z	100
Cell dimension, $\Delta_x \times \Delta_y \times \Delta_z$ [$m \times m \times m$]	4.0 × 4.0 × 4.0

controlled by analyzing the stabilization of the mean and variance of total risk. Figure 3.2 shows a satisfactory stabilization of the two first statistical moments after 100 realizations.

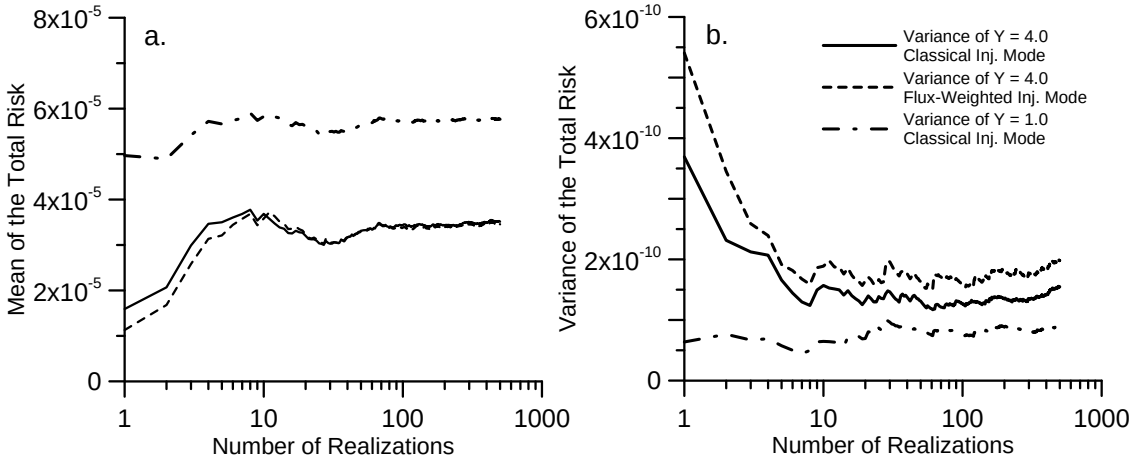

FIGURE 3.2: Monte Carlo convergence of the total mean increased lifetime cancer risk (Figure a.) and its variance (Figure b.) as a function of the number of realizations obtained at the control plane ζ=24.7 for the three different scenarios.

Table 3.3: Reaction parameters

Parameter	Value			
	PCE	TCE	DCE	VC
First order decay, k_i $[d^{-1}]$	0.0025	0.002	0.0015	0.001
Yield coefficient, y_i $[g\ g^{-1}]$	$\times$	0.79	0.74	0.64
Retardation factor, $\mathcal{R}_i$ $[-]$	7.1	2.9	2.8	1.4

For each $Y(\mathbf{x})$ realization, the groundwater flow equation (3.7) was first solved by means of the well-known finite difference code, MODFLOW [Harbaugh et al., 2000]. The multi-species reactive transport problem formed by PCE, TCE, DCE and VC was then simulated using the random walk particle tracking (RWPT) methodology using the RW3D code [Fernàndez-Garcia et al., 2005a]. This code has been recently adapted to efficiently simulate first-order network reaction systems [Henri and Fernàndez-Garcia, 2014]. RWPT simulates solute transport by injecting a large number of mass particles into the system. Particles move by following the velocity field obtained from the solution of the flow equation to simulate advection and adds a random displacement to simulate dispersion [e.g., Salamon et al., 2006a; Boso et al., 2013]. First-order network reactions are simulated by changing the species state assigned to each particle based on transition probabilities that depend on the biochemical properties of the species. The particle-tracking code can efficiently model such multi-species systems in heterogeneous conditions and at high resolution. We refer to Henri and Fernàndez-Garcia [2014] for further numerical details. Transport parameters are characterized by a constant porosity ($\phi = 0.3$), a longitudinal dispersivity of 0.4 m, a horizontal transverse dispersivity of 0.04 m, and a vertical transverse dispersivity of 0.01 m (see Table 3.2). Based on the review of field dispersion data by Gelhar et al. [1992], these grid-cell values of dispersivity were estimated as $\alpha_L \approx 0.1\Delta x$, and $\alpha_L/\alpha_{TH} \approx 10$ to account for subgrid heterogeneity. Biodegradation rates (k_i) are assumed constant in space and were chosen according to the range of possible first-order rate constants observed and summarized by the Environmantal Protection Agency (EPA) [1999]. The retardation factors were chosen according to the expected differences in mobility between the different chlorinated chemicals [Lu et al., 2011]. The adopted reaction parameters are depicted in Table 3.3.

A large number of PCE particles ($n = 10^5$) were instantaneously released at $\mathbf{x} \in A_s$. In terms of the correlation structure, the size of the source area A_s is $6.8\lambda \times 3.4\lambda$, which is

Table 3.4: Source zone mass transfer parameters

Parameter	Value
Power law, Γ $[-]$	2.0
Initial concentration, C_0 $[g/m^3]$	0.1
Initial mass, M_0 $[kg]$	300.0
Source first order decay rate, λ_S $[d^{-1}]$	$5{\times}10^{-4}$

similar to reported field conditions at the Borden and Cape Cod sites [e.g., Mackay et al., 1986; LeBlanc et al., 1991]. The first arrival time of particles passing through a set of control planes was recorded during the simulation, from which cumulative breakthrough curves were estimated, $c_i^h(t;x)$. The concentrations of all species $c_i(t;x)$ produced by a time-dependent injection were then estimated using the principle of superposition, which states that

$$c_i(t;x) = \int_0^t c_s(\tau) c_i^\delta(t-\tau;x) d\tau, \tag{3.12}$$

where $c_i^\delta(\tau;x)$ is the Dirac-input solution (instantaneous injection) of the concentrations associated with the $i-$th species. By discretizing the source term in step functions, $c_s(t) = c_{s,0}H(t) + \sum_{j=1} \Delta c_{s,j} H(t-t_j)$, being $H(t)$ the heaviside step function and $\Delta c_{s,j} = c_{s,j} - c_{s,j-1}$, equation (3.12) can be written as

$$c_i(t;x) = c_{s,0} c_i^h(t;x) + \sum_{j=1}^{t_j<t} \Delta c_{s,j} c_i^h(t-t_j;x), \tag{3.13}$$

where $c_i^h(t;x)$ is the cumulative breakthrough curve of the ith species obtained from a unitary mass source. The mass depletion model parameters are summarized in Table 3.4.

The distribution of particles in the source area followed the two injection modes previously discussed, (i.e., CIM and FWIM). The CIM injection mode injected the particles uniformly within the source area and the FWIM injection mode distributed the particles proportional to local cell fluxes.

3.4 Statistical Description of Risk

Computational results are organized as it follows: section 3.4.1 presents the probability of exceedance of the maximum contaminant levels (MCLs). Then, section 3.4.2 offers the statistical description of the total ILCR. The statistical description of the total ILCR is based on low-order statistics (ensemble mean and coefficient of variation) as well as on the full characterization of the *pdf*. The mean of the total ILCR, denoted here as $\langle \mathrm{R_T}(x) \rangle$, is a measure of the expected threat to the exposed population. Instead, the coefficient of variation of the total ILCR, given by $\mathrm{CV_{R_T}}(x) = \sigma_{R_\mathrm{T}}(x)/\langle \mathrm{R_T}(x) \rangle$, where σ_{R_T} is the standard deviation of the total ILCR, provides a measure of the degree of uncertainty in risk predictions.

We also analyzed the so-called survival or reliability function of the total risk ($\xi_{\mathrm{R_T}}$), i.e., the probability of exceedance of a given threshold R^*, denoted as $\xi_{\mathrm{R_T}}(x) = \mathrm{Prob}[\mathrm{R_T}(x) > \mathrm{R}^*]$. This function identifies the area at which the risk persists beyond a specified threshold normally defined by regulators. Typical values range between 10^{-4} and 10^{-6}. For the purpose of illustration, we set $\mathrm{R}^* = 10^{-5}$. In the following, results are presented in dimensionless variables. The longitudinal distance from the injection $(x - x_{inj})$ is normalized by the integral scale λ, i.e.,

$$\zeta = \frac{x - x_{inj}}{\lambda},$$

and the time elapsed from the beginning of the contamination is normalized by the expected time needed to travel an integral scale, i.e.,

$$\tau = \frac{t\, K_G J}{\lambda \phi},$$

where K_G is the geometric mean of the hydraulic conductivity, and J the hydraulic gradient.

3.4.1 Probability of Exceedance of MCLs

The visualization tool proposed here to analyze probabilities of exceedance of MCLs, i.e., $\xi_{c_i}(x,t) = \text{Prob}[c_i(t;x) > \text{MCL}_i]$, provides a useful information on the temporal and the spatial distribution of risk posed by the contamination. This graphical tool allows decision makers to identify the spatial range in which high values of $\xi_{c_i}(x,t)$ are predicted (*hot spots*) and the temporal persistence of these high values (*hot moments*). Figure 3.3 displays the spatiotemporal evolution of $\xi_{c_i}(\mathbf{x},t)$ for each chemical compound as a function of σ_Y^2 and the injection mode. Results show that the probability of exceedance is highly sensitive to the species of concern. The area limited by non-negligible probabilities of exceedance increases with decreasing MCL. Thus, the degradation product VC with the lowest MCL produces an extended region of low risk reliability both in space and time. The opposite occurs for the degradation product DCE with the highest MCL. An increase in σ_Y^2 leads to the dilution and spreading of the probabilities of exceedance in all contaminant products. Consequently, the threat is smaller in magnitude but occupies a larger spatiotemporal region. Nevertheless, the spreading mostly takes place in the spatial dimension ζ. Remarkably, concentrations can exceed the MCLs during a larger period of time with smaller σ_Y^2 (compare frames a-d with e-h).

The type of injection has substantial consequences on the spatiotemporal evolution of $\xi_{c_i}(\mathbf{x},t)$. A flux-weighted injection can drastically increase the magnitude and area occupied by the non-negligible probability of exceedance. This seems to suggest that the dilution of the contaminant is limited by the flux-weighted injection mode. From a different perspective, we highlight that this graphical tool permits to clearly identify hot spots and hot moments. In this context, it is interesting to see that the area of $\xi_{c_i}(x,t)$ reaching a given predefined threshold at any given time (hot spot) and its corresponding temporal persistence (hot moment) decreases with heterogeneity (σ_Y^2). On the contrary, the flux-weighted injection mode promotes larger hot spots and hot moments.

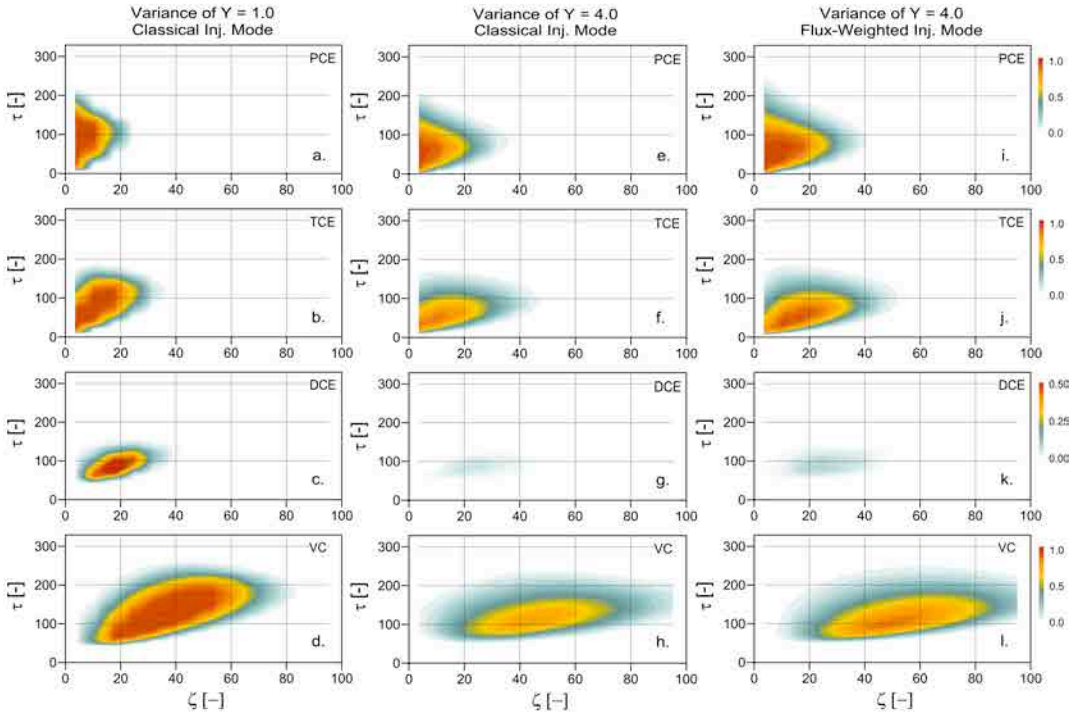

FIGURE 3.3: Risks of exceedance of the MCLs as a function of the normalized time τ and the normalized distance ζ related to a variance of Y of 1.0 (left hand, frames a to d), a variance of Y of 4.0 for a classical Injection Mode (center, frames e to h), and a variance of Y of 4.0 for a flux-weighted injection mode (right hand, frames i to l).

3.4.2 Total Increased Lifetime Cancer Risk

3.4.2.1 Low-order Moments and Reliability

Additive risk models determine that the ILCR posed by a chemical mixture is the sum of the risk posed by each chemical species in the chemical mixture, equation (3.4). The total risk low-order moments are shown in Figure 3.4. Results demonstrate that, when the toxicity of intermediate products is larger than that of the parent species, the mean total risk can increase to a maximum (R_c) at a critical position (x_c). The area with elevated risk surrounding this critical position is denoted as a *hot spot*. Between the contamination area ($x = x_{inj}$) and the critical position ($x = x_c$) the rate of risk generation due to the

formation of toxic intermediate products exceeds the rate of risk reduction due to self-purification (natural attenuation). Eventually, the total risk decreases to near zero at larger distances meaning that the aquifer can remediate itself by natural attenuation.

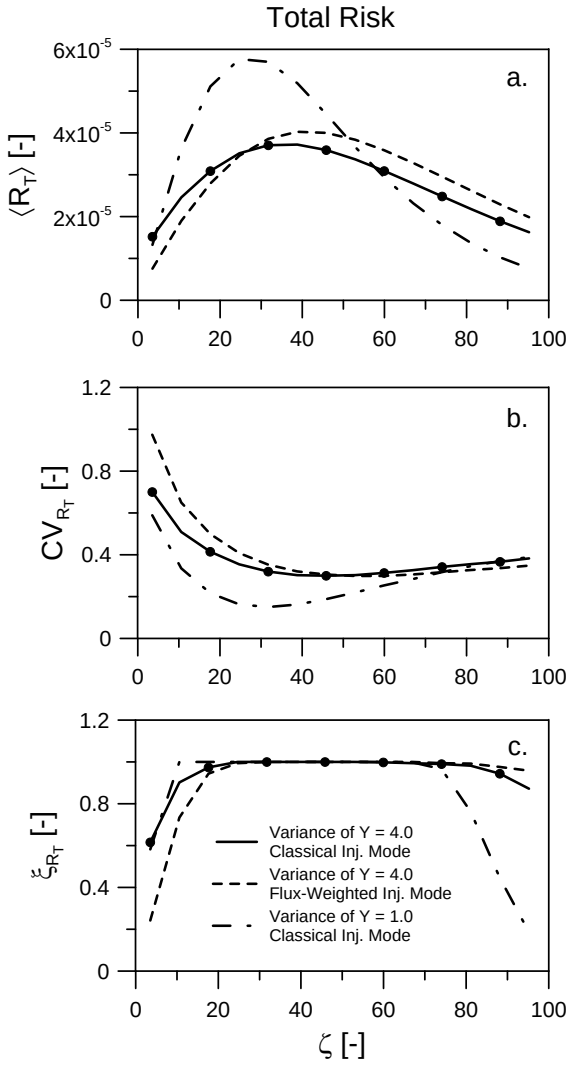

FIGURE 3.4: Longitudinal profile of the expected mean of the total increased lifetime cancer risk (Figure a.), its coefficient of variation (Figure b.), and its reliability function (Figure c.).

Results also indicate that careful attention should be paid to the risk metrics employed during the management of chemical mixtures at a hazardous waste site. A completely different depiction of the critical hot spot can be obtained by using the probability of exceedance of MCLs. For instance, section 3.4.1 shows that the largest probability of

exceedance of the MCL associated with the parent species PCE is situated nearby the source zone and far from the critical position x_c.

The critical position x_c depends on the joint effect of PCE and degradation products on the total risk. The relative contribution of each species is depicted in Figure 3.5. The individual risk posed by PCE and TCE is 2 orders of magnitude lower than DCE and VC. Consequently, the contribution of PCE and TCE to the total risk is negligible and the total mean risk is mainly controlled by DCE and VC. Figure 3.5b displays the uncertainty in risk predictions. Interestingly, the coefficient of variation ($\mathrm{CV}_{\mathrm{R}_T}$) shows a strong inverse correlation with its mean value. Thus, low risk values nearby the source zone have large uncertainties and high risk values close to the critical position are the most reliable.

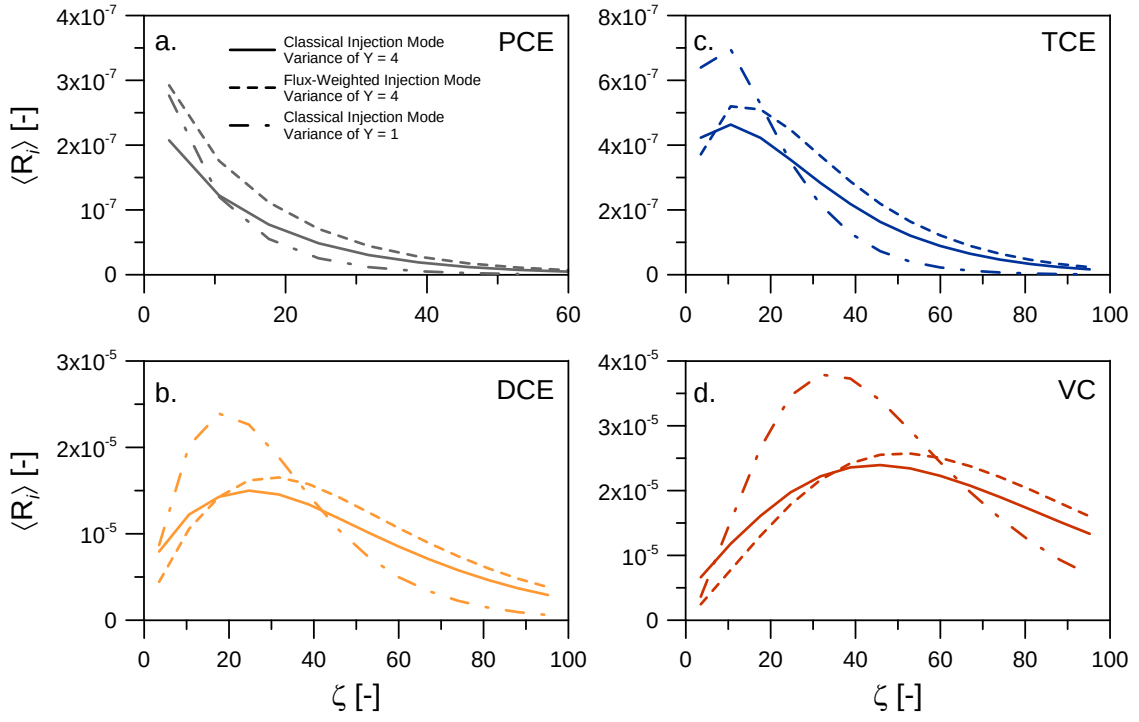

FIGURE 3.5: Influence of the variance of Y and of the injection mode on the longitudinal distribution of the individual mean risk, for the compounds PCE (grey) and TCE (blue), Figures a. (top), and the compounds DCE (orange) and VC (red), Figures b (bottom). Distances from the injection are normalized by the integral scale as $\zeta = (x_{cp} - x_{inj})/\lambda$.

The probability to exceed a mandated risk threshold $\xi_{\mathrm{R_T}}(\mathbf{x})$ follows the total mean risk

behavior (Figure 3.5c) but exhibits a larger area, centered at the critical position, within which the risk persists beyond a specified threshold. That is to say that the area required to accomplish an apparent decontamination can be large in practical situations. Moreover, even though the mean risk at the source zone is close to the critical threshold ($R^* = 10^{-5}$), we note that the probability to exceed R^* is still substantial. An effect that seems attributable to the high uncertainty attained in this region.

Heterogeneity favors the development of preferential channels through which contaminants can rapidly be transported from the source zone to further away distances [Gomez-Hernandez and Wen, 1998; Zinn and Harvey, 2003]. Consequently, Figure 3.4a shows that the critical distance increases with σ_Y^2. At the same time, the maximum risk value diminishes with σ_Y^2 due to the combination of enhanced macro-dispersive effects and the subsequent dilution of concentrations at control planes. Large σ_Y^2 not only diminish the maximum total risk attained at the critical position but also spreads the risk over a wider area (Figure 3.4a). The CV_{R_T} analysis shows also a significant sensitivity to the degree of heterogeneity (Figure 3.4b), especially, close to the source and at the hot spot where the uncertainty in risk predictions increases with σ_Y^2. Finally, heterogeneity causes the persistence of large ξ_{R_T} values over a wider area (Figure 3.4c).

A flux-weighted injection mode (particles injected proportional to local fluxes) initially concentrates more mass in preferential flow channels [Vanderborght et al., 1998]. This effect precludes the initial mixing of the contaminant nearby the injection location, causing an increase in the maximum total mean risk and the critical distance (see Figure 3.4a). As a result, the probability to exceed a mandated risk threshold is shifted away from the source zone during a flux-weighted injection (Figure 3.4c).

3.4.2.2 Probability Density Functions

The total risk-*pdf*s are shown in Figure 3.6 as a function of σ_Y^2 and the injection mode for three different normalized traveled distances (ζ=3.5, 25.0 and 60.0). Results demonstrate that biodegradation can effectively modify the form of the risk-*pdf*s. These *pdf*s are highly asymmetric, positively skewed nearby the source zone (ζ=3.5 on Figure 3.6a) due to the high probability of occurrence of the less toxic compounds in this region. The total risk-*pdf*s seem to approach a Gaussian-like behavior with travel distance (Figure

3.6 frames b and c). The effect of heterogeneity on the total risk-*pdf*s is also shown in Figure 3.6. Close to the source zone (ζ=3.5), a large $\sigma^2_{Y'}$ yields residual but persistent probabilities of high risk.

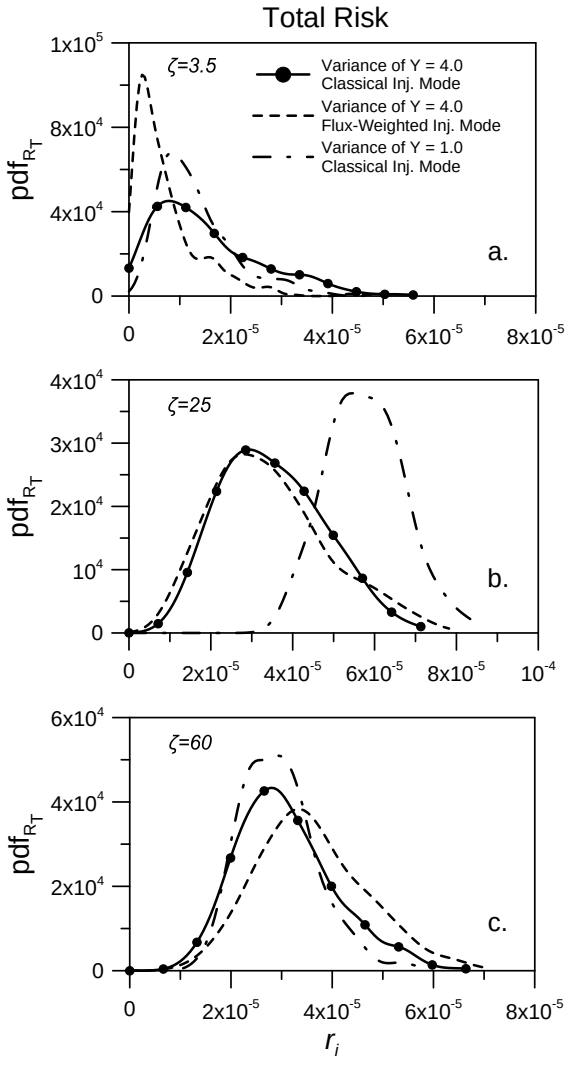

FIGURE 3.6: Probability density functions (*pdf*s) of the total increased lifetime cancer risk obtained at different control planes with normalized distance ζ=3.5, 25 and 60.

The flux-weighted injection mode favors the production of degradation products at larger travel distances. Consequently, knowing that the total risk behavior is mostly controlled by the most toxic species DCE and VC, a flux-weighted injection leads to positively skewed distributions of risk with a peak centered toward smaller risk values (Figure 3.6a).

The total risk-*pdf*s also displays the probability of having negligible risk. This effect depends on the production and the consumption time of the species involved and the travel time needed to reach a certain distance. Thus, negligible risk is highly probable at short traveled distances (Figures 3.6a) due to the late production of the most toxic species, VC. Heterogeneity affects the probability of negligible risk. The formation of preferential channels favored by large σ_Y^2 and flux-weighted injections increases the probability of negligible risk by promoting the rapid migration of products to far away distances.

Describing the risk-*pdf*s by their closest probability density function model provides useful information for a future characterization of risk in real applications. To study this, the sample total risk-*pdf*s (Figure 3.6) were fitted to different theoretical distribution functions honoring the mean and the variance of the ensemble. The Kolmogorov-Smirnov (K-S) test at a 95% confidence level indicates that the risk-*pdf*s obtained in high-risk areas (hot spots) (Figure 3.6b) do not significantly deviate from a Gaussian distribution. In other areas, the K-S tests were only satisfied for the lognormal and beta distribution. This seems to be in agreement with results typically reported in the literature for the concentration *pdf*s [e.g., Bellin et al., 1994; Rubin et al., 1994; Bellin and Tonina, 2007; Sanchez-Vila et al., 2008; Dentz, 2014; de Barros and Fiori, 2014]. The Root-Mean-Square-Deviations (RMSD) of the best fit between the theoretical distributions (truncated normal, lognormal, and beta) and the sample total risk-*pdf*s are also shown in Figure 3.7. The Gaussian-like behavior of the risk distribution obtained in hot spots is here confirmed. In regions with limited or advanced degradation products production (at short and large travel distances, i.e., $\zeta \lesssim 20$ and $\zeta \gtrsim 50$), the risk distribution seems to follow a lognormal or beta distribution. The different scenarios show consistent results (Figure 3.7a, 3.7b and 3.7c).

The impact that the uncertainty in toxicological parameters has on total risk predictions was also investigated. To consider this, a random perturbation of the previously used cancer potency factors was introduced into equation (3.1). The perturbed cancer potency factors were described by pseudo random numbers taken from a uniform distribution supported on a bounded interval defined by $\mu(1 \pm 25\%)$, $\mu(1 \pm 50\%)$ and $\mu(1 \pm 75\%)$, where μ denotes the previously defined CPFs. Figure 3.8 shows the results obtained for σ_Y^2=1. When the mass of the chemical products controlling the total risk is small, i.e., nearby the source zone (ζ=3.5), the uncertainty in physiological parameters do not

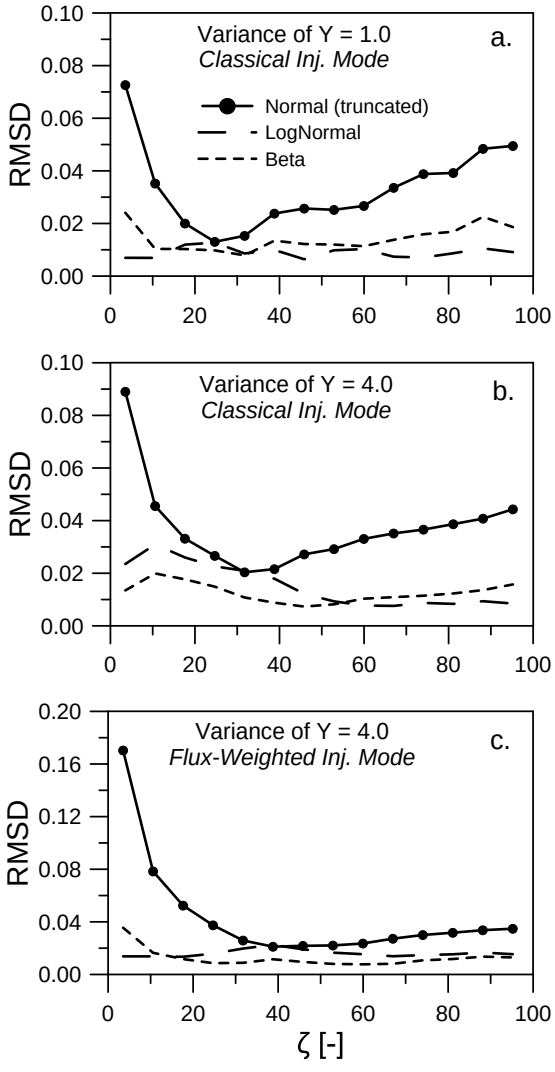

FIGURE 3.7: Root mean square deviation between theoretical Beta, Lognormal and (truncated) Normal distributions and the total increased lifetime cancer risk obtained from Monte Carlo simulations as a function of the normalized travel distance.

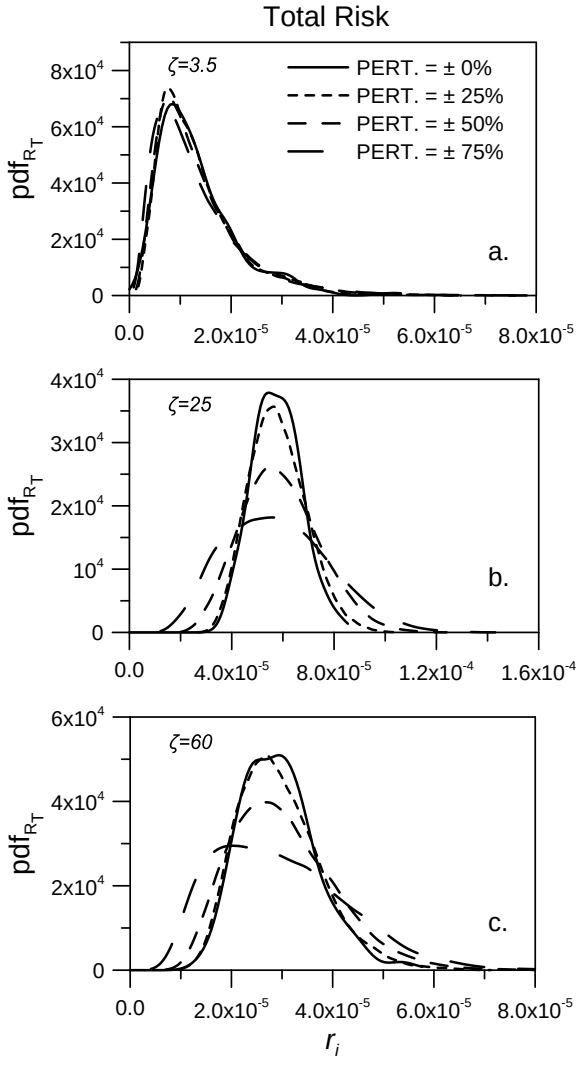

FIGURE 3.8: Probability density functions (*pdf*s) of the total increased lifetime cancer risk considering different degrees of perturbations around the mean of the species-specific cancer potency factors for σ_Y^2=1.0 and normalized distances ζ=3.5, 25 and 60.

substantially affect the risk-*pdf*s predictions (Figure 3.8a). In this case, the uncertainty in the hydraulic conductivity is the controlling factor. However, in areas where the mass of the products DCE and VC is abundant (ζ=25.0 and 60.0), a perturbation of the CPFs will gradually deteriorate the Gaussian-like behavior observed in the risk-*pdf*s (Figure 3.8b and 3.8c). This result agrees with the conclusions of de Barros and Rubin [2008].

3.5 The Toxicology-Based Damkhöhler number

Results have demonstrated that, when the toxicity of intermediate products is larger than that of the parent species, the mean total risk can reach a maximum value (R_c) at a critical position (x_c). At this critical position, the rate of risk generation due to the formation of toxic intermediate products is equal to the rate of risk reduction due to self-purification (natural attenuation). Based on this, it is useful to define a dimensionless number D_R to relate the distance of a sensitive location ($d = x - x_{inj}$) to the corresponding critical distance ($d_c = x_c - x_{inj}$),

$$D_R = \frac{d}{d_c}. \tag{3.14}$$

The sensitive location will be situated downgradient or upgradient from the critical position depending on D_R, i.e., $D_R > 1$ will indicate that the sensitive location is downgradient and vice versa. Knowing this dimensionless number, the relative distance between the sensitive location and the critical position can be estimated by

$$\ell = \left| \frac{d - d_c}{d_c} \right| = |D_R - 1|. \tag{3.15}$$

The estimation of D_R in the field requires several considerations. The distance to the sensitive location d is known by construction but the location of the hot spot (d_c) is largely uncertain. Let us express this critical distance as $d_c = v_a \bar{t}_c$, where $\bar{t}_c$ is the mean arrival time needed for a non-reactive solute to reach the critical distance, and v_a is the apparent velocity of groundwater. An approximate solution of $\bar{t}_c$ can be determined analytically by noticing that the total mass of a given species is closely related to the maximum running

averaged flux-concentration. The derivation is provided in the Appendix D. Because $\bar{t}_c$, which is referred to as the critical time, can be analytically determined from toxicological and chemical properties, D_R can be seen as a toxicology-based Damköhler number. However, v_a depends mostly on the spatial variability of the hydraulic conductivity field and is susceptible to large uncertainties. This uncertainty will propagate to D_R. The following section analyzes how this uncertainty can affect the total risk predictions.

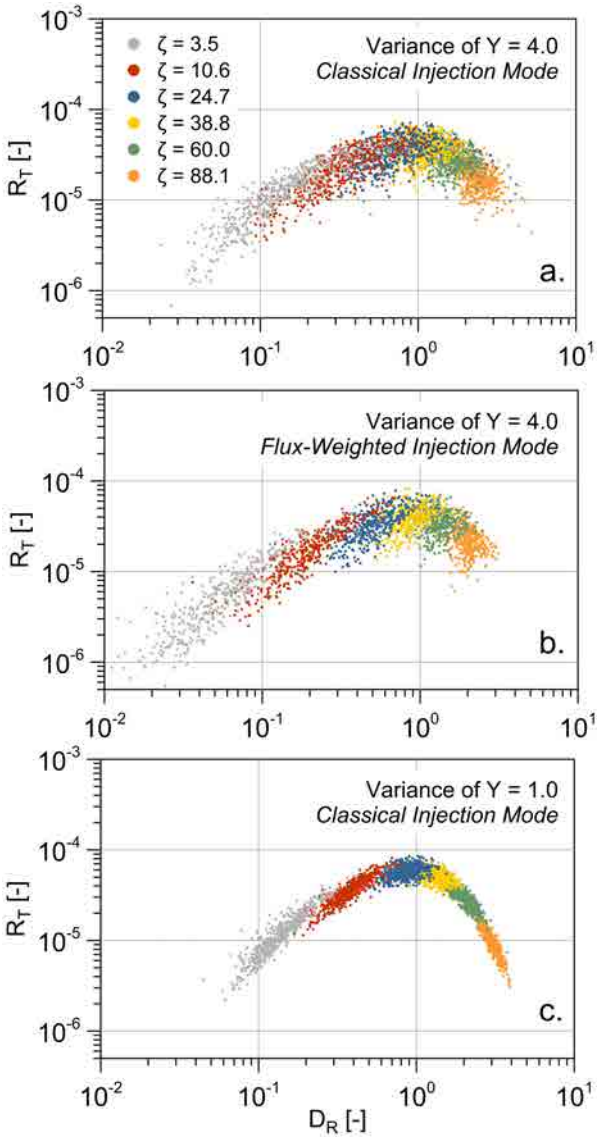

FIGURE 3.9: Relationship between the total increased lifetime cancer risk and the toxicological-based Damköhler number obtained for each simulation and scenario at selected control planes.

To illustrate the importance of the toxicology-based dimensionless number, we estimated D_R from (3.14) for each realization and x-control plane. The critical time $\bar{t}_c$ was estimated from the analytical solution provided in the Appendix D, i.e., from equation (D.15). For each realization, we also simulated the transport of a non-reactive species with an instantaneous injection. The resulting breakthrough curve is denoted as c^δ. From this, v_a at a given x-control plane was calculated as $v_a = d/\bar{t}(x)$, where $\bar{t}(x)$ is the mean arrival time determined from

$$\bar{t}(x) = \frac{\int_0^\infty t c^\delta(t;x)dt}{\int_0^\infty c^\delta(t;x)dt}. \tag{3.16}$$

Figure 3.9 shows the ensemble of the total risk $\mathrm{R_T}$ as a function of D_R. Here, colors are used to distinguish data from different selected control planes. Results show that the maximum total risk satisfies that $D_R = 1$ in all cases. Interestingly, the total risk is positively correlated with D_R when $D_R < 1$ and negatively correlated when $D_R > 1$. That is to say that between the contamination area and the critical distance the total risk increases with ℓ, whereas beyond the critical distance the total risk decreases with ℓ. Essentially, the first regime is controlled by the production of highly toxic intermediate species and the second regime is controlled by the self-purification capacity of the aquifer due to natural attenuation.

The relationship between total risk and the toxicology-based Damköhler number as a function of σ_Y^2 and injection mode is better seen by presenting the ensemble average of the two quantities over all realizations at each control plane (Figure 3.10). In this context, the degree of heterogeneity σ_Y^2 seems to dictate the intensity of $\mathrm{R_T}$ for a given D_R. The intensity decreases with increasing σ_Y^2, suggesting a tendency to dilute the hazard. The effect of the injection mode is seen moderate in this case.

3.6 Impact of Connectivity

Low-order moments of a random field (mean, variance and covariance function) do not provide sufficient information on the structure of preferential channels, which mainly control v_a in a given realization. In other words, two realizations with the same low-order

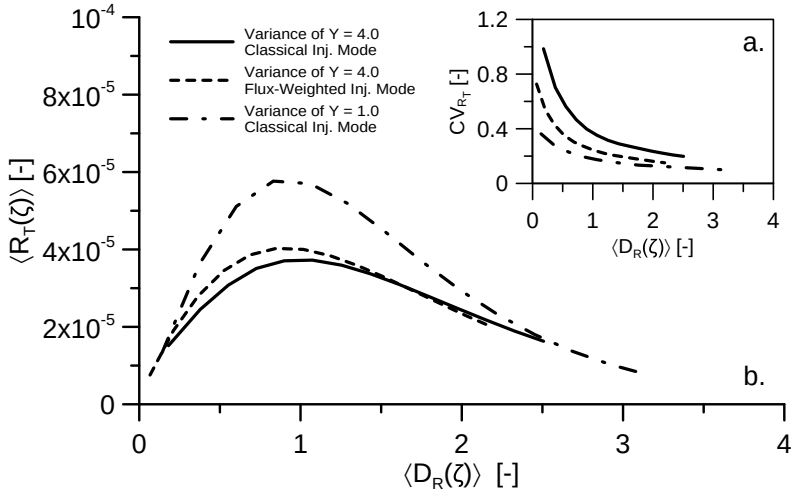

FIGURE 3.10: Coefficient of variation (Figure a.) and mean (Figure b.) of the total increased lifetime cancer risk as a function of the mean toxicological-based Damköhler number obtained at each control plane for all scenarios.

moments can reflect substantially different connectivity features and, in turn, apparent velocity estimates [Gomez-Hernandez and Wen, 1998].

Different metrics have been used to describe connectivity [Sanchez-Vila et al., 1999; Fernàndez-Garcia et al., 2002; Knudby and Carrera, 2005, 2006; Trinchero et al., 2008; Fernàndez-Garcia et al., 2010]. In general, Renard and Allard [2013] distinguished two types of measures: *Static* connectivity metrics only depend on the spatial distribution of aquifer properties, and *dynamic* connectivity metrics depend on the flow and/or transport response to a given impulse. To analyze the effect of connectivity on risk, this section categorizes risk simulations in terms of a dynamic connectivity metric. The chosen connectivity metric CI is defined as the ratio of the effective hydraulic conductivity, K_{eff}, to the geometric mean of K, K_G [Knudby and Carrera, 2005],

$$CI = \frac{K_{eff}}{K_G} \approx \frac{1}{t_{50}} \frac{(x_{cp} - x_{inj})\,\phi}{K_G\, J}, \tag{3.17}$$

where t_{50} is the arrival time of the 50% of mass. High CI values indicate the presence of preferential channels and vice versa. This connectivity metric was estimated for all realization to represent CI as a function of the total risk (Figures 3.11d-f). For comparison

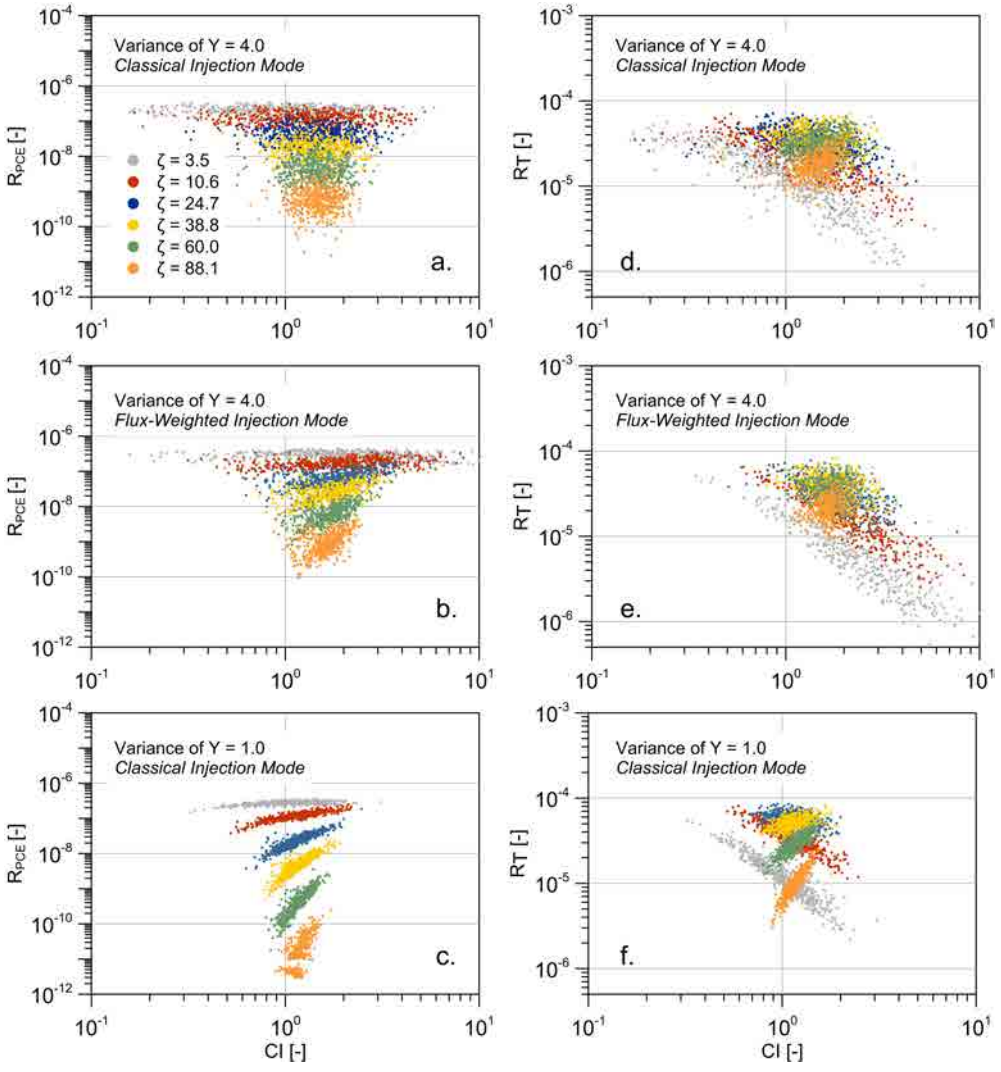

FIGURE 3.11: Relationship between the increased lifetime cancer risk related to the exposure to PCE (left figures, frames a-c) and to the chemical mixture (right figures, frames d-f), and the connectivity indicator obtained for each simulation and scenario at selected control planes.

purposes, we also estimated the relationship between CI and the individual risk posed by PCE (Figures 3.11a-c).

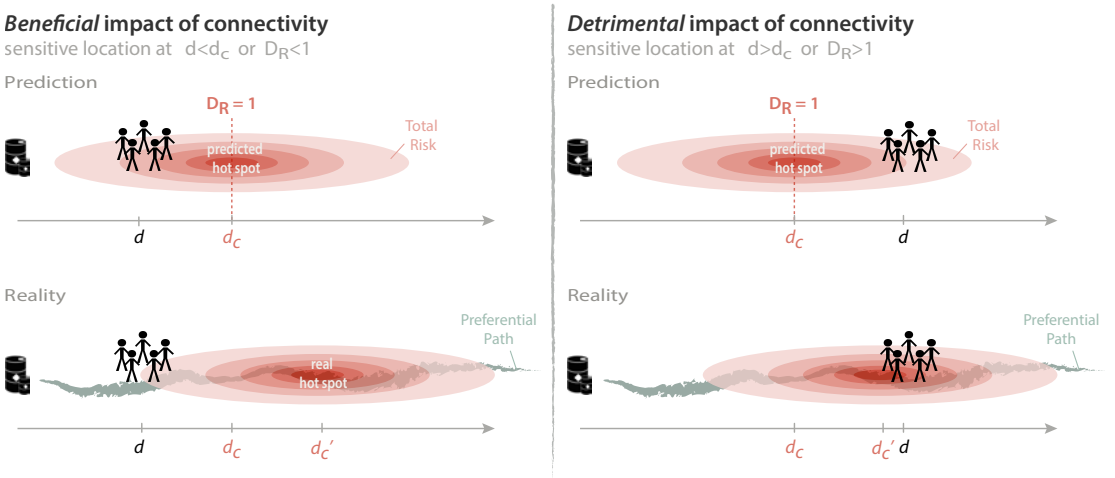

FIGURE 3.12: Schematic illustration of the relationship between the toxicological-based Damköhler number (D_R), connectivity (CI) and the total risk (R_T). The red plume represents the spatial distribution of the total risk reaching a maximum at the critical distance d_c. The toxicological-based Damköhler number D_R is equal to 1 at the critical distance. Left figures represent an scenario A in which the exposed population is initially estimated to be located between the source of pollution and the hot spot (D_R<1). Right figures represent an scenario B in which the exposed population is initially estimated to be located beyond the hot spot location (D_R>1). If initial predictions on the critical distance have not considered (or missed) the presence of an existing preferential transport pathway, the real critical distance d_c' will be located at a farther away distance. This will cause a decrease of the total risk in scenario A (beneficial impact of connectivity) but not in scenario B where the total risk increases (detrimental impact of connectivity).

A clear power law relationship is observed for small σ_Y^2 (Figure 3.11c and 3.11f). Yet, this relationship is strikingly different for PCE than for chemical mixtures. Even though the individual risk posed by PCE always tends to increase with connectivity, mostly due to a decrease in the travel time and degradation, this is not necessarily true for chemical mixtures. When $D_R < 1$ the total risk decreases with increasing connectivity but the opposite occurs when $D_R > 1$. This indicates that the impact of connectivity on risk predictions mostly depends on D_R. When $D_R < 1$, the hot spot is located beyond the sensitive location (d<d_c). In this situation, the presence of preferential channels (high CI values) will move the hot spot to a farther distance, thereby reducing the total risk. Instead, when $D_R > 1$, the hot spot is located between the source zone and the sensitive location (d>d_c). In this case, preferential channels will move the hot spot closer to the

sensitive location, thereby increasing the total risk. Figure 3.12 shows a sketch of these situations.

To further explore this, the power law relationship was fitted to the following regression model

$$\mathrm{R_T} = a\ (CI)^b\,, \tag{3.18}$$

where $|b|$ expresses the sensitivity of the total risk to connectivity, and the sign of b indicates whether connectivity is beneficial ($b < 0$) or detrimental ($b > 0$) in risk predictions. Results show a strong linear relationship between b and D_R (Figure 3.13a.) with a negative correlation when $D_R < 1$ and a positive correlation when $D_R > 1$. Suppose that one estimates, based on the general properties of an aquifer, that a sensitive location (e.g., a populated area) is characterized by $D_R < 1$. In this case, the unnoticed presence of preferential channels at the field site due to the lack of detail characterization will lead to smaller risk predictions than expected. A situation that is conservative in terms of risk. On the contrary, if the sensitive location is characterized by $D_R > 1$, the unnoticed presence of preferential channels can lead to significantly erroneous risk predictions. In this case, one needs to intensify site characterization and monitoring efforts. It is also important to highlight here that the effect of connectivity is expected to be more pronounced in non-multiGaussian fields, where well-connected structures with large permeability values can develop faster solute pathways [Gomez-Hernandez and Wen, 1998].

Despite this clear trend, the correlation between CI and D_R diminishes close to hot spots ($D_R = 1$) and large σ^2_Y values (Figure 3.13c). This is seen for both injection modes without substantially affecting the results. In sum, the unnoticed presence of preferential channels can lead to catastrophic consequences in cases where D_R is large ($d{>}d_c$) and σ^2_Y is relatively small. Finally, we note that other sources of uncertainty can also affect this relationship. For instance, the uncertainty in toxicity measures (see section 3.4.2.2) seems to deteriorate the fit to the regression model without significantly affecting the parameters (Figure 3.14).

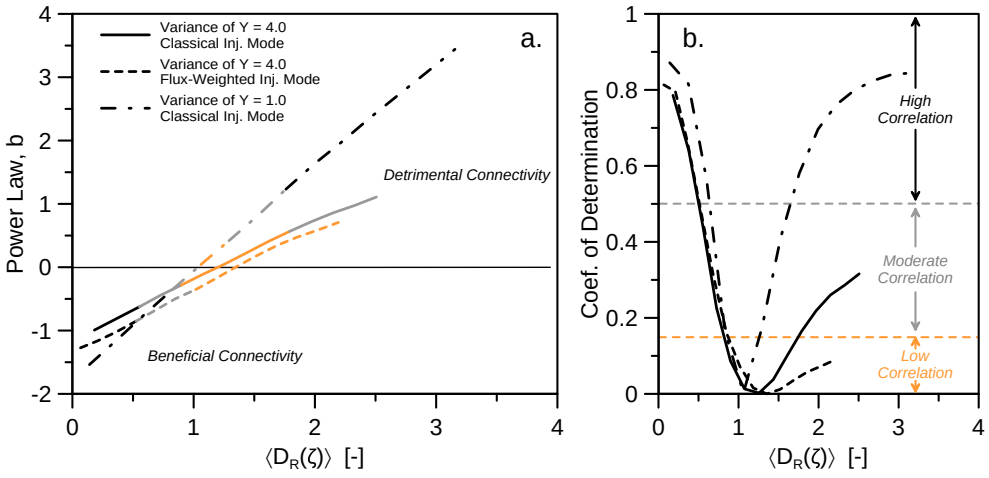

FIGURE 3.13: Power regression coefficient β as a function of the mean toxicological-based Damköhler number obtained at each control plane (Figure a.). The line color indicates the degree of correlation between R_T and CI with the following criterion based on the coefficient of determination r^2: black for a high correlation (r^2 >0.5), grey for a moderate correlation (r^2 <0.5) and orange for a low correlation (r^2 <0.15). The coefficient of determination r^2 related to each power regression and color criterion is given in Figure b.

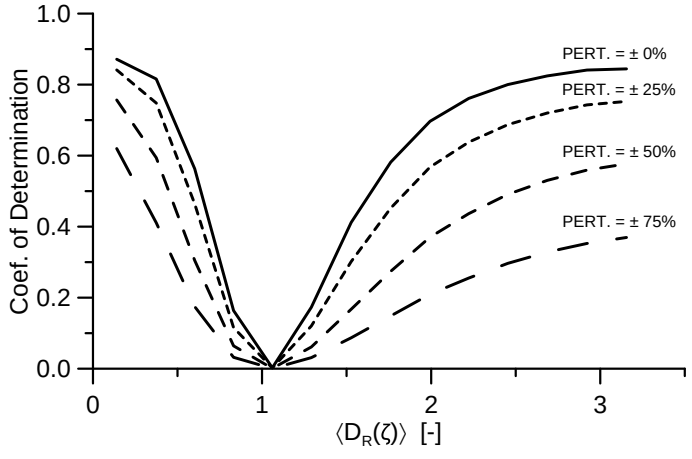

FIGURE 3.14: Coefficient of determination r^2 of the regression model $R_T = a(CI)^b$ as a function of the mean toxicological-based Damköhler number for different perturbations of the cancer potency factor.

3.7 Concluding Remarks

We have investigated human health risk of a chemical mixture, formed by the combination of tetrachloroethylene with its daughter products, in a three-dimensional heterogeneous aquifer under uncertainty through a set of Monte Carlo reactive transport simulations involving a multispecies chemical system. Simulation results have provided a full statistical description of the most common risk metrics (increased life time cancer risk and probability of exceedance of MCLs) as well as an examination of the key factors controlling the formation of hot spots (high-risk areas). The following main findings are highlighted:

- **Uncertainty and reliability.** The statistical analysis of the increased lifetime cancer risk has demonstrated that low risk values, observed far from the source zone for the parent species and near the source for the degradation products, have typically large uncertainties. Contrarily, high-risk areas are the most reliable. This is in line with previous works that found low reliability at low expected concentrations [Kapoor and Gelhar, 1994]. We have also proposed a visualization tool aimed at analyzing the probability of exceedance of MCLs during the temporal and spatial risk management of a contaminated site. Interestingly, results have determined that the area of non-zero probability of MCLs increases with σ_Y^2, owing to the formation of preferential channels and fast travel times, but they take place during a shorter period of time due to an increase dilution of the contaminant in the system. Moreover, a flux-weighted injection mode has led to a decrease in reliability in both space and time by limiting the dilution process while increasing travel times.

- **Probability Distributions Forms.** Total risk *pdf*s have shown positively-skewed asymmetric distributions with a maximum at a relatively low risk value near the source zone. This is especially true for small σ_Y^2 or when a non trivial flux-weighted injection mode is considered. The emergence of asymmetric distributions may lead to reinterpret the *a priori* expected risk value and reliability, which is respectively overestimated and underestimated. The functional form of the risk-*pdf* is determined to follow a Gaussian-like behavior nearby areas of elevated risk. However,

in other areas, the distribution is better characterized by a lognormal or a beta distribution.

- **Formation of hot spots.** Risk analysis of chemical mixtures cannot consider that corresponding hot spots (here defined as areas of elevated risk) are somehow located close to the contaminant source where concentrations are higher. In a chemical mixture, the joint effect of advection, degradation pathways and toxicity dictates the formation of a hot spot. A newly proposed toxicity-weighted Damköhler number D_R has been shown to control the longitudinal distribution of the total risk, which tends to increase with D_R to a maximum at a certain critical position x_c where D_R=1. The time needed for a conservative species to reach this critical distance ($\bar{t}_c$) depends on toxicity and biochemical properties. Approximate analytical solutions of this critical time are provided. These results differ from observation made on more trivial cases, where early arrivals are often seen as the most dangerous cases. On the other hand, the amplitude of the mean total risk is mainly a function of σ^2_Y.

- **The Role of Connectivity.** The assessment of human health risk based only on low-order statistical moments is shown to provide an incomplete analysis of risk. An additional key factor is shown to be connectivity. Results have illustrated that a hydraulic conductivity field with high connectivity is susceptible to have a beneficial (D_R<1 or x<x_c) or a detrimental (D_R>1 or x>x_c) effect on risk depending on the proposed toxicity-weighted Damköhler number. If a sensitive area is characterized by D_R<1, the unnoticed presence of a preferential channel due to the lack of detail characterization is shown to lead to smaller risk estimates than expected. A situation that is conservative in terms of risk (overestimation). On the contrary, if the sensitive area is characterized by D_R>1, the unnoticed presence of a preferential channel can have important consequences as it is shown to lead to higher than expected risk estimates. In this case, one needs to intensify site characterization and monitoring efforts.

CHAPTER 4

Impact of DNAPLs Source-Zone Behavior on the Human Health Risk Propagation in Heterogeneous Aquifers: a Probabilistic Assessment

Contents

Henri, C. V., D. Fernàndez-Garcia and F.P.J. de Barros, submitted in Advances in Water Resources.

4.1 Introduction

Contaminant source zones are often complex and subject to uncertainty. The uncertainty arises from our lack of knowledge of the solute distribution in the contaminated area and of the volumetric discharge crossing the source zone [e.g. Jarsj et al., 2005; Troldborg et al., 2010; Koch and Nowak, 2015]. It is well known that source zone architecture and the hydraulic conditions in its vicinity have a significant impact on the down-gradient solute transport [Brusseau, 2013]. Understanding the release conditions of a contaminant into the subsurface and how it affects the potential exposure of humans to noxious chemicals is essential for an accurate polluted groundwater management.

In this paper, we focus on the effects of Dense Non-Aqueous Phase Liquids (DNAPLs) source characterization on transport and related human health risk propagation into heterogeneous porous media. Subsurface contamination by Dense Non-Aqueous Phase Liquids (DNAPLs) constitutes a major environmental issue given its frequency and the spatiotemporal complexity of its transfer into the groundwater [Cohen and Mercer, 1993]. DNAPLs are quasi-immiscible fluids with a density exceeding that of water. These specific properties are often synonymous with a slow release of mass into the aquifer due mainly to a slow dissolution process. The rate of mass transferred from a source zone into the solute plume is controlled by a complex set of parameters, such as the specific chemico-physical characteristics of the DNAPL, the heterogeneity in the local water flux and the DNAPL spatial distribution and saturation [Pankow and Cherry, 1996; Brusseau, 2013].

The spatio-temporal behavior of DNAPL mass discharge has been documented and different approaches has been adopted to link source zone architecture metrics to mass discharge behavior [e.g. Fure et al., 2006; Page et al., 2007]. Because of the multiprocess nature of DNAPL problems, complex multi-phase numerical methods are commonly used to simulate the dissolution of DNAPL and the intensity of its release into the groundwater [Abriola and Pinder, 1985; Kueper et al., 1989]. However, their application has been limited to purely theoretical purposes because of their computational cost associated with complex non-linear equations and the need for a fine characterization of the source zone spatial variability. From a practical point of view, it is helpful to make use of

the low computational cost of integrative and empirical upscaled mass transfer relationship tested in the literature [Rao et al., 2001; Rao and Jawitz, 2003; Parker and Park, 2004; Zhu and Sykes, 2004]. These methods highlight the main characteristics of DNAPL mass discharge by linking the DNAPL source strength to the DNAPL mass remaining in the source zone [Falta et al., 2005]. The simplicity of this approach lies in the conceptualization of the source zone as a control plane from which the temporal evolution of the contaminant fluxes is simulated using integrative parameters in line with the architecture of the DNAPL. Moreover, in accordance with Soga et al. [2004], this screening approach seems to be more suited to evaluating the risk down-gradient when compared with a management strategy based on source zone monitoring.

DNAPLs are in most cases chemically complex industrial compounds that cause proven or suspected deterioration of human metabolisms. The specific risk management related to this type of subsurface contamination demands the evaluation of their consequences on health. The management of contaminated aquifers is often based on maintaining an estimated risk to health below an acceptable or legally mandatory threshold. However, subsurface pollution, because of its multi-parameter nature, is complex to characterize and is markedly affected by several sources of uncertainty. Probabilistic risk assessment methods for groundwater contamination incorporate hydrogeological uncertainty in the threat quantification [e.g. Andričević and Cvetković, 1996; Maxwell and Kastenberg, 1999; de Barros and Rubin, 2008; Cvetković and Molin, 2012]. This constitutes a robust support for risk assessors, i.e. (1) to quantify the aquifer locations and temporal windows where the risk to health is mostly expected to exceed a regulatory threshold [Tartakosky, 2007; Henri et al., 2015]; (2) to optimize the location of necessary monitoring intensification [James and Gorelick, 1994; Maxwell and Kastenberg, 1999; Fernàndez-Garcia et al., 2012]; and (3) to optimize the allocation of resources for uncertainty reduction [de Barros et al., 2009]. First applied to simple conceptualization of groundwater contamination (e.g. conservative tracer), there is now a tendency for probabilistic risk assessment to deal with more complicated scenarios. For instance, the impact of chemical reactions on the risk to health has recently been assessed [Benekos et al., 2006; Siirila and Maxwell, 2012; Atchley et al., 2013; Henri et al., 2015]. However, the influence of source zone behaviors on health risk propagation remains to be investigated in depth. de Barros and Nowak [2010] and Troldborg et al. [2010] have established a strong correlation between the mode of the source zone release condition and the uncertainty of plume predictions.

There is therefore a need to allocate research efforts to improve our understanding of the significance of source zone release conditions on the risk to human health.

Our work seeks to characterize the impact of DNAPL mass release on the spatiotemporal evolution of the threat to health expressed in terms of the most frequently used risk metrics. To this end, a consequent computational effort was produced to simulate the transfer, transport and fate of a DNAPL into a finely discretized three-dimensional aquifer. Furthermore, we utilized a stochastic framework to incorporate the effects of uncertainty in the hydraulic properties of the aquifer. The two following sections (sections 2 and 3) detail, respectively, the problem and the methods adopted to solve it. Section 4 analyzes the impact of the DNAPL mass release on the human health risk through the spatial characterization of its lower-order statistics and probability density functions. To conclude, we show that the water flux crossing the source zone exerts a strong influence on the effective health risk due to a mixture of interdependent reactive chemicals.

4.2 Problem Statement

The study focuses on a subsurface contamination by the chlorinated solvent Perchloroethylene (PCE), a well-known DNAPL that is responsible for considerable groundwater contamination in industrialized societies [Fay and Mumtaz, 1996; McGuire et al., 2004]. The chlorinated solvent is originally trapped and transferred under a solute form into the aquifer from a source zone. Interestingly, the solute form of PCE initiates a successive dechlorination under the anaerobic conditions assumed in our synthetic aquifer [Jain and Criddle, 1995; McCarty, 1997]. This will lead to the formation of the degradation product Trichloroethylene (TCE), which will be transformed into Dichloroethylene (DCE), which will be successively reduced into Vinyl Chloride (VC), which will finally lose the remaining chloride atom to become the non-toxic Ethene. The decontamination of the site is then achieved when the reductive dechlorination chain is completed. However, the parent species PCE and its three sub-products TCE, DCE and VC present a potential risk to human health that needs to be monitored [Environmantal Protection Agency (EPA), 1997]. PCE, TCE and DCE are indeed suspected of being carcinogenic and VC is a confirmed carcinogenic agent. When dechlorination is initiated, the parent and daughter

species form a chemical mixture composed of chemicals with different toxicities [Environmantal Protection Agency (EPA), 2000].

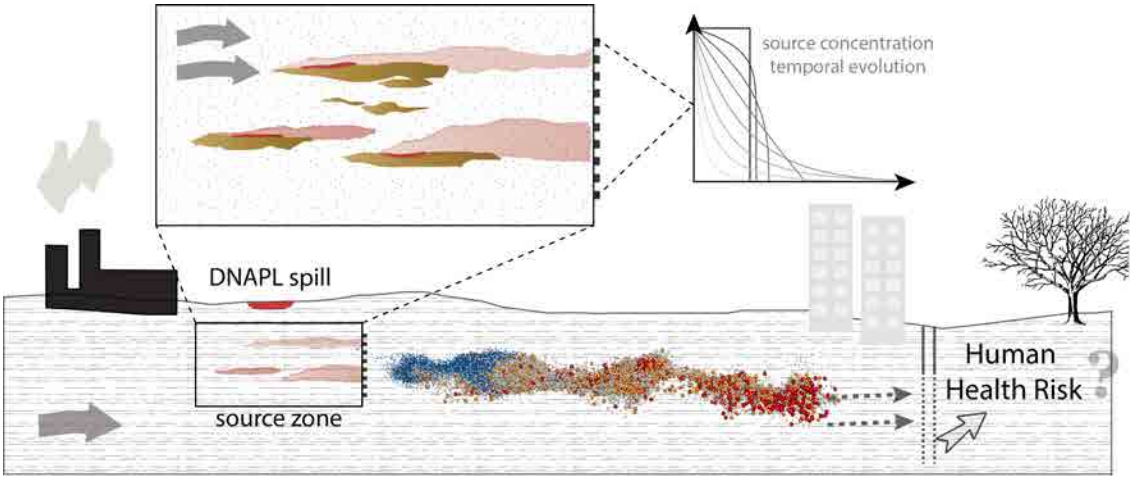

FIGURE 4.1: Scheme of an aquifer contamination by a DNAPL. The source zone is formed of pools due to the presence of low permeability lenses in the source zones. The scheme illustrates the screening approach used in this paper, i.e. the consideration of the concentrations leaving the downstream edge of the source zone area to assess the health risk posed by the contamination.

The risk management of the contaminated aquifer must therefore consider the spatiotemporal behavior of the four compounds that can be simulated under the form of the sequential reaction PCE $\rightarrow$ TCE $\rightarrow$ DCE $\rightarrow$ VC $\rightarrow$ Ethene. The potential risk to human health due to this chemical mixture (effective risk) was characterized statistically and accounts numerically for uncertainties in the hydraulic conductivity fields through a Monte Carlo scheme. This probabilistic approach of human health risk estimation was adopted for different modes of DNAPL mass release.

4.2.1 Flow and Reactive-Transport Model

In this paper, we modeled flow and reactive transport numerically. We considered a three-dimensional (3D) confined aquifer conceptualized by a rectangular prism with length L_x = 1600 m, width L_y = 800 m, and height L_z = 400 m. The flow in the synthetic aquifer was constrained by a constant head at the longitudinal ends, and no-flow at the top and bottom of the domain. We considered an aquifer with steady state flow conditions driven

by a mean horizontal hydraulic gradient of 0.07. The spatially variable 3D flow field was solved by applying Darcy's law:

$$\mathbf{q}(\mathbf{x}) = -K(\mathbf{x})\nabla h(\mathbf{x}), \tag{4.1}$$

where $\mathbf{q}$ [m d^{-1}] is the specific discharge, h [m] is the hydraulic head and K [m d^{-1}] is the hydraulic conductivity at the given location $\mathbf{x}$. The spatial variability of K and its dependent 3D field of specific discharge were regarded as uncertain.

The sequential reductive dechlorination of the solvents PCE, TCE, DCE and VC was approximated by a serial first-order decay reaction network [Clement, 2001; Cunningham and Mendoza-Sanchez, 2006]. Earlier research has shown that these systems is able to approximate more complex biodegradation models such as the Michaelis-Menten model when concentrations are lower than the Michaelis-Menten rate. The serial network can be mathematically expressed by the following system of partial differential equations

$$\begin{aligned}
\phi\mathcal{R}_1\frac{\partial C_1}{\partial t} - \nabla\cdot(\phi\mathbf{D}\nabla C_1) + \nabla\cdot(\mathbf{q}C_1) &= -k_1\phi C_1 + s(\mathbf{x},t),\\
\phi\mathcal{R}_i\frac{\partial C_i}{\partial t} - \nabla\cdot(\phi\mathbf{D}\nabla C_i) + \nabla\cdot(\mathbf{q}C_i) &= y_i k_{i-1}\phi C_{i-1} - k_i\phi C_i,\ \forall i = 2,\ldots,4,
\end{aligned} \tag{4.2}$$

where ϕ is the porosity, and $\mathbf{D}$ [m^2 d^{-1}] is the hydrodynamic dispersion tensor. For each species i, $\mathcal{R}_i$ [$-$] is the retardation factor, C_i [g.m^{-3}] is the resident concentration in the liquid phase, k_i [d^{-1}] is the first-order decay rate constant, and y_{ij} [mol.mol^{-1}] is the effective yield coefficient for any reactant or product pair, i.e. the ratio of mass of species i generated to the amount of mass of species j consumed. Sorption reactions were assumed to be in local equilibrium and to follow a linear sorption isotherm. The concentration temporal evolution of the parent species PCE is affected by a degradation term (decay) and by the source term $s(\mathbf{x},t)$ [g.m^{-3}.d^{-1}], reflecting the mass of dissolved contaminant released from the source zone. This source dissolution rate can be derived from c_s, the concentration of the released contaminant (here PCE) as

$$s(\mathbf{x},t) = q_{sz}c_s(t)\delta(x - x_{inj})\Omega(\mathbf{x}\in A_{sz}), \tag{4.3}$$

where $q_{sz} = Q_{sz}/A_{sz}$, when Q_{sz} is the total flow passing through the source zone area A_{sz}. $\Omega(\mathbf{x} \in A_{sz})$ is a binary indicator function that equals one if $\mathbf{x} \in A_{sz}$ and zero otherwise. In case of DNAPL contamination, the key point of a good predictive model is to accurately represent the source dissolution rate $c_s(t)$.

4.2.2 DNAPL Mass Release Models

A simple mass transfer model As mentioned in the introduction, the intrinsic complexity of the spatio-temporal behavior of DNAPLs mass depletion can be conceptualized by diverse methods. We made use of the commonly employed power law empirical model proposed by Rao et al. [2001] or Parker and Park [2004]. This method describes the temporal evolution of the normalized flux-averaged concentrations of the contaminant leaving a control plane located at the edge of the source zone as a power law of the normalized mass of DNAPL remaining in the source zone (see Figure 4.1), or mathematically:

$$\frac{c_s(t)}{c_0} = \left(\frac{m(t)}{m_0}\right)^{\Gamma}, \tag{4.4}$$

where c_0 is the initial flux-averaged concentration of the released contaminant (here PCE), m is the mass of DNAPL remaining in the source zone with initial value m_0. The temporal evolution of the DNAPL discharge in the aquifer is controlled by the empirical power exponent Γ. This integrative exponent reflects the shape of the source discharge response to a changing source mass, which is controlled by the DNAPL architecture, the heterogeneity of the flow field and by the correlation between heterogeneity and DNAPL saturation [Rao and Jawitz, 2003]. Typically, a Γ lower than one is related to a source discharge increasing rapidly for small increases in the source mass. This large initial mass transfer is characteristic of the prominence of pool and lenses in the DNAPL source zone. By contrast, a Γ larger than one demands a large decrease in mass to significantly increase the source concentration, which reflects the prominence of finger or ganglia characterized by a small initial mass transfer coefficient.

For a flow rate passing through the source zone assumed to be constant, the time dependence of the source concentration can be expressed as [Falta et al., 2005]:

$$c_s(t) = \frac{c_0}{m_0^{\Gamma}} \left\{ \frac{-Q_{sz}c_0}{\lambda_s m_0^{\Gamma}} + \left(m_0^{1-\Gamma} + \frac{Q_{sz}c_0}{\lambda_s m_0^{\Gamma}} \right) e^{(\Gamma-1)\lambda_s t} \right\}^{\frac{\Gamma}{1-\Gamma}}, \tag{4.5}$$

where λ_s is the biodegradation rate observed in the source zone.

A two-domain mass transfer model However, field experiments have shown that the conceptualization of the source zone by either pool *or* ganglia can be oversimplified and inaccurate [Anderson et al., 1992; Sale and McWhorter, 2001]. Indeed, in many cases the two kinds of DNAPL architecture may be present in the source zone and may significantly affect the contaminant mass transfer into the solute plume. A more appropriate mixture of low saturation ganglia and high-saturation pools would lead to (1) an intense mass release at short times due to the characteristic high initial mass transfer of pools and (2) to a subsequent mass release of moderate intensity due to the presence of ganglia. As introduced by Christ et al. [2010], this particular behavior can be conceptualized by a two-domain style model. The respective source concentration related to both ganglia and pool in the source zone is expressed as

$$\frac{c_s^{(g)}(t)}{c_0^{(g)}} = \left(\frac{m^{(g)}(t)}{m_0^{(g)}} \right)^{\Gamma_g}, \text{ and } \frac{c_s^{(p)}(t)}{c_0^{(p)}} = \left(\frac{m^{(p)}(t)}{m_0^{(p)}} \right)^{\Gamma_p}, \tag{4.6}$$

where the exponents (g) and (p) of the source flux-averaged concentration (c_s), remaining masses (m), and power law exponent (Γ) refer, respectively, to the ganglia and pools.

The relative mass leaving the source due to pools and ganglia is mainly controlled by the proportion of water flux crossing the two types of DNAPL architecture. The effective source concentration will evolve in time following:

$$c_s(t) = \frac{Q_{sz}^{(g)} c_s^{(g)} + Q_{sz}^{(p)} c_s^{(p)}}{Q_{sz}^{(g)} + Q_{sz}^{(p)}} \tag{4.7}$$

TABLE 4.1: Risk parameters

Parameter	Value			
Ingestion rate, IR [l/d]	1.4			
Body weight, BW [kg]	70.0			
Exposure duration, ED [y]	30.0			
Exposure frequency, EF [d/y]	350.0			
Average time of the expected lifetime, AT [d]	25550.0			
	PCE	TCE	DCE	VC
Cancer potency factor, CPF_i [kg d/mg]	0.0021	0.011	0.6	1.5
Maximum Contaminant Level, MCL_i, [ppb]	5.0	5.0	7.0	2.0

where $Q_{sz}^{(g)}$ and $Q_{sz}^{(p)}$ are the flow passing through the ganglia and pools forming the source zone area (i.e., $Q_{sz} = Q_{sz}^{(g)} + Q_{sz}^{(p)}$). Thus, the source concentration can be expressed as a function of the fraction of pool (f_p) and ganglia (f_g) within the source zone:

$$c_s(t) \approx c_s^{(g)} f_g + c_s^{(p)} f_p \tag{4.8}$$

where $f_p + f_g = 1$.

While conceptualizing the source zone as a mixture of pools and ganglia, it is useful to express the fraction of pool and ganglia in the source zone in terms of their ratio, i.e. $GTP = f_g/f_p = f_g/(1 - f_g)$ [Christ et al., 2005]. The temporal evolution of the source concentration (4.8) is then expressed as a function of a single metric by:

$$c_s(t) \approx \frac{c_s^{(g)} GTP + c_s^{(p)}}{GTP + 1}. \tag{4.9}$$

4.2.3 Human Health Risk Metrics

Stake-holders and regulators often base remediation monitoring and population protection on maintaining the estimated risk below a threshold with respect to the metric used. We analyzed two frequently employed metrics for decision making: (1) the Increased lifetime Cancer Risk (ILCR), and (2) the exceedance of Maximum Contaminant Levels (MCL).

ILCR for an Exposure to a Chemical Mixture This work seeks to quantify the risk of cancer from a long-term exposure to the mixture of chlorinated solvents along the

contaminated aquifer after a DNAPL spill and reactive transport into a heterogeneous porous media. The threat to human health were evaluated from the temporal evolution of the contamination concentrations through integrated breakthrough curves obtained at a series of vertical control planes. The quantification of the human health risk follows the guidance of the Environmantal Protection Agency (EPA) [1989] that describes the carcinogenic health risk as a Poisson model for individual cancer occurrence. Our analysis focuses exclusively on the effective threat posed by exposure to the chemical mixture of chlorinated solvents ($\mathrm{R_T}$) that can be approximated by a simple addition of the individual cancer risk associated with each of these compounds (PCE, TCE, DCE and VC) [Speek, 1981], i.e.

$$\mathrm{R_T}(x) = \sum_{i=1}^{4} \mathrm{R}_i(x). \tag{4.10}$$

where $\mathrm{R}_i(x)$ is the incremental lifetime cancer risk (ILCR) due to the exposure to the chemical i at a given longitudinal position of the control plane x. The individual ILCR is given mathematically by

$$\mathrm{R}_i(x) = 1 - \exp[-ADD_i(x) \times CPF_i]. \tag{4.11}$$

The ILCR considers the toxicity of the contaminant i through the metabolized cancer potency factor CPF_i [kg d/mg], and the exposure by direct ingestion of the contaminant i through the average daily dose ADD_i [mg/(kg d)], given by

$$ADD_i(x) = \bar{c}_i(x) \left[\frac{IR}{BW}\right] \frac{ED \times EF}{AT}, \tag{4.12}$$

where IR is the ingestion rate of water [L/d], BW is the body weight [kg], AT is the expected lifetime [d], ED is the exposure duration [y], and EF is the daily exposure frequency [d/y]. We assume these behavioral and exposure parameters to be constant and define them in Table 4.1. We focused more specifically on $\bar{c}_i$ [mg/L], the critical (flux-averaged) concentration of the pollutant i. This key factor of the average daily dose can be regarded as a critical maximum running averaged concentration of the concentration breakthrough curve obtained at the control plane located in x over the exposure duration ED [Maxwell and Kastenberg, 1999]. Formally, $\bar{c}_i$ is estimated by

$$\bar{c}_i(x) = \max_{t>0} \left\{ \frac{1}{ED} \int_t^{t+ED} c_i(\tau; x) d\tau \right\}. \tag{4.13}$$

In case of uncertain hydraulic properties, $\bar{c}_i$ is described as random. The distribution of which controls the resulting ILCR distribution.

Exceedance of MCLs When the quantification of the risk of cancer occurrence is not mandatory, stake-holders can base the remediation effort on maintaining concentrations below MCLs, i.e. the legal threshold limit of a contaminant concentration permitted in groundwater intended for human consumption. Under uncertain conditions, the monitoring of the threshold satisfaction is described stochastically through the estimation of the probability to exceed the MCLs associated with the chemical species i, i.e.

$$\xi_{c_i}(x,t) = \text{Prob}[c_i(t,x) > \text{MCL}_i]. \tag{4.14}$$

One of the main goals of the risk assessor is to locate areas of elevated risk. These areas will be denoted as *hot spots*. When the ILCR is a temporally integrative metric, ξ_{c_i} preserves the temporality of the problem. In this case, a *hot spot* will indicate the longitudinal interval in which the probability of exceedance reaches a large value at a given time. In addition, we define the temporal windows of persistence of the elevated values as *hot moments*.

The statistical analysis of the two human health risk metrics spatial (for R_T) and spatiotemporal (for ξ_{c_i}) propagation was performed for a set of scenarios in order to study the impact of the degree of heterogeneity in the uncertain hydraulic conductivity field and the impact of the DNAPL source zone discharge behavior.

4.3 Methodology

Stochastic Framework The uncertainty in the hydraulic conductivity was considered through a stochastic framework, with the K-field regarded as a random space function. The stochastic estimation of the human health risk has been evaluated using analytical

TABLE 4.2: Physical parameters

Parameter	Value
Flow problem	
Average hydraulic gradient [−]	0.07
Longitudinal dispersivity, α_L [m]	0.4
Transversal dispersivity in the horizontal plane, α_{TH} [m]	0.04
Transversal dispersivity in the vertical plane, α_{TV} [m]	0.01
Porosity, ϕ [−]	0.3
Heterogeneous field	
Variogram type	Gaussian
Mean of Y (Y=ln$K$) [m^2/d]	0.0
Variance of Y	1.0, 2.0, 4.0, 8.0
Integral scales, λ_x=λ_y=λ_z [m]	14.18
Domain discretization	
Number of cells in x direction, n_x	400
Number of cells in y direction, n_y	220
Number of cells in z direction, n_z	100
Cell dimension, $\Delta_x \times \Delta_y \times \Delta_z$ [$m \times m \times m$]	4.0 × 4.0 × 4.0

methods in order to consider uncertain hydrogeological characteristics [e.g., Andričević and Cvetković, 1996; de Barros and Rubin, 2008]. However, no existing analytical approach is applicable to reactive chemical mixtures in highly heterogeneous 3D aquifers. In the present study, the human health risk was evaluated through numerical Monte Carlo simulations. This enabled us to characterize the ILCR by its statistical moments and probability density functions (*pdf*s), and the determination of the exceedance of MCLs in a probabilistic manner.

Random hydraulic conductivity field The spatial structure of the log-conductivity, $Y(x) = \ln K(x)$, was described by its random space function. The Y-field follows a multi-Gaussian random space function model with an isotropic Gaussian covariance function characterized by a mean of zero and an integral scale λ of 14.18 m. The impact of the degree of heterogeneity was investigated considering four variances of Y: $\sigma_Y^2 = \{1.0, 2.0, 4.0, 8.0\}$. The domain was finely discretized into 8 million cells, ($400 \times 200 \times 100$), each cell being a cube of 64 m^3 ($4.0 \times 4.0 \times 4.0$ m). See Table 4.2.

TABLE 4.3: Biochemical parameters

Parameter	Value			
	PCE	TCE	DCE	VC
First order decay, k_i $[d^{-1}]$	0.0025	0.002	0.0015	0.001
Yield coefficient, $y_{i/j}$ $[mol\, mol^{-1}]$	×	0.79	0.74	0.64
Retardation factor, $\mathcal{R}_i$ $[-]$	7.1	2.9	2.8	1.4

Flow and reactive transport For each of the 500 stochastically pre-generated equiprobable Y-fields, the Monte Carlo scheme consisted of three main steps: (1) solving the flow problem; (2) solving the reactive-transport problem (Eq. 4.2); and (3) estimating the corresponding R_T and spatiotemporal windows of exceedance of the MCLs. The flow equation (Eq. 4.1) was solved by means of the finite difference code MODFLOW [Harbaugh et al., 2000]. The reactive-transport of the four reactive compounds PCE, TCE, DCE and VC was then solved making use of the efficient random-walk particle-tracking code RW3D developed by Fernàndez-Garcia et al. [2005a] and subsequently adapted to first-order decay network simulation by Henri and Fernàndez-Garcia [2014].

The numerical method splits the reactive plumes into a large number of moving particles. Each particle is associated with a species state that evolves in time in accordance with the biochemical conditions. It uses the velocity field previously resolved to advectivally move particles, and disturbs the motion by a random displacement in order to simulate dispersion [Salamon et al., 2006a]. Henri and Fernàndez-Garcia [2014] contains more information on numerical details and model efficiency and accuracy. Transport was controlled by a spatially homogeneous porosity ϕ of 0.3 and a longitudinal, horizontal transverse and vertical transverse dispersivity of 0.4, 0.04 and 0.01, respectively (Table 4.2). Our selected values for the reaction rates (k_i) are within the range of first-order decay rates recorded by the [Environmantal Protection Agency (EPA), 1999]. The retardation factors were chosen according to the differences in mobility between the four chlorinated solvents [Lu et al., 2011] (Table 4.3).

Source zone A large number of PCE particles (10^5) was uniformly and instantaneously released from a rectangular 2D source area A_{sz} of dimension $6.8\lambda \times 3.4\lambda$ (in the y-z plane). This source area is perpendicular to the mean flow. From this pulse injection, the first

Table 4.4: Source zone mass transfer parameters

Parameter	Value
Initial concentration, C_0 $[g.m^{-3}]$	0.1
Initial mass, M_0 $[g]$	3×10^5
Degradation rate, λ_s $[d^{-1}]$	5×10^{-5}
Volumetric discharge Q_{sz} $[m^3.d^{-1}]$	*depends on K-field*
Power law Γ $[-]$	0.25, 0.5, ..., 4.0

arrival time of particles passing through a set of control planes were recorded to estimate cumulative breakthrough curves of the flux-averaged concentrations, $c_i^h(t;x)$.

The flux-averaged concentrations resulting from the release of DNAPL expressed in (Eq. 4.5) were simulated using the principle of superposition that states that

$$c_i(t;x) = \int_0^t c_s(\tau) c_i^\delta(t-\tau;x) d\tau, \tag{4.15}$$

where c_i^δ is the Dirac-input solution of the flux-averaged concentrations for species i. For numerical purposes, the source term can be discretized in step functions to give

$$c_s(t) = c_0 H(t) + \sum_{j=1} \Delta c_{s,j} H(t-t_j),$$

when $\Delta c_{s,j} = c_{s,j} - c_{s,j-1}$ and $H(t)$ is the Heaviside step function. The principle of superposition (Eq. 4.15) can now be written in terms of the estimated cumulative breakthrough curves as

$$c_i(t;x) = c_0 c_i^h(t;x) + \sum_{j=1}^{t_j<t} \Delta c_{s,j} c_i^h(t-t_j;x). \tag{4.16}$$

The initial concentration of PCE in the source zone was fixed at 0.1 g.m^3, for an initial total mass of 300 kg. Moreover, the chlorinated solvent was affected by an in-situ biodegradation fixed at the rate of 5×10^{-5} d^{-1}. Source zone parameters are shown in Table 4.4. The sensitivity analysis concerns the power exponent of the mass transfer model (Eq. 4.4) and the fraction of ganglia and pools in the two-domain mass transfer model (Eq. 4.6). The impact of these two parameters on the source concentration is shown in Figure 4.2.

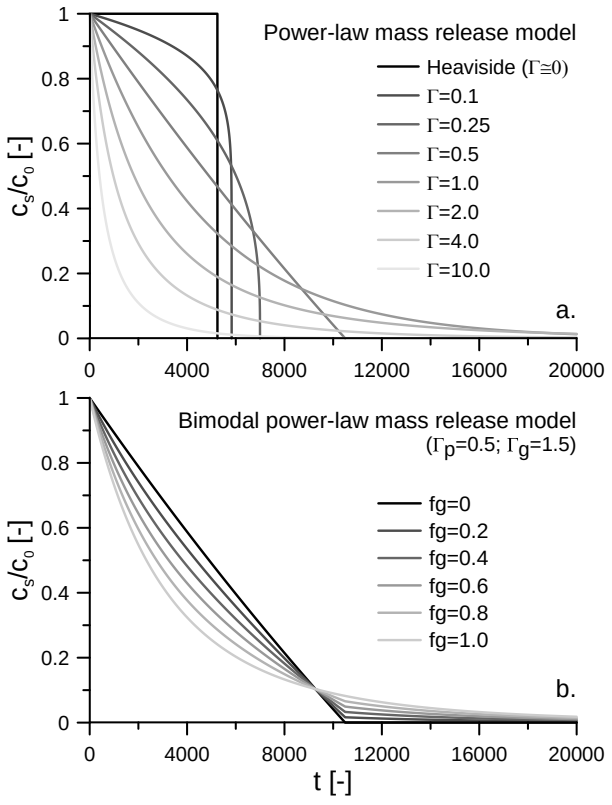

FIGURE 4.2: Temporal evolution of the source zone concentrations for (a) a set of power exponent of the simple mass transfer model; and (b) for a set fraction of ganglia for a bimodal source zone mass transfer model.

4.4 Statistical Assessment of the Impact of the DNAPL Mass Release on the Human Health Risk

Results from the simulations are displayed in this section with regard to the following organization: First, the observed impact of the power exponent of the DNAPL source-zone mass-transfer model (reflecting the DNAPL architecture) is shown both on the probability of exceedence of the MCLs (in section 4.4.1) and on the excepted value and the probability density function of the total ILCR (in section 4.4.2). Secondly, the potential impact of a two-domain style mass release model on the total ILCR is described (in section 4.4.3). Results are presented in terms of dimensionless spatial and temporal variables normalizing

the longitudinal distance from the injection by the integral scale as

$$\zeta = \frac{x - x_{inj}}{\lambda},$$

and normalizing the elapsed time by an approximate time needed to travel an integral scale, i.e.

$$\tau = \frac{t\, K_G\, J}{\lambda \phi},$$

where K_G is the geometric mean of the hydraulic conductivity and J is the hydraulic gradient.

4.4.1 Impact of a power mass transfer on the probabilities to exceed MCLs

The first risk metric that we analyze is the risk of exceedence of the Maximum Concentration Levels, i.e. $\xi_{c_i}(x;t) = \text{Prob}[c_i(t;x) > MCL_i]$. The *hot spots* e.g. spatial ranges in which high values of ξ_{c_i} are predicted and their temporal persistence (*hot moments*) are identified through a useful visualization tool introduced in Henri et al. [2015]. Hot spots and hot moments are shown in Figures 4.3 and 4.4. This visualization tool displays the spatiotemporal propagation of the risk by contour-mapping ξ_{c_i} with the normalized longitudinal distances in the horizontal-axis and the normalized time in vertical-axis.

It should be noted that despite the lower concentrations expected for the last subspecies of the reaction chain, the probability that VC concentrations exceed the MCL is high over considerable distance and time (see Figures 4.3 and 4.4, frames d,h,l) because of the low concentration threshold. Results show that the DNAPL source zone architecture (or power exponent of mass-transfer) exerts a significant influence on the magnitude of the probability of exceedance for any species of the mixture. An increase in the power exponent is translated into a reduction of the global threat where hot spots are less spread and hot moments are less persistent. In other words, an underestimation of the pooling process of the DNAPL (increased Γ exponent) in the source zone leads to an underestimation of the threat posed by the contamination. It is interesting to note that despite a change in the risk amplitude the location of the peak of ξ_{c_i} appears to be retained for all Γ values.

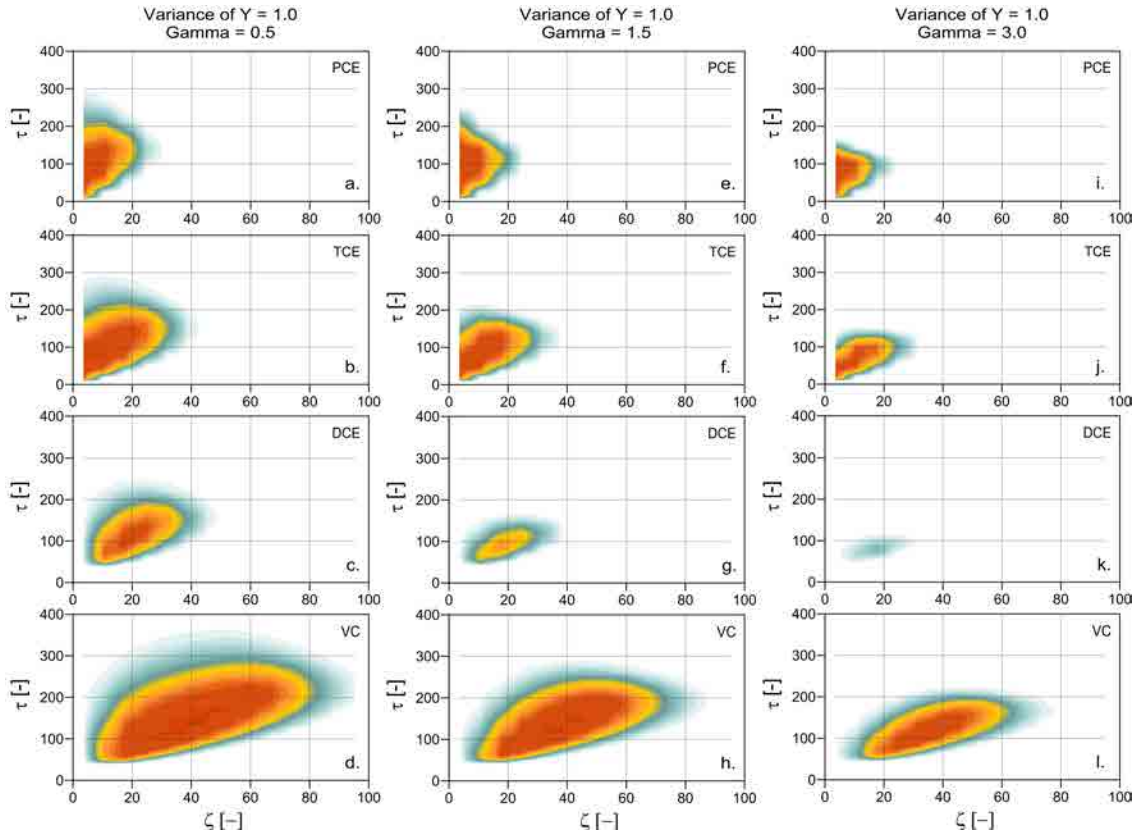

FIGURE 4.3: Risk of exceedance of the MCLs of PCE (first row), TCE (second row), DCE (third row) and VC (fourth row) as a function of the normalized time τ and the normalized distance η for variance of Y of 1.0 and a mass release power coefficient of 0.5 (frames a-d), 1.5 (frames e-h) and 3.0 (i-l).

As expected and as shown in Henri et al. [2015], the degree of heterogeneity in K plays a major role in risk dilution. Comparison of Figures 4.3 and 4.4 illustrates how $\xi_{c_i}(\zeta;\tau)$ varies from a mildly ($\sigma_Y^2 = 1.0$) to a highly heterogeneous ($\sigma_Y^2 = 4.0$) Y-field. It may be observed that the magnitude of ξ_{c_i} decreases when σ_Y increases. However, in this scenario, a non-negligible risk is observed over a large portion of aquifer due to an increased macrodispersion. In other words, *hot spots* are wider and *hot moments* are longer for a low degree of heterogeneity, but this intense and spatiotemporally focused risk becomes rapidly negligible when the plume moves downstream of the *hot spots*.

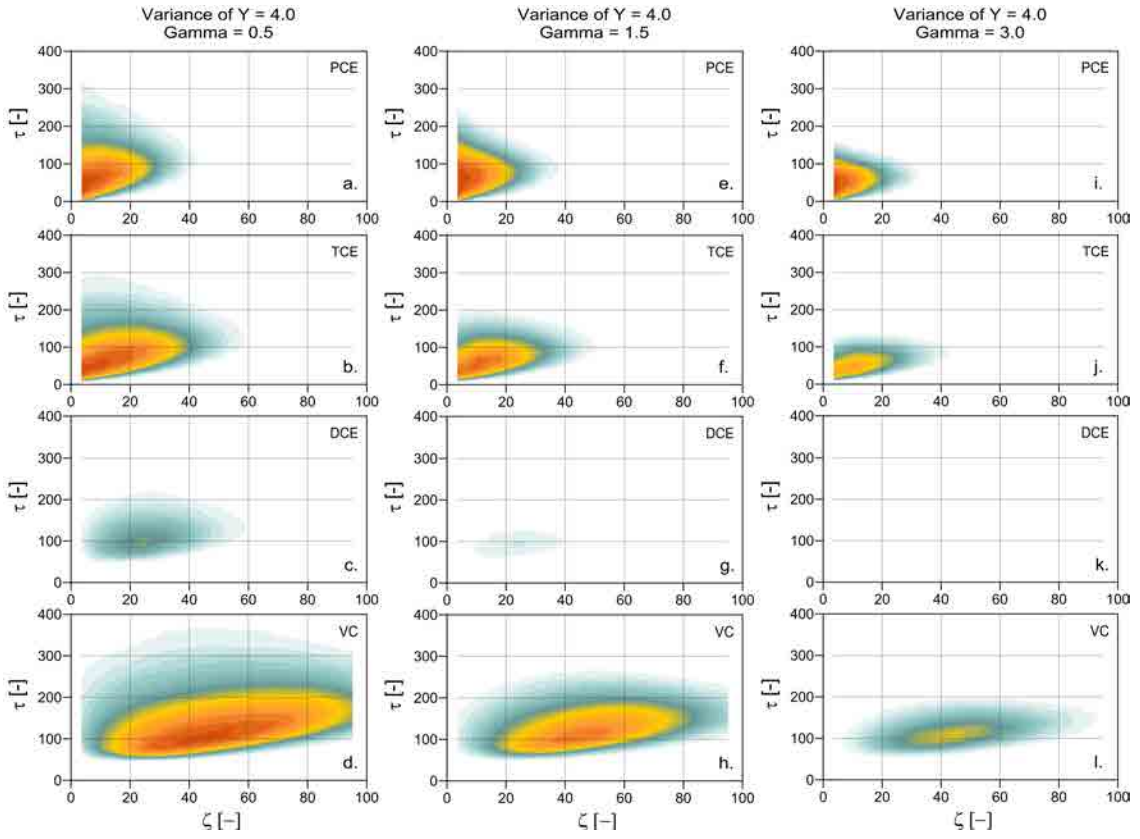

FIGURE 4.4: Risk of exceedance of the MCLs of PCE (first row), TCE (second row), DCE (third row) and VC (fourth row) as a function of the normalized time τ and the normalized distance η for variance of Y of 4.0 and a mass release power coefficient of 0.5 (frames a-d), 1.5 (frames e-h) and 3.0 (i-l).

4.4.2 Impact of a power mass transfer on the total ILCR

Expected total ILCR Let us now focus on the second risk metric: the Increase Life Time Cancer Risk, with effective value R_T. For the record, the ILCR is a temporally integrative risk metric, i.e. only its spatial propagation is analyzed. Figure 4.5 displays the evolution of the expected (i.e., average ensemble of the) total ILCR along the aquifer longitudinal profile as a result of the simulations with σ_Y^2 of 1.0 and 4.0 and using a set of 16 Γ values ranging from 0.25 to 4.0. Moreover, the profile of R_T is shown for a temporal evolution of the DNAPL source zone concentrations following a Heaviside step function, i.e. $c_s(t) = c_0$ until the exhaustion of the initial mass. Note that this Heaviside function

can be regarded as a result of the power mass depletion model with a Γ exponent tending to 0.

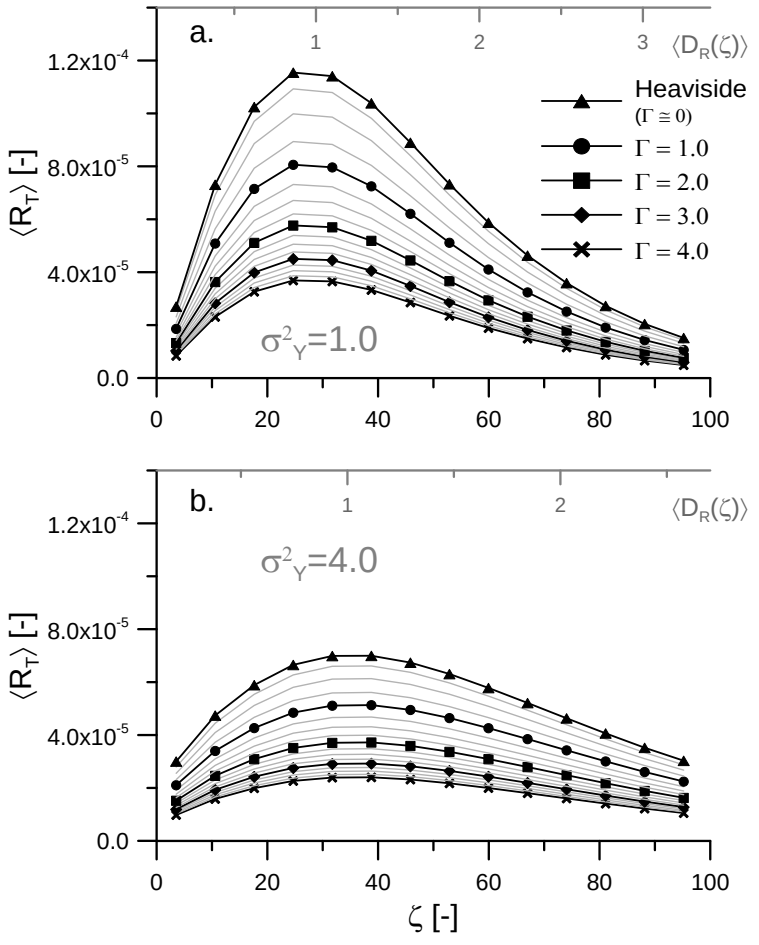

FIGURE 4.5: Impact of the mass release power coefficient on the expected total ILCR from the chlorinated solvents reactive-transport in (a) a mildly and (b) highly heterogeneous hydraulic conductivity field.

The longitudinal profile of the expected R_T displays a two-phase behavior characteristic of a chemical mixture with subproducts presenting a higher toxicity than the parent species. The total ILCR increases first in the subspecies zones of production, reaches a peak when the rate production/destruction is similar, and then decreases when the toxic subspecies are mostly destroyed (see Henri et al. [2015]). Regardless of the degree of heterogeneity in the flow field, the mass release coefficient Γ is shown to control the amplitude of the total risk. Here again, the presence of ganglia (increased Γ) is shown to be beneficial

by decreasing the amplitude of the total risk signal along the aquifer profile. In global terms, increasing the degree of heterogeneity in the hydraulic conductivity field tends to decrease this magnitude of the threat (compare frames a and b of the Figure 4.5).

On the other hand, it is interesting to observe that the exponent Γ does not have an impact on the critical distance x_c, i.e. the distance from the injection where the maximum risk is observed (*hot spot*). As shown in Henri et al. [2015], for a first-order decay network, the peak of expected total ILCR is predictable when a predefined toxicity-based Damköhler ($\mathrm{D_R}$) reaches 1. This useful metric is defined as the ratio between $\bar{t}$, the average time needed for a conservative tracer to reach a sensitive location, and $\bar{t}_c$, a mean arrival time needed for a tracer to attain the critical distance (where the total ILCR is expected to reach a maximum value), i.e.

$$D_{\mathrm{R}} = \frac{\bar{t}}{\bar{t}_c}. \tag{4.17}$$

The critical time $\bar{t}_c$ depends on risk parameters (toxicity, exposure duration and frequency, physiological properties in individuals) and reaction parameters (decay, retardation) and can be evaluated analytically, as

$$\bar{t}_c = \arg\max \left\{ \frac{IR \times ED \times EF}{BW \times AT} \sum_{i=1}^{4} CPF_i \, S_{ij} e^{-k_j \bar{t} \mathcal{R}_i^e(\bar{t})/\mathcal{R}_j} S_{j1}^{-1} \right\}, \tag{4.18}$$

where $\mathcal{R}_i^e$ is a time dependent effective retardation factor related to a species transition PCE $\rightarrow$ species i, and $\mathbf{S}$ is a matrix composed of the eigenvalues of a predefined reaction matrix. Readers are referred to Henri and Fernàndez-Garcia [2014] for more information.

As stated in Henri et al. [2015], critical distance and time can be solved from a Dirac-input source (or pulse injection) as the source term is assumed not to affect the critical distance. This statement is confirmed by the present results. The expected value of the toxicity-based Damköhler corresponding to the control plane located at the x position is shown in the upper axis of Figure 4.5. It may be observed that the peak of the expected total ILCR is reached when $\mathrm{D_R}$ approaches 1, which is independent of the value given to σ_{Y}^2 or to the PCE mass transfer power exponent Γ.

Scaling factor When the ascending and descending phases of the risk signal along the aquifer longitudinal profile are explained (and even well predicted) by the biochemical and toxicological conditions, the changes of amplitude seem to be a more complex phenomenon depending *inter alia* on the mass depletion mode (Γ) and on the degree heterogeneity in the flow field. The dependence of the total ILCR amplitude on the DNAPL mass release mode can be investigated by observing the scaling factor (χ) between $R_T^{(H)}$, the total ILCR value obtained for a mass release following a Heaviside step function ($\Gamma \approx 0$), and $R_T^{(\Gamma)}$, the total ILCR value obtained for a given mass depletion power exponent, i.e.

$$\chi = \frac{{R_T}^{(H)}}{{R_T}^{(\Gamma)}}. \tag{4.19}$$

The Heaviside function is an easily conceptualized model to describe the temporal evolution of the source zone concentration that produces the highest cancer risk values ("worst-case scenario").

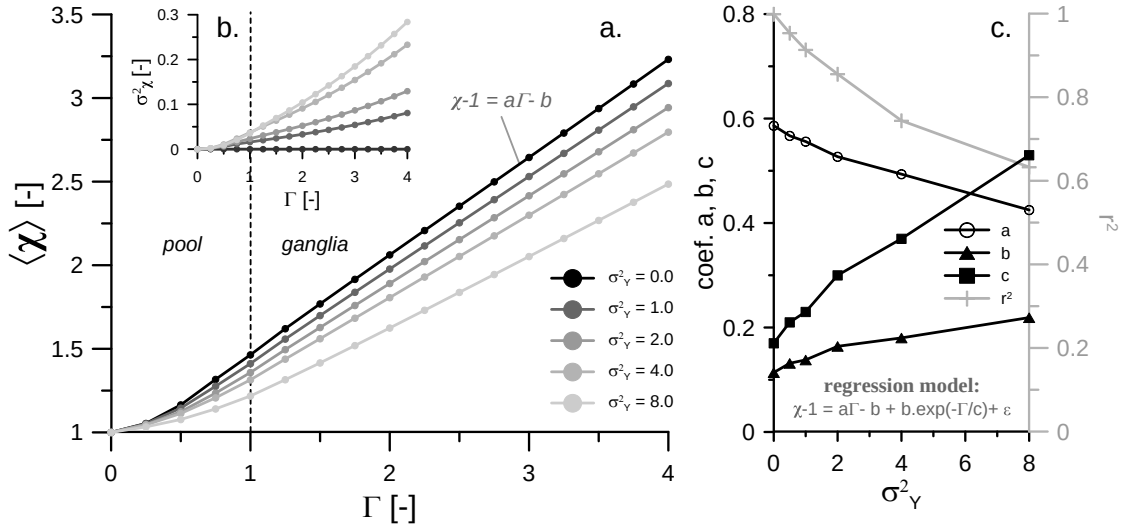

FIGURE 4.6: Expected value (a) and variance (b) of the scaling factor χ as a function of the power exponent of the DNAPL mass transfer model Γ for a variance of the hydraulic conductivity of 0.0 (homogeneous case), 1.0, 2.0, 4.0 and 8.0. q

Interestingly, χ seems to be relatively constant all along the aquifer longitudinal profile. The scaling factor is calculated for each simulation. Figure 4.6 shows its ensemble mean

(frame a) and variance (frame b) as a function of the source discharge for different variances of the Y-field. The more the power exponent of the mass transfer model increases, the more the total ILCR deviates from the risk signal obtained for a step injection mode. On the other hand, the sensitivity of the scaling factor to the source zone mass release decreases with the degree of heterogeneity. These observations can be expressed by the following regression model obtained over all realizations with equal σ_Y^2

$$\chi = a_1\Gamma + a_2(\exp(-\Gamma/a_3) - 1) + \epsilon, \tag{4.20}$$

where a_1, a_2 and a_3 are fitting parameters depending on σ_Y^2. This dependence is illustrated in Figure 4.6c. The same Figure 4.6c shows that the coefficient of determination of the regression r^2 decreases with the degree of heterogeneity, but remains acceptable in all cases (> 0.6). Interestingly, the regression model fits perfectly (i.e., $r^2 = 1$) the ensemble mean behavior, which reflects a symmetrical disturbance ϵ around the mean. Moreover, note that the relationship between χ and Γ follows a simple linear regression model: $\chi = a\Gamma - b + \epsilon$ when $\Gamma > 1$ (ganglia).

Probability density functions of $\mathbf{R_T}$ The total risk is now characterized by its non-parametric *pdf*s for a set of mass depletion exponents and two different degrees of heterogeneity ($\sigma_Y^2 = 1.0$ and 4.0) at three normalized distances from the source zone ($\zeta = 3.5$, 25.0 and 60.0) as shown in Figure 4.7. The positive skewness observed near the source zone (Figure 4.7a,d) is a typical asymmetry of total risk *pdf*s in case of chemical mixtures. This is caused by the high probability of occurrence of arrival times lower than the characteristic time required for the production of the highly toxic subspecies at short distances [Henri et al., 2015].

More importantly, the results depicted in Figure 4.7 demonstrates the substantial impact of the source zone architecture on the risk-*pdf*s shape. The presence of pools in the source zone (low Γ exponents) tends to stretch the *pdf*s, increasing both mean and variance of the risk distribution. This effect seems more pronounced at mid-distance, where total ILCRs are the highest (Figure 4.7b,e). These observations are true for both degrees of heterogeneity in the K-field. The global impact of σ_Y^2 produces an increase in the dilution

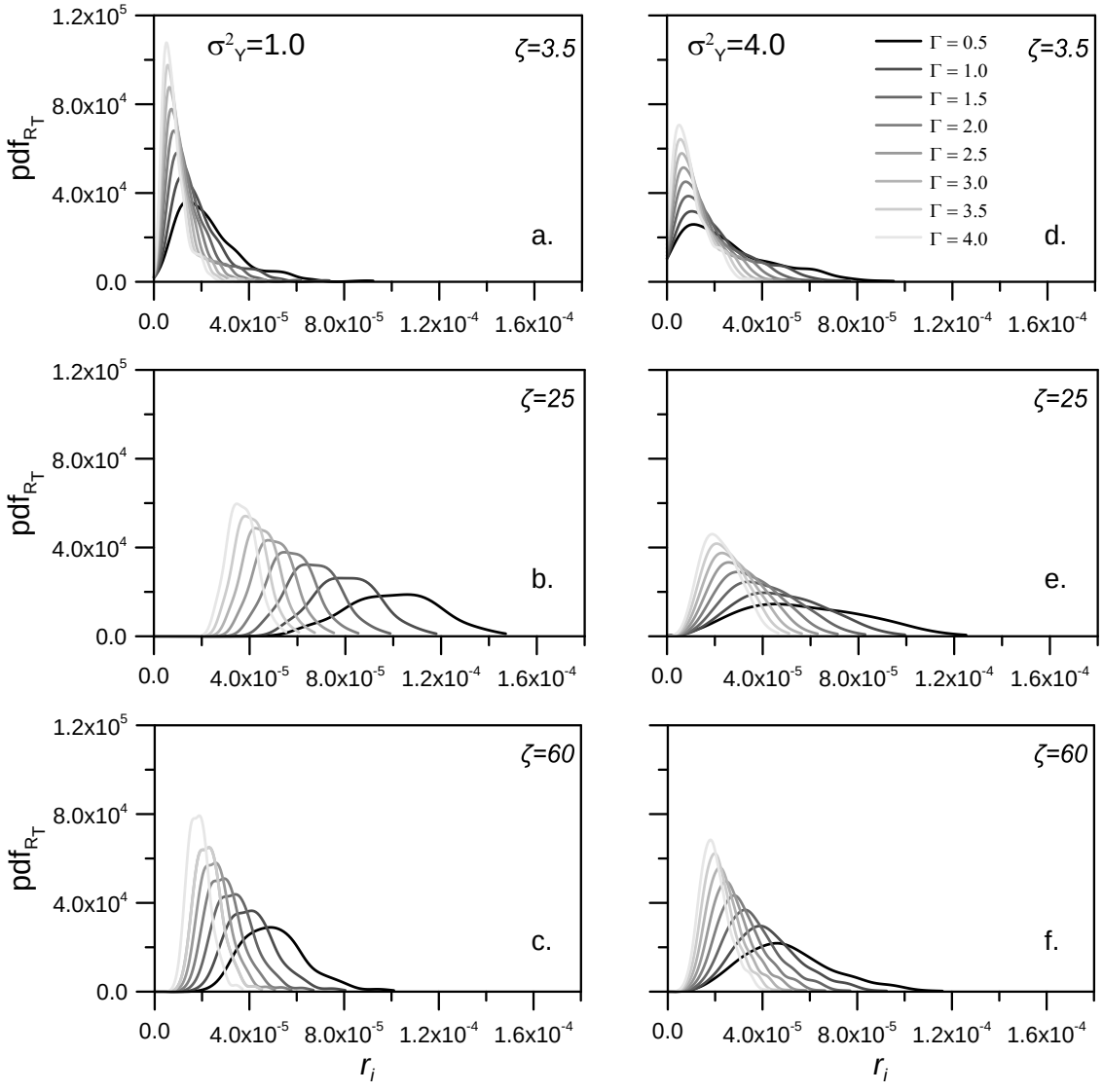

FIGURE 4.7: Probability Density Functions of the total ILCR for a series of mass release power coefficient at the control planes located at the normalized distances from the injection ξ =3.5, 25 and 60, and for a mildly (left hand) and a highly (right hand) heterogeneous hydraulic conductivity field.

of the risk, i.e. an apparent increase in the total risk variance (compare frames a-c and d-f in Figure 4.7).

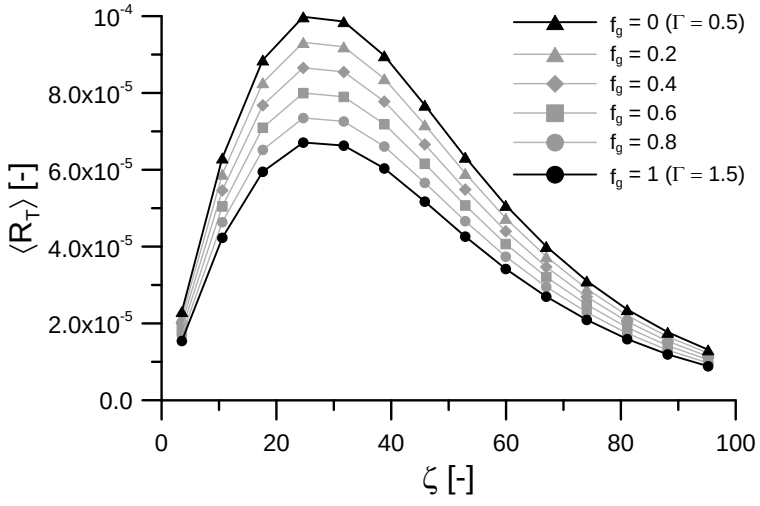

FIGURE 4.8: Impact of the fraction of ganglia on the expected total ILCR from chlorinated solvents simulations in a mildly heterogeneous hydraulic conductivity field ($\sigma_Y^2 = 1.0$) using $\Gamma_p = 0.5$ and $\Gamma_g = 1.5$.

4.4.3 Impact of a Two-domain style mass release model on the total ILCR

Expected R_T Next, we focus on the second mass depletion model accounting for the presence of both ganglia and pools in the source zone (Eq. 4.6 in subsection 4.2.2). Figure 4.8 shows the effect of applying different fractions of ganglia (f_g) on the propagation of the expected total ILCR along the aquifer longitudinal profile. Typically, by increasing f_g, the total risk moves linearly from the risk signal corresponding to the sole presence of pools ($R_T^{(\Gamma_g)}$) in the source zone to the risk signal corresponding to the sole presence of ganglia ($R_T^{(\Gamma_p)}$). The following simple additive relation is then observed:

$$R_T = R_T^{(\Gamma_g)} f_g + R_T^{(\Gamma_p)} f_p. \tag{4.21}$$

Using this relation, a large number of ganglia/pool fraction can be tested without significant computational cost when $R_T^{(\Gamma_g)}$ and $R_T^{(\Gamma_p)}$ are known.

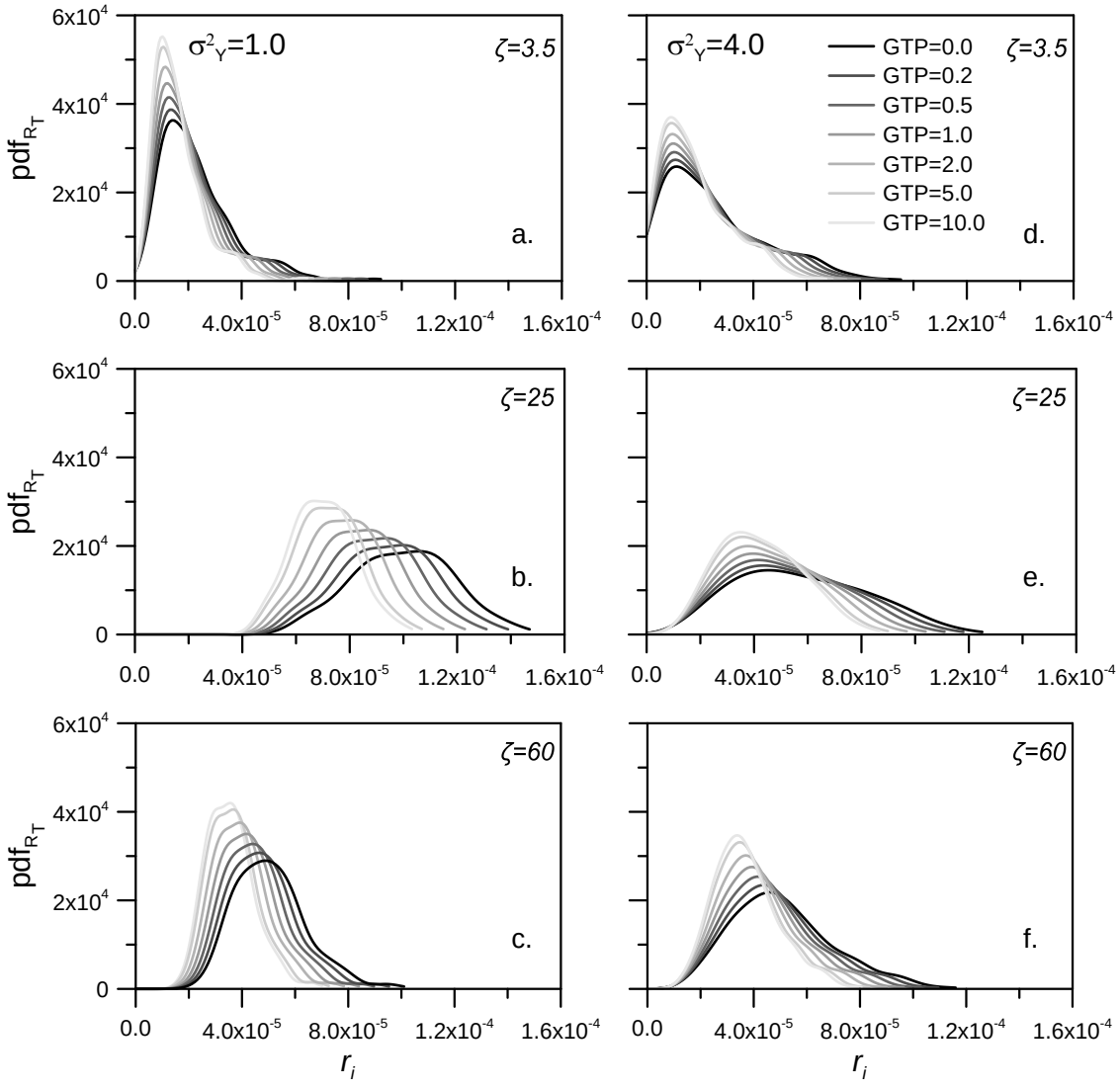

FIGURE 4.9: Probability Density Functions of the total ILCR for a series of Ganglia To Pool ratio at control planes located at the normalized distances from the injection ξ =3.5, 25 and 60, and for a mildly (left hand) and a highly (right hand) heterogeneous hydraulic conductivity field (respectively $\sigma^2_Y = 1.0$ and $\sigma^2_Y = 4.0$).

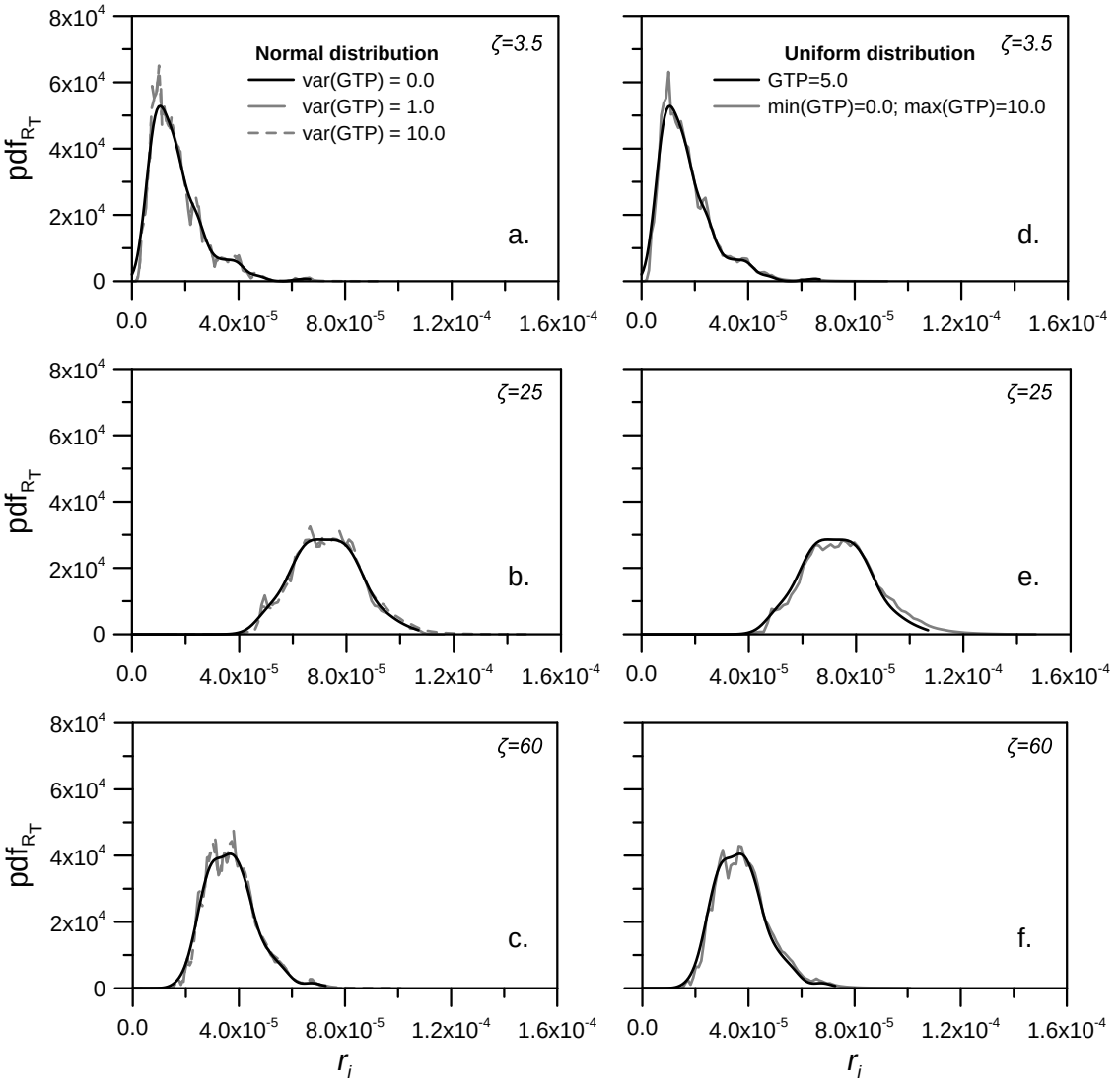

FIGURE 4.10: Probability Density Functions of the total ILCR considering a random Ganglia To Pool (GTP) ratio taken from a normal distribution (left hand, frames a, b and c) and from a uniform distribution (right hand, frames d, e, f) at control planes located at the normalized distances from the injection ξ =3.5, 25 and 60, and for a mildly heterogeneous hydraulic conductivity field ($\sigma^2_Y = 1.0$). Both distribution of the GTPs respects a mean of 5.0.

Ganglia to Pool ratio and Probability density functions of $\mathbf{R_T}$ This useful observation (Eq. 4.21) allows us to easily translate the expression of ganglia and pool fractions in terms of the more concise ganglia to pool (GTP) ratio from the pre-estimation of $R_T^{(\Gamma_g)}$ and $R_T^{(\Gamma_p)}$. Figure 4.9 shows the impact of the GTP ratio on the total risk *pdf*s. The more the GTP ratio tends to zero (i.e., the sole presence of pools in the source zone), the more the typical *pdf*s asymmetry is accentuated, with an increased tailing towards high risk values, especially near the source zone (Figure 4.9d). Once more, this spreading phenomenon is logically exaggerated by the heterogeneity in the flow field.

The GTP ratio can be treated as a random variable owing to the low computational cost of a total risk profile evaluation while using the linear relation expressed in Eq. 4.21. A total of 10^5 random values of GTP ratio were therefore randomly generated from a normal and a uniform distribution, both using a mean of 5.0. Figure 4.10 displays the resulting total risk *pdf*s. The randomization of the ganglia to pool ratio does not seem to have an impact on risk distributions, adding a simple noise around the mean risk.

4.5 Source Zone Efficiency

The above results highlight the temporal evolution of the contaminant mass release as a clear controlling factor of the human health risk. However, the source zone characterization involves additional complex processes such as the hydraulic conditions in its vicinity. In this section we investigate the potential impact of the water flux passing through the source zone. For each realization ir, we defined the corresponding source zone efficiency η_{ir} as the ratio between the volumetric water flux crossing the source zone $Q_{sz,ir}$ and an expected flow rate $\langle Q_{sz} \rangle$ defined as the average over all realizations, i.e.

$$\eta_{ir} = \frac{Q_{sz,ir}}{\langle Q_{sz} \rangle}. \tag{4.22}$$

Introduced by de Barros and Nowak [2010], the metric above (Eq. 4.22) is an indicator of the relative flux intensity passing through the source zone. Figure 4.11 displays this potential relationship between the total risk and the source zone efficiency.

Interestingly, an apparent power law correlation ($R_T = \alpha\, \eta^{\beta}$) can be observed. The negative correlation implies a beneficial effect of η on the system, i.e. the total ILCR

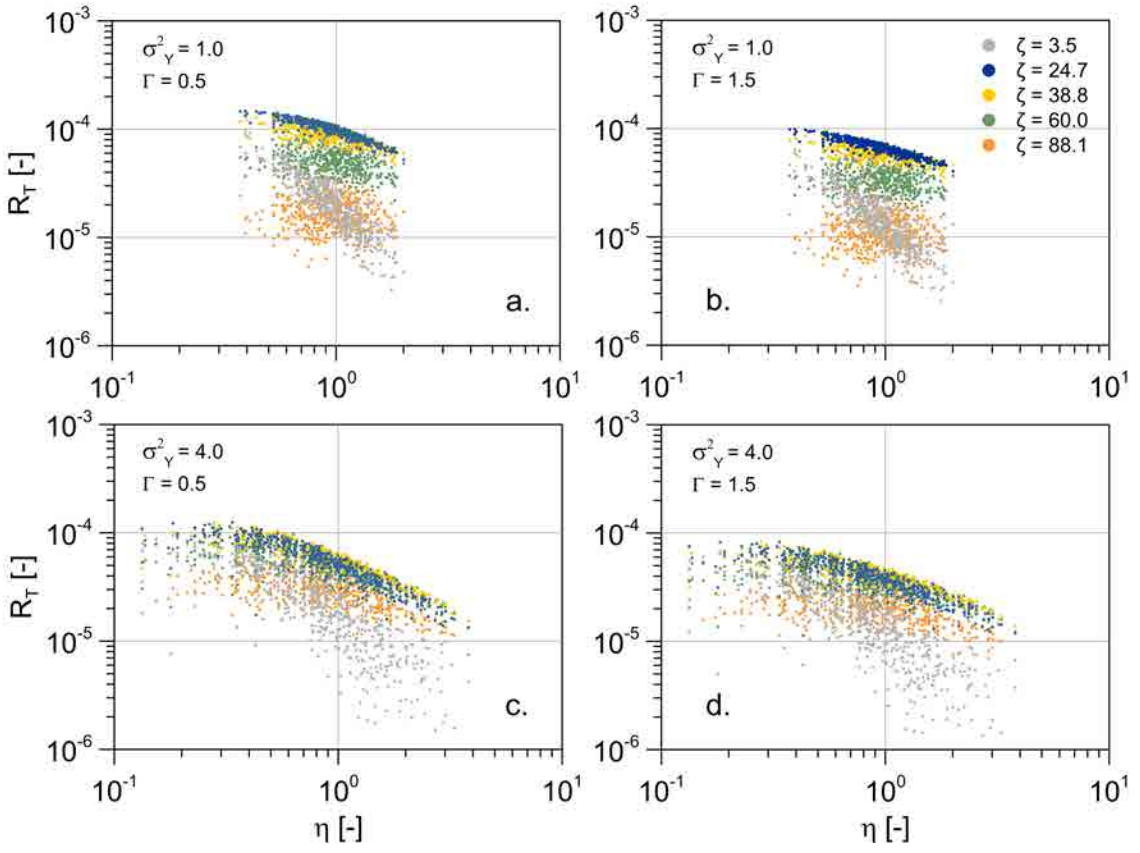

FIGURE 4.11: Relationship between the source zone efficiency and the total increase lifetime cancer risk obtained for each simulation at selected control planes. Right hand figures (frames a and c) shows the relationship for a power DNAPL mass transfer exponent Γ of 0.5 (pool), left hand (frames b and d) for a Γ of 1.5 (ganglia) for a mildly (top) and a highly (bottom) heterogeneous hydraulic conductivity field (respectively $\sigma^2_Y = 1.0$ and $\sigma^2_Y = 4.0$).

decreases when the source efficiency increases. By performing a regression analysis, we obtain the power exponent of the data set in Figure 4.11. The power exponent informs us about the degree of sensitivity of R_T to η and the regression coefficient of determination can be seen as an indicator of the degree of correlation. Figure 4.12 expresses total risks that are highly sensitive to the source zone efficiency at short distances. The degree of correlation between the risk and the water flux passing through the source zone is relatively high at short traveled distances and decreases downstream of the hot spot (near $D_R > 1$). Surprisingly, the degree of correlation is highest near the hot spot location, where the effective threat to human health is the highest. Both sensitivity and correlation between the two variables are mitigated by increasing the heterogeneity in the Y-field

(Figure 4.12b). On the other hand, conceptualizing the source zone by ganglia ($\Gamma = 1.5$) tends to decrease the dependence of the total risk on the source zone efficiency (lower absolute value of the β power law exponent and of the coefficient of determination).

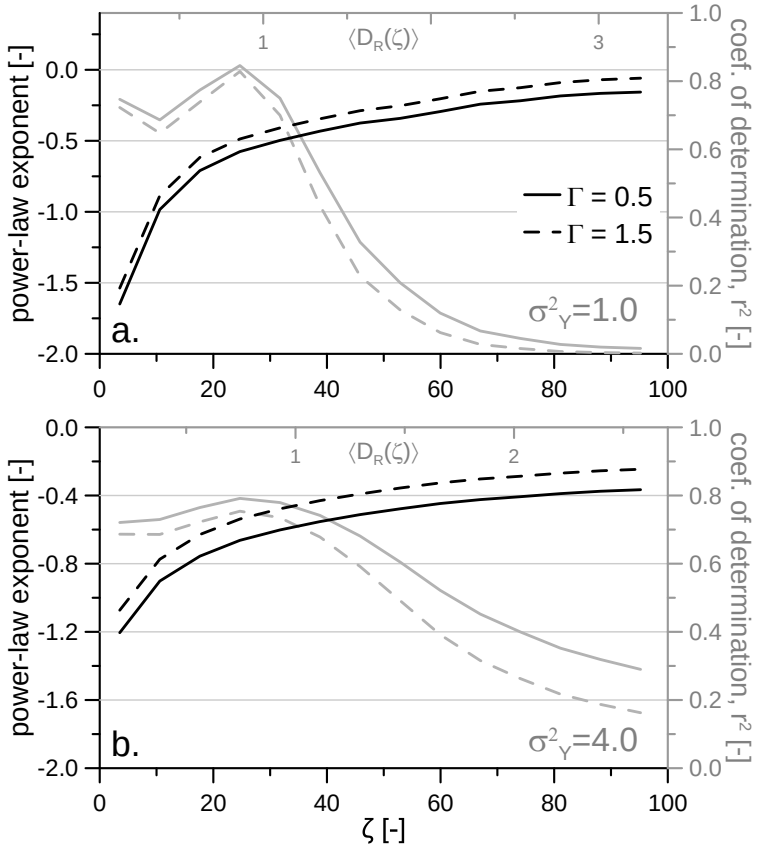

FIGURE 4.12: Power regression coefficient as a function of the normalized traveled distance (bottom x-axis) and corresponding mean toxicity-based Damköhler (top x-axis) for a power DNAPL mass transfer exponent Γ of 0.5 (solid line) and 1.5 (dashed line) and for a mildly (top) and a highly (bottom) heterogeneous hydraulic conductivity field (respectively $\sigma^2_Y = 1.0$ and $\sigma^2_Y = 4.0$). Grey lines shows the coefficient of determination of the regression (right hand axis).

As shown in Henri et al. [2015], plume travel times control the effective risk attributed to a chemical mixture in a non-trivial manner. To sum up, increasing the advective time will result (1) in an increase in the total risk beyond the mean hot spot location characterized by a toxicity-based Damkölher number below 1 (zone of production of highly toxic subspecies), and (2) in a decrease in the threat in zones with $D_R > 1$ above 1, between the source zone and the mean hot spot location (zone of destruction of highly

toxic subspecies). Increasing the source zone efficiency will generate lower travel times in areas of production of daughter compounds ($D_R > 1$), which will increase the probability to decrease the risk near the source zone. This decrease in risk is also observed when the plume moves downstream but vanishes progressively owing to the spread of the plume and to the degradation of η as a good indicator of travel time.

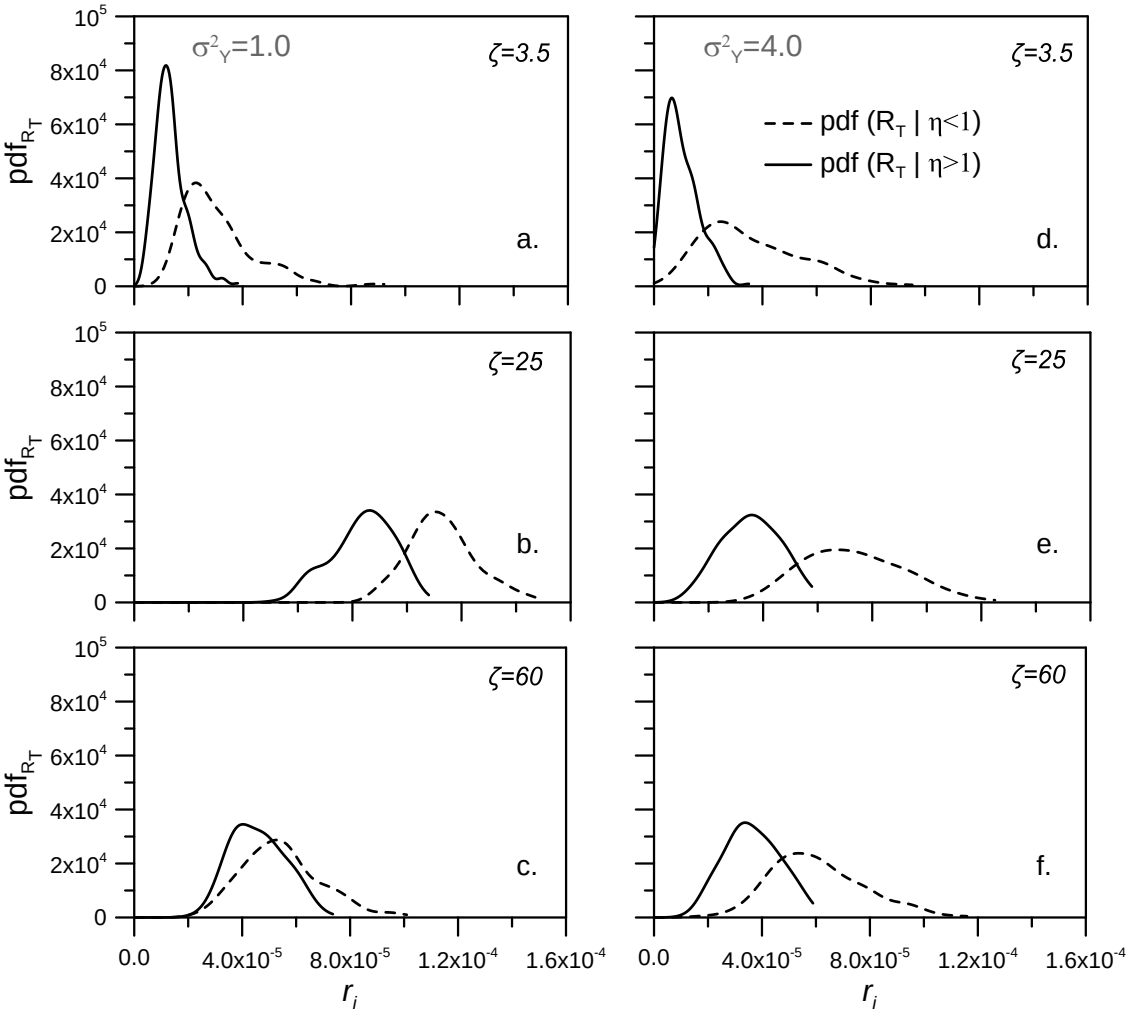

FIGURE 4.13: Probability Density Functions of the total ILCR conditioned to a source zone efficiency lower than 1 (dashed line) and higher than 1 (solid line) at control planes located at the normalized distances from the injection ξ =3.5, 25 and 60, and for a mildly (left hand) and a highly (right hand) heterogeneous hydraulic conductivity field (respectively $\sigma_Y^2 = 1.0$ and $\sigma_Y^2 = 4.0$).

Conditional probability density functions of R_T In order to illustrate the potential importance of the water flux crossing the source zone in the total ILCR profile, we conditioned the *pdf*s of R_T on η, and characterized the risk distribution for a source zone efficiency with $\eta < 1$ and $\eta > 1$.

The analysis was performed using the set of simulations related to a pool fully-dominated source zone ($\Gamma = 0.5$). Figure 4.13 shows the clear difference of total risk distribution for the two conditions. Relatively high water flux passing through the DNAPL source zone leads to lower total risk values (as explained above) with a clear difference at the hot spot location (Figure 4.13b,e). Total risk *pdf*s conditioned by a $\eta > 1$ also display a lower variance, e.g. less uncertainty, especially at short distances from the source zone. Again, the non triviality of the impact of travel times on the effective ILCR in case of chemical mixtures accounts for these observations.

4.6 Conclusions

This work investigates the human health risk response to DNAPL source zone behavior. The human health risk due to the release of the chlorinated solvent PCE and to the reactive transport of its carcinogenic biodegradation products was characterized stochastically through Monte Carlo simulations considering uncertain hydraulic properties.

DNAPL mass release and Expected Risk, Uncertainty Results show that mass release models control significantly the human health risk. The statistical analysis of the increased lifetime cancer risk due to a mixture of chlorinated solvents demonstrated a lower threat when the DNAPL source zone was mostly formed of ganglia. The detrimental impact of the presence of DNAPL pools is also clearly shown while using the exceedence of MCLs as a risk metric. Moreover, we show that in the presence of network reaction systems, the DNAPL mass release mode, when modeled by an upscaled contaminant mass transfer from a source zone, does not affect the hot spot location (area of higher risk). We confirm the observations made in [Henri et al., 2015] that highlight a risk-based Damköhler number (depending on travel time and on species-dependent reaction kinetics and toxicities) as the right metric to predict hot spot locations. The amplitude

of the total risk follows a scaling factor sensitive to both source zone mass release and heterogeneity in the hydraulic conductivity. Moreover, we show that the conceptualization of DNAPL mass release has a significant impact on the uncertainty of the human health risk estimation. Globally, an increase in the pooling-effect decreases the reliability of the expected risk values.

Impacts of a Two-domain Mass Depletion Model The propagation of the effective lifetime cancer risk is then analyzed as a result of a simplified two-domain DNAPL mass depletion model. Outputs show that the risk profile resulting from a source zone constituted by ganglia and pools can be evaluated by a simple linear combination of the risk profile solutions of a pool dominated source zone and a ganglia dominated source zone. Interestingly, results display a higher uncertainty in the risk prediction when the proportion of pool in the source zone is increased. Moreover, the ganglia to pool ratio is considered for the first time as an uncertain parameter. We show that this additional source of uncertainty does not have a significant impact on a lifetime cancer risk prediction based on an expected ganglia-to-pool ratio.

The Role of Source-zone Efficiency As a complement to the above analysis of the low statistical moments of risk, our work highlights the potential impact of the water flux passing through the source zone on the effective increased lifetime cancer risk due to a reactive chemical mixture. Counter-intuitively, the source zone efficiency is shown to have a beneficial effect on the risk. The total risk tends indeed to decrease for high source zone efficiency due to the consequential decrease in travel times near the source zone, which may limit the production of highly toxic daughter products.

Conclusions

The increasing presence of toxic chemicals released in the subsurface has led to a rapid growth of social concerns and the need to develop and employ models that can predict the impact of groundwater contamination on human health risk under uncertainty. Monitored natural attenuation is a common remediation action in many contamination cases, but can lead to the production of subspecies of distinct toxicity that may pose challenges in pollution management strategies. The actual risk that these contaminants pose to human health depends on the interplay between the complex structure of the geological media and the kinetic and toxicity of each pollutant byproduct. Modeling multispecies reactive transport in natural systems with strong heterogeneities at divers scales and complex biochemical reactions is therefore a major challenge for assessing accurately the risk posed by groundwater polluted sites with organic and inorganic contaminants. The following paragraphs will conclude this thesis by exposing the advances done in (1) the development of efficient and stable numerical solutions to model the fate and transport of multispecies biochemical systems in heterogeneous porous media, and (2) the risk assessment of complex contamination (by the presence of multispecies reactive systems or non-trivial source zone behavior) under heterogeneous and uncertain conditions.

Results Summary

Numerical methods The first chapter presents a random-walk particle tracking method capable to efficiently simulating the motion of particles affected by first-order network reactions in three-dimensional systems, which are represented by spatially variable physical and biochemical coefficients described at high resolution. The approach is based on the the development of transition probabilities that describe the likelihood that particles belonging to a given species and location at a given time will be transformed into and moved to another species and location afterward. The method is fully coupled with reactions, free of numerical dispersion and overcomes the inherent numerical problems stemming from the incorporation of heterogeneities to reaction transport codes. In doing this, we demonstrate that the motion of particles follows a standard random-walk with time-dependent effective retardation and dispersion parameters that depend on the initial and final chemical state of the particle. Moreover, explicit analytic solutions of the transition probability matrix and related particle motions are provided for serial reactions. An example of the effect of heterogeneity on the dechlorination of organic solvents in a three-dimensional random porous media shows that the power-law behavior typically observed in conservation tracers breakthrough curves can be largely compromised by the effect of biochemical reactions.

In the second chapter, we present a versatile particle method able to simulate contaminant plumes moved by advection-dispersion and affected by network reactions and multirate mass transfer processes under spatially heterogeneous conditions. The stochastic approach is based on the derivation of the probability that a particle being at a certain position, specie and mobility zone will move into another specie and/or zone. The particle method is free of numerical dispersion and overcomes the inherent numerical problems stemming from the incorporation of heterogeneities into reactive transport codes based on Eulerian approaches. We attempt to isolate the specific effect of both processes by proceeding to a sensitivity analysis and show this way the importance of their consideration. Illustratively, we apply our method to model the sequential degradation of chlorinated solvents (PCE $\rightarrow$ TCE $\rightarrow$ DCE $\rightarrow$ VC $\rightarrow$ 0) into a finely discretized field and show how spatially variable coefficients of bio-decay and mass transfer affect the spatial and temporal behavior of the four reactive plumes.

Risk Assessment The third chapter addresses human health risk for chemical mixtures (such as chlorinated solvents) under uncertainty through high resolution three-dimensional numerical simulations. We systematically investigate the interaction between aquifer heterogeneity, flow connectivity, contaminant injection model and chemical toxicity in the probabilistic characterization of health risk. We illustrate how chemical-specific travel times control the regime of the expected risk and its corresponding uncertainties. Results indicate conditions where preferential flow paths can favor the reduction of the overall risk of the chemical mixture. The overall human risk response to aquifer connectivity is shown to be non-trivial for multispecies transport. This non-triviality is a result of the interaction between aquifer heterogeneity and chemical toxicity. To quantify the joint effect of connectivity and toxicity in health risk, we propose a toxicity-based Damköhler number. Furthermore, we provide a statistical characterization in terms of low-order moments and the probability density function of the individual and total risks.

To finish, the fourth and last chapter focuses on the impact of the DNAPL release mode on the human health risk propagation along the aquifer under uncertain conditions. We simulate the release and the transport of the chlorinated solvent Perchloroethylene and its carcinogenic degradation products in randomly heterogeneous porous media. The human health risk posed by the chemical mixture of these contaminants is characterized by the low-order statistics and the probability density function of common risk metrics. We show that the zone of high risk (hot spot) is independent of the DNAPL mass release mode, and that the risk amplitude is mostly controlled by heterogeneities and by the source zone architecture. The risk is lower and less uncertain when the source zone is formed mostly by ganglia than by pools. We also illustrate how the source zone efficiency (intensity of the water flux crossing the source zone) affects the risk posed by an exposure to the chemical mixture. Results display that high source zone efficiencies are counter-intuitively beneficial, decreasing the risk because of a reduction in the time available for the production of the highly toxic subspecies.

Opening for Future Researches

This thesis contributed to the improvement of risk management under complex contamination conditions. A great (and sometimes frustrating) attribute of sciences is the

inevitable avalanche of questions arising from the answering of a single one. After this thesis, the issues stay therefore numerous and the challenge exiting. Here are few thoughts and example of remaining topics in line with the researches exposed in this dissertation:

- *Near-future evolution of RW3D.* The random walk particle tracking code RW3D can now handle a wide range of simulation scenarios (any combination of single or multirate mass transfer, linear sorption, serial or generic first-order decay network reaction, ...). You will find in Appendix E a quick description of the algorithm architecture and required inputs. One of the main limitations of RW3D is the impossibility to impose temporal variability in the groundwater flux and in the biogoechemical system. One could say that this lack reflects the actual philosophy of the "stochastic hydrogeology community" that focuses its efforts more on space than on time. Incorporating transient water flux and biochemical conditions in the particle tracking code will open great opportunities (1) to increase our understanding of the subsurface contamination temporality and (2) to assess the impact of this temporality (in a stochastic manner?) on populations exposure to contaminants. It is also planed to incorporate non-linear bimolecular reactions in RW3D. This will allow a more sophisticated simulation of biodegradation processes based per instance on Michaelis-Menten-Monod type of models. Despite the potential subsequent lose of efficiency, this may initiate interesting investigations to better understand the complex interaction between hetereogeneities in hydrodynamic properties of the porous media and the transport of reactive contaminants.

- *Application to in-situ conditions.* Through the newly developed numerical methods to model biochemical reactive systems in heterogeneous porous media, we aim to propose an efficient and applicable alternative to simulate complex contamination scenarios in a stochastic manner. The conceptual model presents however important simplification such as the approximation of biochemical reactions by first-order decay networks. The validation of our approach should obviously pass by an application to a real and well monitored contaminated site.

- *Spatial variability of biogeochemical conditions.* The presence of a strong degree of heterogeneity in the biogoechimical conditions within aquifers is more and more documented, and few studies already shown the significant impact of this spatial

variability on the solute transport. The chapter 3 of the thesis uses the assumption of a negative correlation between hydraulic conductivity and first-order decay rates. However, the controlling factors of the biochemical spatial variability are not fully understood. More research effort should be allocated to the better understanding of this additional source of spatial variability. However, regarding the multitude of processes engaged in biogeochemical reactions, uncertainties in the spatial distribution of the parameters will most certainly remain. In this context, adapted stochastic approaches may be developed.

APPENDICES

APPENDIX A

Derivation of First Spatial Moments

From equation (1.16), the solution matrix of the absolute first spatial moment (x-direction) satisfies the following system of ordinary differential equations

$$\frac{d\mathbf{X}_x}{dt} = \frac{q'_x}{\phi}\mathbf{R}^{-1}\mathbf{P}(t) + \mathbf{K}\,\mathbf{X}_x, \tag{A.1}$$

subject to the initial condition

$$\mathbf{X}_x(t=0) = \mathbf{0} \tag{A.2}$$

where the matrix $\mathbf{X}_x$ is the $n_s \times n_s$ absolute first spatial moment matrix. The matrix $\mathbf{R}^{-1}$ is a diagonal matrix composed by the inverse of the retardation factors, and $\mathbf{K}$ is the reaction matrix. The parameter q'_x and ϕ represent the particle Darcy velocity in the x-direction and the porosity of the medium, respectively. $\mathbf{P}(t)$ is the species state transition probability matrix. Defining the matrix $\mathbf{Y}_x(t)$ by

$$\mathbf{Y}_x(t) = \frac{q_x'}{\phi}\mathbf{R}^{-1}\mathbf{P}(t), \tag{A.3}$$

leads to the following system of equations

$$\frac{d\mathbf{X}_x}{dt} = \mathbf{Y}_x(t) + \mathbf{K}\,\mathbf{X}_x, \tag{A.4}$$

whose solution is

$$\mathbf{X}_x(t) = \int_0^t \exp(\mathbf{K}(t-s))\mathbf{Y}_x(s)ds. \tag{A.5}$$

After the diagonalization of $\mathbf{K}$ by $\mathbf{K} = \mathbf{S}\mathbf{K}'\mathbf{S}^{-1}$, the solution can be written as

$$\mathbf{X}_x(t) = \int_0^t \mathbf{S}\exp(\mathbf{K}'(t-s))\mathbf{S}^{-1}\mathbf{Y}_x(s)ds, \tag{A.6}$$

where $\mathbf{S}$ is the transformation matrix composed by the eigenvalues of the reaction matrix $\mathbf{K}$, and $\mathbf{K}'$ is the diagonal matrix whose components are the eigenvalues of $\mathbf{K}$. The component $X_{x,ij}$ of this matrix (A.6) is expressed as

$$X_{x,ij}(t) = \sum_{p,q=1}^{n_s} S_{ip}S_{pq}^{-1}\int_0^t \exp(K_{pp}^{'}(t-s))Y_{x,qj}(s)ds, \tag{A.7}$$

where

$$Y_{x,qj}(s) = \frac{q_x'}{\phi R_{qq}}P_{qj}(s). \tag{A.8}$$

From (1.20), the species state transition probability matrix can also be expressed in terms of the eigenvalues and eigenvectors of $\mathbf{K}$ by

$$P_{qj}(s) = \sum_{r} S_{qr}\ \exp(K'_{rr}s)\, S^{-1}_{rj}. \tag{A.9}$$

The first absolute moment of a particle plume that moves from species j to species i after a time interval t can be obtained by respectively introducing (A.9) and (A.8) into (A.8) and (A.7),

$$X_{x,ij}(t) = \frac{q'_x t}{\phi} \sum_{p,q,r=1}^{n_s} \frac{S_{ip}S^{-1}_{pq}S_{qr}S^{-1}_{rj}}{R_{qq}} F_{pr}(t), \tag{A.10}$$

where

$$F_{pr}(t) = \frac{1}{t}\int_0^t \exp(K'_{pp}(t-s))\exp(K'_{rr}s)ds. \tag{A.11}$$

The solution of this integral is

$$F_{pr}(t) = \begin{cases} \dfrac{\exp(K'_{pp}t) - \exp(K'_{rr}t)}{t\,(K'_{pp} - K'_{rr})}, & \text{if } p \neq r \\ \\ \exp(K'_{rr}t), & \text{if } p = r \end{cases} \tag{A.12}$$

Based on this, the normalized first absolute spatial moments can be written as

$$A_{ij,x}(t) = \frac{X_{x,ij}}{P_{ij}} = \frac{q'_x t}{\phi R^e_{ij}(t)}, \tag{A.13}$$

where $R^e_{ij}(t)$ is an effective retardation coefficient defined by

$$\frac{1}{R^e_{ij}(t)} = \frac{1}{P_{ij}(t)} \sum_{p,q,r=1}^{n_s} \frac{S_{ip}S^{-1}_{pq}S_{qr}S^{-1}_{rj}}{R_{qq}} F_{pr}(t). \tag{A.14}$$

APPENDIX B

Derivation of Second Spatial Moments

From equation (1.17), the solution matrix of the absolute second spatial moment (xy-component) satisfies the following system of ordinary differential equations

$$\frac{d\boldsymbol{\Psi}_{xy}}{dt} = \frac{q'_y}{\phi}\mathbf{R}^{-1}\mathbf{X}_x + \frac{q'_x}{\phi}\mathbf{R}^{-1}\mathbf{X}_y + 2D_{xy}\mathbf{R}^{-1}\mathbf{P} + \mathbf{K}\boldsymbol{\Psi}_{xy}, \tag{B.1}$$

subject to the initial condition

$$\boldsymbol{\Psi}_{xy}(t=0) = \mathbf{0} \tag{B.2}$$

where the component $\Psi_{xy,ij}$ represents the temporal evolution of the absolute second moment of a particle plume originally belonging to species j and turning into species i in the time interval t. Defining

$$\mathbf{Y}_{xy}(t) = \frac{q'_y}{\phi}\mathbf{R}^{-1}\mathbf{X}_x + \frac{q'_x}{\phi}\mathbf{R}^{-1}\mathbf{X}_y + 2D_{xy}\mathbf{R}^{-1}\mathbf{P}, \tag{B.3}$$

we obtain the following inhomogeneous first-order linear differential equation system

$$\frac{\partial \mathbf{\Psi}_{xy}}{\partial t} = \mathbf{Y}_{xy}(t) + \mathbf{K}\mathbf{\Psi}_{xy}(t). \tag{B.4}$$

The solution of (B.4) is

$$\mathbf{\Psi}_{xy}(t) = \int_0^t \exp(\mathbf{K}(t-s))\mathbf{Y}_{xy}(s)ds. \tag{B.5}$$

After the diagonalization of $\mathbf{K}$ by $\mathbf{K} = \mathbf{S}\mathbf{K}'\mathbf{S}^{-1}$, this solution can be written as

$$\mathbf{\Psi}_{xy}(t) = \int_0^t \mathbf{S}\exp(\mathbf{K}'(t-s))\mathbf{S}^{-1}\mathbf{Y}_{xy}(s)ds, \tag{B.6}$$

where $\mathbf{S}$ is the transformation matrix composed by the eigenvalues of the reaction matrix $\mathbf{K}$, and $\mathbf{K}'$ is the diagonal matrix whose components are the eigenvalues of $\mathbf{K}$. The component $\Psi_{xy,ij}$ of this matrix (B.6) can be expressed as

$$\Psi_{xy,ij}(t) = \sum_{a,b=1}^{n_s} S_{ia}S_{ab}^{-1}\int_0^t \exp(K'_{aa}(t-s))Y_{xy,bj}(s)ds. \tag{B.7}$$

From (B.3), the component $Y_{xy,bj}$ is

$$Y_{xy,bj}(s) = \frac{q'_y}{\phi R_{bb}}X_{x,bj}(s) + \frac{q'_x}{\phi R_{bb}}X_{y,bj}(s) + \frac{2D_{xy}}{R_{bb}}P_{bj}(s). \tag{B.8}$$

Substituting (A.9) and (A.10) into (B.8) and (B.7) we obtain

$$\begin{aligned}\Psi_{xy,ij}(t) &= 2D_{xy}t\sum_{a,b,u=1}^{n_s}\frac{S_{ia}S_{ab}^{-1}S_{bu}S_{uj}^{-1}}{R_{bb}}F_{au}(t) \\ &\quad + \frac{2q'_xq'_yt^2}{\phi^2}\sum_{a,b,p,q,r=1}^{n_s}\frac{S_{ia}S_{ab}^{-1}S_{bp}S_{pq}^{-1}S_{qr}S_{rj}^{-1}}{R_{bb}R_{qq}}H_{apr}(t),\end{aligned} \tag{B.9}$$

where $F_{au}(t)$ is defined in (A.12) and $H_{apr}(t)$ is

$$H_{apr}(t) = \frac{1}{t^2} \int_0^t \exp(K'_{aa}(t-s)) s F_{pr}(s) ds. \tag{B.10}$$

The solution of this integral can be written as

$$H_{apr}(t) = \begin{cases} \dfrac{F_{ap}(t) - F_{ar}(t)}{t\left(K'_{pp} - K'_{rr}\right)}, & \text{if } p \neq r \\ \\ W_{ar}(t), & \text{if } p = r \end{cases} \tag{B.11}$$

where

$$W_{ar}(t) = \begin{cases} \dfrac{\exp(K'_{rr}t)\left[(K'_{rr} - K'_{aa})t - 1\right] + \exp(K'_{aa}t)}{t^2\ \left(K'_{aa} - K'_{rr}\right)^2}, & \text{if } a \neq r \\ \\ \exp(K'_{aa}t)/2, & \text{if } a = r \end{cases} \tag{B.12}$$

Based on this, the normalized second absolute spatial moment can be written as

$$B'_{xy,ij}(t) = \frac{2D_{xy}}{R^e_{ij}(t)} t + \frac{2q'_x q'_y}{\phi^2 G_{ij}(t)} t^2, \tag{B.13}$$

where

$$G_{ij}(t) = P_{ij}(t) \left(\sum_{a,b,p,q,r=1}^{n_s} \frac{S_{ia} S^{-1}_{ab} S_{bp} S^{-1}_{pq} S_{qr} S^{-1}_{rj}}{R_{bb} R_{qq}} H_{apr}(t) \right)^{-1}. \tag{B.14}$$

Knowing (1.22) and (A.13), the second central spatial moment is

$$B_{xy,ij}(t) = \frac{2D_{xy}}{R^e_{ij}(t)} t + \frac{2q'_x q'_y}{\phi^2 R^e_{ij}(t)} \left(\frac{R^e_{ij}(t)}{G_{ij}(t)} - \frac{1}{2R^e_{ij}(t)} \right) t^2. \tag{B.15}$$

APPENDIX C

ANALYTICAL DETERMINATION OF THE EIGENSYSTEM FOR A SIMPLIFIED TWO-SPECIES AND DOUBLE POROSITY PROBLEM

Let us first recall the definition of our three dimensionless variables

$$\tau = \frac{k_m}{R_m}\, t, \tag{C.1}$$

$$\chi = \frac{R_m\, k_{im}}{R_{im}\, k_m}, \tag{C.2}$$

$$Da_{II} = \frac{k_m}{\alpha\, R_m}, \tag{C.3}$$

The governing equation (2.12)-(2.11) can be written in dimensionless form for a two-species system affected by a single rate mass transfer as:

$$\begin{aligned}
\frac{d\mu_1^m}{d\tau} + \quad \frac{d\mu_1^{im}}{d\tau} &= -\mu_1^m - \chi\mu_1^{im} \\
\frac{d\mu_1^{im}}{d\tau} &= Da_{II}^{-1}\beta\mu_1^m - Da_{II}^{-1}\mu_1^{im} - \chi\mu_1^{im} \\
\frac{d\mu_2^m}{d\tau} + \quad \frac{d\mu_2^{im}}{d\tau} &= \mu_1^m - \mu_2^m + \chi\mu_1^{im} - \chi\mu_2^{im} \\
\frac{d\mu_2^{im}}{d\tau} &= Da_{II}^{-1}\beta\mu_2^m - Da_{II}^{-1}\mu_2^{im} + \chi\mu_1^{im} - \chi\mu_2^{im}
\end{aligned} \tag{C.4}$$

This system can be written in term of matrix as in (2.14) defining the architecture matrix $\mathbf{A}$ and reaction matrix $\mathbf{B}$ as:

$$\mathbf{A} = \begin{bmatrix} 1 & 1 & 0 & 0 \\ 0 & 1 & 0 & 0 \\ 0 & 0 & 1 & 1 \\ 0 & 0 & 0 & 1 \end{bmatrix} \tag{C.5}$$

$$\mathbf{B} = \begin{bmatrix} -1 & -\chi & 0 & 0 \\ Da_{II}^{-1}\beta & -Da_{II}^{-1} - \chi & 0 & 0 \\ 1 & \chi & -1 & -\chi \\ 0 & \chi & Da_{II}^{-1}\beta & -Da_{II}^{-1} - \chi \end{bmatrix}, \tag{C.6}$$

which give the matrix $\mathbf{A}^{-1}\mathbf{B}$

$$\mathbf{A}^{-1}\mathbf{B} = \begin{bmatrix} -Da_{II}^{-1}\beta - 1 & Da_{II}^{-1} & 0 & 0 \\ Da_{II}^{-1}\beta & -Da_{II}^{-1} - \chi & 0 & 0 \\ 1 & 0 & -Da_{II}^{-1}\beta - 1 & Da_{II}^{-1} \\ 0 & \chi & Da_{II}^{-1}\beta & -Da_{II}^{-1} - \chi \end{bmatrix}. \tag{C.7}$$

The eigensytem of a such matrix can be obtained analytically. The four eigenvalues are given by $\lambda = \begin{bmatrix} \lambda_1 & \lambda_1 & \lambda_2 & \lambda_2 \end{bmatrix}^T$ where

$$\begin{aligned}\lambda_1 = \; & \frac{1}{2}\sqrt{Da_{II}^{-2}\beta^2 + 2\,Da_{II}^{-1}\left(Da_{II}^{-1} - \chi + 1\right)\beta + \left(Da_{II}^{-1} + \chi - 1\right)^2} \\ & + \frac{1}{2}\left(-\beta - 1\right)Da_{II}^{-1} - \frac{\chi}{2} - \frac{1}{2},\end{aligned}$$

$$\begin{aligned}\lambda_2 = \; & -\frac{1}{2}\sqrt{Da_{II}^{-2}\beta^2 + 2\,Da_{II}^{-1}\left(Da_{II}^{-1} - \chi + 1\right)\beta + \left(Da_{II}^{-1} + \chi - 1\right)^2} \\ & + \frac{1}{2}\left(-\beta - 1\right)Da_{II}^{-1} - \frac{\chi}{2} - \frac{1}{2}.\end{aligned}$$

The matrix of eigenvectors is defined by:

$$\mathbf{S} = \begin{bmatrix} S1_1 & 0 & S1_2 & 0 \\ S2_1 & 0 & S2_2 & 0 \\ S3_1 & 0 & S3_2 & 0 \\ 1 & 0 & 1 & 0 \end{bmatrix} \tag{C.8}$$

where

$$\begin{aligned} S1_i = \; & \frac{\gamma_i\,Da_{II}^{-1}}{\left(Da_{II}^{-1} + \lambda_i + \chi\right)\left(Da_{II}^{-1}\beta + \lambda_i + 1\right)\Psi_i} \\ S2_i = \; & \frac{\gamma_i}{\left(Da_{II}^{-1} + \lambda_i + \chi\right)\Psi_i} \\ S3_i = \; & \frac{\left(\left(Da_{II}^{-1}\beta + \lambda_i + 2\right)\chi + Da_{II}^{-1} + \lambda_i\right)Da_{II}^{-1}}{\Psi_i} \end{aligned}$$

after the definition of Ψ_i and γ_i as:

$$\begin{aligned}\Psi_i = \; & \left(-Da_{II}^{-1}\beta - \lambda_i - 1\right)\chi^2 + \left(Da_{II}^{-2}\beta^2 + \left(\left(\beta - 1\right)\lambda_i + 2\,\beta - 1\right)Da_{II}^{-1} + \lambda_i + 1\right)\chi \\ & + Da_{II}^{-2}\beta,\end{aligned}$$

$$\gamma_i = \left(\left(Da_{II}^{-1}\beta + \lambda_i + 1\right)\chi + \left(1 + \left(\beta + 1\right)\lambda_i\right)\left(Da_{II}^{-1}\right) + {\lambda_i}^2 + \lambda_i\right)\beta\,\left(\chi + 1\right)Da_{II}^{-2}$$

APPENDIX D

The Total Risk Critical Time and Distance

A closed-form analytical solution of the critical distance x_c and the critical time t_c at which the total increased lifetime cancer risk (ILCR) reaches a maximum value is derived in this appendix. We start by noticing that since $\bar{c}_i(x)$ only depends on x and the partial differential equations describing contaminant transport constitutes a linear system, the critical distance x_c is independent of the temporal evolution of the source term $c_s(t)$. This term will only affect the intensity of the total risk but not its critical position. Based on this, it is mathematically convenient to solve the critical distance x_c for a Dirac-input source of the form $Q_s c_s(t) = m_0 \delta(t)$, where m_0 is the total initial contaminant mass of PCE at the source zone.

By the definition of the maximum running averaged flux-concentration obtained at the x-control plane we have that

$$Q_d \, \bar{c}_i(x) \, ED = \int_{t_p - \frac{ED}{2}}^{t_p + \frac{ED}{2}} Q_d \, c_i(t; x) \, dt \tag{D.1}$$

where Q_d is the total flow rate passing through the x-control plane, and t_p is the time where the risk reaches its maximum point. In the limit, when $ED \to \infty$, the integral in the right-hand-side of equation (D.1) is simply the total mass of species i recovered at the control plane. The exposure duration ED is typically a large number ranging between 30 years (non-carcinogens) and 70 years (for carcinogens). In this situation, this integral can be seen as some proportion α of the total mass. Imagine, for instance, that the concentration profile is Gaussian and ED is about 4 standard deviations, in this case, $\alpha = 95\%$. This reasoning suggests that one can approximate the integral in (D.1) by

$$Q_d\, \bar{c}_i(x)\, ED \approx \alpha\, M_i \left(\frac{d(x)}{v_a} \mathcal{R}_i^e \right), \tag{D.2}$$

where $d(x) = x - x_{inj}$ is the distance from the source zone to the x location, and v_a is the apparent velocity of groundwater (defined from the mean arrival time of a conservative species at the x control plane as $v_a = d(x)/\bar{t}(x)$, $\mathcal{R}_i^e$ is the effective retardation factor of the ith species, and M_i is the total mass of species i defined by

$$M_i(t) = \int_{-\infty}^{\infty} \mathcal{R}_i\, \phi\, C_i(\mathbf{x}, t)\, d\mathbf{x}. \tag{D.3}$$

The additivity property of risk states that the total ILCR for a system composed of n_s toxic chemical species is

$$\mathrm{R_T}(x) = \sum_{i=1}^{n_s} \mathrm{R}_i(x). \tag{D.4}$$

The human health risk model (section 3.2.1) relates the ILCR of a given species i to the maximum running averaged flux-concentration $\bar{c}_i$ and the toxicological parameters. For the sake of simplicity, one can simply express that

$$\mathrm{R}_i(x) = \beta_i\, \bar{c}_i(x), \tag{D.5}$$

where

$$\beta_i = CPF_i \times \left[\frac{IR}{BW}\right] \frac{ED \times EF}{AT} \tag{D.6}$$

Substituting (D.2) and (D.5) into (D.4) we obtain

$$\mathrm{R_T}(x) = \frac{\alpha}{Q_d\, ED} \sum_{i=1}^{n_s} \beta_i M_i \left(\frac{d(x)}{v_a} \mathcal{R}_i^e\right). \tag{D.7}$$

The critical distance x_c at which the total increased lifetime cancer risk reaches a maximum level is

$$x_c = \arg\max_x \{\mathrm{R_T}(x)\}, \tag{D.8}$$

which can be obtained by setting $\partial R_T/\partial x = 0$,

$$\frac{\partial}{\partial x} \sum_{i=1}^{n_s} \beta_i M_i \left(\frac{d(x)}{v_a} \mathcal{R}_i^e\right) = 0. \tag{D.9}$$

Defining $\bar{t} = d(x)/v_a$, this equation can be rewritten as

$$\frac{\partial}{\partial \bar{t}} \sum_{i=1}^{n_s} \beta_i M_i \left(\bar{t} \mathcal{R}_i^e\right) = 0. \tag{D.10}$$

Knowing $M_i(t)$, the solution of this implicit equation yields the critical time $\bar{t}_c$ needed for a conservative tracer to reach the critical risk distance. Thus,

$$\bar{t}_c = \arg\max_{\bar{t}} \left\{ \sum_{i=1}^{n_s} \beta_i M_i \left(\bar{t} \mathcal{R}_i^e\right) \right\}. \tag{D.11}$$

The temporal evolution of the total mass of a given species i can be determined from the mass balance equations of the chemical system, written as

$$\frac{dM_i(t)}{dt} = \frac{y_i k_{i-1}}{\mathcal{R}_{i-1}} M_{i-1}(t) - \frac{k_i}{\mathcal{R}_i} M_i(t) + m_0 \delta(t) \delta_{i1}, \ \forall i = 1, \ldots, n_s, \tag{D.12}$$

where δ_{i1} is the Kronecker delta (only PCE is released from the source zone). This is a system of ordinary differential equations whose solution is

$$\mathbf{M}(t) = m_0 e^{\mathbf{A}(t)} \mathbf{e}_1, \tag{D.13}$$

where $\mathbf{M}(t) = [M_1(t), ..., M_n(t)]^t$, $\mathbf{e}_1 = [1, 0, ..., 0]^t$, and $\mathbf{A}$ is a lower triangular matrix with diagonal elements determined by $A_{ii} = -k_i/\mathcal{R}_i$ and non-zero satellite elements determined by $A_{ii-1} = y_i k_{i-1}/\mathcal{R}_{i-1}$. This matrix $\mathbf{A}$ can be easily decomposed by the eigenvalue method into $\mathbf{A} = \mathbf{S}\mathbf{D}\mathbf{S}^{-1}$, where $\mathbf{D}$ is a diagonal matrix formed from the eigenvalues of $\mathbf{A}$, and the columns of $\mathbf{S}$ are the corresponding eigenvectors of $\mathbf{A}$. In a similar problem, Clement [2001] and Henri and Fernàndez-Garcia [2014] showed that these matrices can be written as

$$D_{ii} = -k_i/\mathcal{R}_i,$$

$$S_{ij} = S_{ij}^{-1} = 0, \qquad j > i,$$

$$S_{ij} = S_{ij}^{-1} = 1, \qquad j = i,$$

$$S_{ij} = \mathcal{R}_i \mathcal{R}_j^{i-j-1} \prod_{m=j}^{i-1} \left(\frac{k_m y_{m+1}}{\mathcal{R}_j k_{m+1} - \mathcal{R}_{m+1} k_j} \right),$$

$$S_{ij}^{-1} = \mathcal{R}_i^{i-j} \prod_{m=j}^{i-1} \left(\frac{-k_m y_{m+1}}{\mathcal{R}_m k_i - \mathcal{R}_i k_m} \right).$$

From this, the mass evolution of each species is written as

$$M_i(t) = m_0 \sum_{j=1}^{n_s} S_{ij} e^{D_{jj} t} S_{j1}^{-1}. \tag{D.14}$$

so that the critical time $\bar{t}_c$ is

$$\bar{t}_c = \arg\max_{\bar{t}} \left\{ \sum_{i=1}^{n_s} \sum_{j=1}^{n_s} \beta_i S_{ij} e^{-k_j \bar{t} \mathcal{R}_i^e / \mathcal{R}_j} S_{j1}^{-1} \right\}. \tag{D.15}$$

Assuming that the chemical properties are spatially constant, Henri and Fernàndez-Garcia [2014] has recently shown that the effective retardation factor associated with a network reaction system are time-dependent properties that depend on the initial conditions of the chemical system. When only PCE is initially present in the aquifer, the effective retardation factors can be estimated from

$$\mathcal{R}_i^e(t) = \frac{M_i(t)}{m_0} \left(\sum_{p,q,r=1}^{n_s} S_{ip} S_{pq}^{-1} \mathcal{R}_q^{-1} S_{qr} S_{r1}^{-1} F_{pr}(t) \right)^{-1}, \tag{D.16}$$

where

$$F_{pr}(t) = \begin{cases} \dfrac{\exp(-k_p/\mathcal{R}_p t) - \exp(-k_r/\mathcal{R}_r t)}{t\,(-k_p/\mathcal{R}_p + k_r/\mathcal{R}_r)}, & \text{if } p \neq r \\ \\ \exp(-k_r/\mathcal{R}_r t), & \text{if } p = r \end{cases} \tag{D.17}$$

We refer to Henri and Fernàndez-Garcia [2014] for further details on the effective retardation factor.

APPENDIX E

RW3D_RX: A THREE-DIMENSIONAL OBJECT-ORIENTED REACTIVE-TRANSPORT MODEL USING RANDOM-WALK PARTICLE-TRACKING

All numerical simulation of solute reactive transport presented in the thesis make use of the capacities of the code RW3D. Initially developed a decade ago by Daniel Fernàndez-Garcia during his stay at the the Colorado School of Mines (USA), RW3D has evolved through the years to solve a larger and larger range of reactive transport problem. RW3D's algorithms are written in FORTRAN 90/95 and follow an object-oriented philosophy making the code evolution easier. The following flow-chart diagram display summarily the program architecture.

RW3D consists mainly on the motion of particles with specific mass and evolving chemical state whom the ensemble simulates a plume evolution. The program is capable of simulating motion by advection, diffusion and dispersion, and reaction following a linear sorption, a range of mass transfer processes (single rate, multiple-rate, diffusion from spheres, layers or cylinders ...), or a first-order decay networks (serial and generic). Each of the simulated processes can be considered separately as well as following whatever

pre-defined combinations. Simpler scenarios are solved using analytical solutions increasing significantly the efficiency of the program. Most importantly, all motion or reaction parameters can be defined as spatially heterogeneous (at steady-state).

The motion of particles is controlled by a hybrid scheme for the velocity interpolation that has the advantage to provide divergence-free velocity fields within the solution domain and a velocity dependent dispersion tensor that approximates mass balance at grid interfaces of adjacent cells with contrasting hydraulic conductivity. More, the particles motion is randomized in order to respect classical random-walk theories for dispersion/diffusion modeling.

If necessary, you will find the input parameters description following the program flowchart.

FLOWCHART OF RW3D

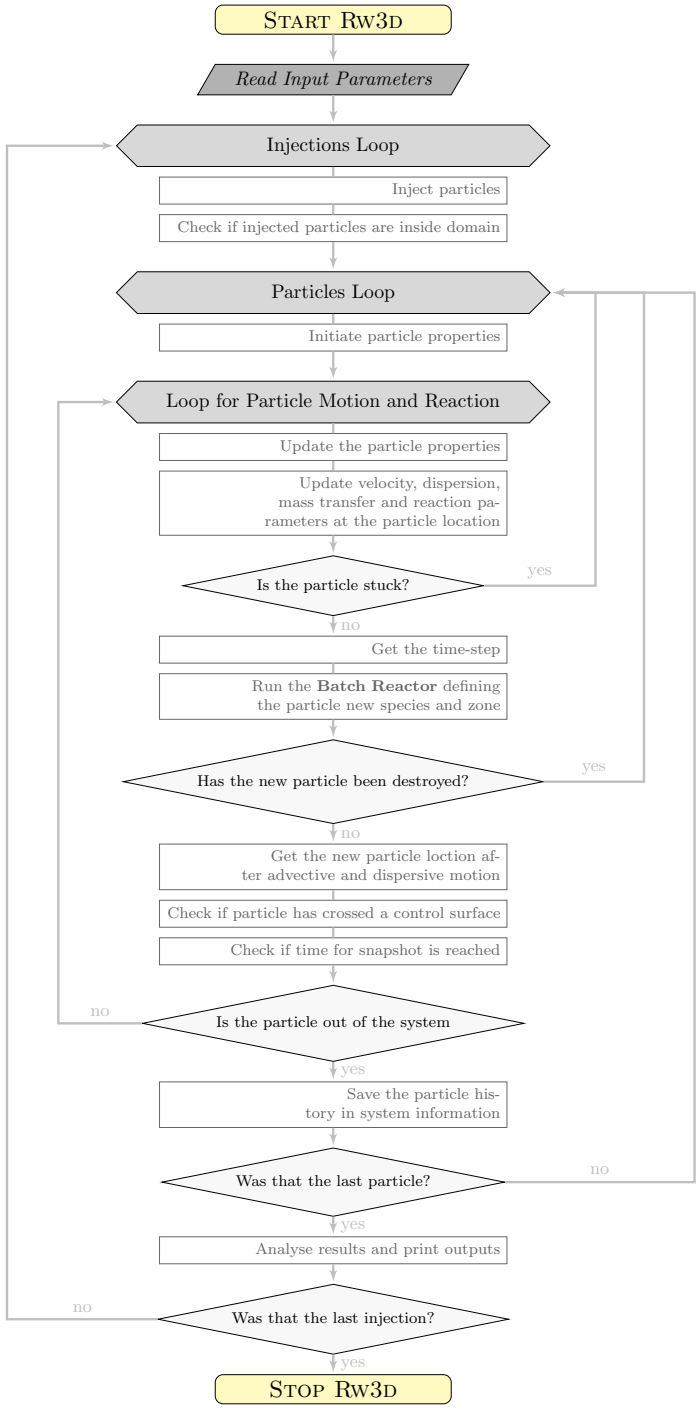

ReadMe: INPUT FILE FOR RW3D-Rx

Main program references

Fernàndez-Garcia, D., Illangasekare, T. H., and Rajaram, H. (2005), Differences in the scale-dependence of dispersivity estimated from temporal and spatial moments in physically and chemically heterogeneous porous media, *Advances in Water Resources* (ISSN 0309-1708), 28, 745-759. link

Salamon, P., Fernàndez-Garcia, D., and J. J. Gómez-Hernández (2006), A review and numerical assessment of the random walk particle tracking method, *Journal of Contaminant Hydrology* (ISSN 01697722), 86, 277-305. link

Salamon, P., Fernàndez-Garcia, D., and J. J. Gómez-Hernández (2006), Modeling mass transfer processes using random walk particle tracking, *Water Resour. Res.* (ISSN 0043-1397), 42, W11417, doi:10.1029/2006WR004927. link

Henri, C.V., and Fernàndez-Garcia, D. (2014), Toward efficiency in heterogeneous multispecies reactive transport modeling: A particle-tracking solution for first-order network reactions, *Water Resour. Res.*, 50, 72067230, doi:10.1002/2013WR014956. link

Field applications

Salamon, P., Fernàndez-Garcia, D., J. J. Gómez-Hernández (2007), Modeling tracer transport at the MADE site: The importance of heterogeneity, *Water Resour. Res.* (ISSN 0043-1397), 43, W08404, doi:10.1029/2006WR005522. link

Riva, M., A. Guadagnini, D. Fernàndez-Garcia, X. Sánchez-Vila, (2008), Relative importance of geostatistical and transport models in describing heavily tailed breakthrough curves at the Lauswiesen site, *Journal of Contaminant Hydrology* (ISSN 01697722), 101, 1-13, 2008. link

INPUT FILES

Name file	File with names for output files (by default: `rw3d.nam`)
Parameter file	File with parameters (to be defined in the name file)

NAME FILE

LINE	VARIABLE	DESCRIPTION
1	Text	
2	Text	
3	Text	
4	Text	
5	File name	Parameter file
6	Text	
7	Text	
8	Text	
9	File name	Output histogram (pdf) of particle arrival times (btcs)
10	File name	Output with cumulative pdf particle arrival times (cbtcs)
11	File name	Output with particle snapshots with time
12	File name	Output with particle paths
13	File name	Output with cartesian spatial moments
14	File name	Output with spatial moments of particle position
15	File name	Output with particle position at control planes
16	File name	Output with dilution index of kitanidis (option disable)
17	File name	Output with radial spatial moments
18	File name	Output with temporal moments of breakthrough curves
19	File name	Output with dispersivities from control planes breakthrus
20	File name	Output with residence times in zonal regions
21	File name	Output with velocity field (for idebug ≥ 1)
22	File name	Output with derivative of BTC in double log

PARAMETER FILE

DEBUG OPTIONS

LINE	VARIABLE	DESCRIPTION
1	Text	
2	Text	
3	Text	
4	idebug, ipReStart	*idebug*: Integer defining degree of debugging as written in `rw3d_general.dbg` OPTIONS: • idebug = -1 → Do not write the velocity field • idebug = 0 → Normal Run • idebug = 10 → Maximum Debugging Degree *ipReStart*: Particle number to start simulations. It is a restart options for those cases in which the program crashes before finalizing the task. The program writes all the particle info in temporary files in real time so that no information is lost when the program crashes.

GEOMETRY

LINE	VARIABLE	DESCRIPTION
5	Text	
6	Text	
7	Text	
8	nx, ny, nz	Number of cells in x,y,z directions

9	dx [*read as a real array*]	Size cells in x-direction
10	dy [*read as a real array*]	Size cells in y-direction
11	dz [*read as a real array*]	Size cells in z-direction
12	file, const, ivar, flag	*file*: file name with array defining inactive cells (IBOUND variable) *const*: after reading the array, all values are multiplied by *const* *ivar*: column variable in the GSLIB file *flag*: integer defining the way to read the array

OPTIONS:

- flag = 0: The array is not read from file.
- flag = 1: The array is read from file named FILE. This file has GSLIB format such that:

  IBOUND $\neq$ 0: active cell

  IBOUND = 0: inactive cell $\rightarrow$ particles reflect at cell boundaries
- flag = 2: Option specific for reading IBOUND from MODFLOW external file format.
- flag = 3: Specific for IBOUND array. This reads specific inactive cells from the external file named *file*. The format of this external file is:

1. number of inactive cells [Integer]

for each inactive cell:

2. column, row, layer (in GSLIB format)

13	ibx1, ibx2, iby1, iby2, ibz1, ibz2	Boundary conditions: ib = 0 for flux boundary condition ib = 1 for impermeable boundary condition

TIME DISCRETIZATION

LINE	VARIABLE	DESCRIPTION
14	Text	
15	Text	
16	Text	
17	string	Method to calculate the time step

OPTIONS:

- string = CONSTANT_DT: The time step is fixed: standard random walk
- string = CONSTANT_CU: The time step is estimated from

$$\Delta \mathrm{t} = \mathrm{Cu}\ \frac{\Delta s}{\|v\|/R},$$

where Δs is the characteristic size of a cell, Cu is the grid-courant number (given in the next line), and R is the retardation coefficient.

- string = CONSTANT_PE: The time step is estimated from

$$\Delta \mathrm{t} = \mathrm{Pe}\ \min \frac{\Delta x_i^2}{D}\ R,$$

where Pe is the grid-peclet number (given in next line), and D is the hydrodynamic dispersion coefficient.

- string = CONSTANT_DaMT: The time step is estimated from

$$\Delta \mathrm{t} = \mathrm{DaMT}\ /\ t_{\mathrm{MT}}$$

where DaMT is the grid-Damkholer number based on Mass Transfer process (given in next line), and t_{MT} is the characteristic time for mass transfer, i.e.:

$$t_{\mathrm{MT}} = \max \frac{1}{\alpha_k \times \beta_k} \quad \forall k = 1, \ldots, N_{im},$$

where α_k and β_k are respectively the mass transfer coefficient and the field capacity coefficient associated to the kth immobile domain, and N_{im} is the number of immobile zones.

- string = CONSTANT_DaSORP: The time step is estimated from

$$\Delta t = \text{DaSORP} \;/\; \max\{k_f, k_b\},$$

where DaSORP is the grid-Damkholer number based on Sorption process (given in next line) modeled using the Continuous History Time Method, and k_f and k_b are respectively the forward and backward rates.

- string = CONSTANT_DaDECAY: The time step is estimated from

$$\Delta t = \text{DaDECAY} \;/\; t_K,$$

where DaDECAY is the grid-Damkholer number based on Decay process (given in next line), and t_K is the characteristic time for first-order decay, i.e. $t_K = \dfrac{R}{k}$ where k is the first-order decay rate.

- string = CONSTANT_PE_OR_CU: Chooses the more restrictive of the times estimated from Peclet and Courant numbers.

- string = CONSTANT_CU_OR_DA: Chooses the more restrictive of the times estimated from Courant and Damkholer numbers.

- string = CONSTANT_CU_OR_PE_OR_DA: Chooses the more restrictive of the times estimated from Courant, Pecelt and Damkholer numbers.

- string = CONSTANT_MOVE_X_CELL: Estimates the time step only once for each cell as

$$\Delta t = \text{Cu}\; T_{esc},$$

where T_{esc} is the advective travel time of the particle in the cell.

18	Dt, Cu, Pe, DaMT DaSORP, DaDECAY	Dt → time step Cu → grid-Courant number Pe → grid-Pecklet number DaMT → grid-Damkholer number based on Mass Transfer process DaSORP → grid-Damkholer number based on Sorption process DaDECAY → grid-Damkholer number based on Decay process

ADVECTION PACKAGE

LINE	VARIABLE	DESCRIPTION
19	Text	
20	Text	
21	Text	
22	Logical Flag	True (T) if package is active
23	method	Character variable specifying computation of the advection displacement of a particle.

OPTIONS:

- method = EULERIAN: Standard Random Walk with Eulerian integration of the velocity:

$$\Delta \mathbf{X}_{p,adv} = \int v(\tau) d\tau \approx v(\mathbf{X}_p, t)\Delta t,$$

where $\mathbf{X}_{p,adv}$ is the advective motion of a particle, and v is the pore velocity.

- method = EXPONENTIAL: Pollock Method to integrate the velocity from finite-difference flow models:

$$\Delta \mathbf{X}_{p,adv} = \int v(\tau) d\tau \approx \frac{v_i(\mathbf{X}_p, t)}{A_i\, R}(\exp(A_i\, \Delta t) - 1), \text{ with}$$

$$A_i = \frac{v_{i,face(2)} - v_{i,face(1)}}{\Delta x_i}.$$

24	qx [*read as a real array*]	Darcy velocity in x
25	qy [*read as a real array*]	Darcy velocity in y
26	qz [*read as a real array*]	Darcy velocity in z
27	poro [*read as a real array*]	Porosity for the Mobile Zone

DISPERSION PACKAGE

LINE	VARIABLE	DESCRIPTION
28	Text	
29	Text	
30	Text	
31	Logical Flag	True (T) if package is active
32	aL [*read as a real array*]	Longitudinal dispersivity
33	aTH [*read as a real array*]	Transverse dispersivity in horizontal plane
34	aTV [*read as a real array*]	Transverse dispersivity in vertical plane
35	Dm [*read as a real array*]	Molecular diffusion

MASS TRANSFER PACKAGE

LINE	VARIABLE	DESCRIPTION
36	Text	
37	Text	
38	Text	
39	Logical Flag	True (T) if package is active
40	Model	Type of mass transfer model

OPTIONS:

- model = MULTIRATE: discrete series of mass transfer rates

How to define input parameters?

41	N_{im}	number of immobile zones

for each zone:

42	$\phi_{k=1}$ [*read as a real array*]	porosity in the 1^{st} immobile zone

43	$\alpha'_{k=1}$ [*read as a real array*]	first-order mass transfer rate associated with the 1^{st} immobile zone
	ϕ_k [*read as a real array*]	porosity in the kth immobile zone
⋮	α'_k [*read as a real array*]	first-order mass transfer rate associated with the kth immobile zone

- model = SPHERICAL_DIFFUSION or LAYERED_DIFFUSION or CYLINDRICAL_DIFFUSION: diffusion geometry

How to define input parameters?

41	N_{im}	number of immobile zones
42	ϕ_{im} [*read as a real array*]	porosity in the immobile domain
43	D_p/a^2 [*read as a real array*]	effective pore diffusion coefficient, related to apparent pore diffusion coefficient D_a/a^2 by $D_a = D_p/R_{im}$. D_p $[L^2/T]$ is the diffusivity coefficient, a^2 $[L^2]$ is the radius of the blocks. The multirate series for diffusion models is given in Table E.1.

- model = POWER_LAW: power law memory function

How to define input parameters?

41	N_{im}	number of immobile zones
42	β_{tot} [*read as a real array*]	total capacity ratio of all immobile zones
43	A_{min} [*read as a real array*]	minimum apparent mass transfer coefficient
44	A_{max} [*read as a real array*]	maximum apparent mass transfer coefficient
45	*power* [*read as a real array*]	exponent of the power law density function of first-order rate coefficient

- model = LOGNORMAL_LAW: lognormal law memory function

How to define input parameters?

41	N_{im}	number of immobile zones
42	β_{tot} [*read as a real array*]	total capacity ratio of all immobile zones

43	*mean* [*read as a real array*]	mean of the natural log of mass transfer coefficient
44	*stdv* [*read as a real array*]	standard deviation of the natural log of mass transfer coefficient

- model = COMPOSITE_MEDIA: mixture of geometries

How to define input parameters?

41	N_{mrate}, N_{sph}, N_{cyl}, N_{lay}	number of immobile zones for the multirate model (N_{mrate}), the spherical diff. model (N_{sph}), the cylindrical diff. model (N_{cyl}) and the cylindrical diff. model (N_{lay})

for each zone of each mass transfer model:

42	$Fmrate_1$	fraction of the 1^{st} zone for the multirate model
...	$Fmrate_k$	fraction of the kth zone for the multirate model
43	$Fsph_1$	fraction of the 1^{st} zone for the sph. diff. model
...	$Fsph_k$	fraction of the kth zone for the sph. diff. model
44	Fcy_1	fraction of the 1^{st} zone for the cyl. diff. model
...	Fcy_k	fraction of the kth zone for the cyl. diff. model
45	$Flay_1$	fraction of the 1^{st} zone for the lay. diff. model
...	$Flay_k$	fraction of the kth zone for the lay. diff. model

parameters for the multirate model:

46	$\phi_{k=1}$ [*read as a real array*]	porosity in the 1^{st} imm. zone
47	$\alpha'_{k=1}$ [*read as a real array*]	first-order mass transfer rate associated with the 1^{st} imm. zone
⋮	ϕ_k [*read as a real array*]	porosity in the k^{th} imm. zone
	α'_k [*read as a real array*]	first-order mass transfer rate associated with the k^{th} imm. zone

parameters for the sph. diff model:

48	ϕ_{im} [*read as a real array*]	porosity in the immobile domain
49	D_p/a^2 [*read as a real array*]	effective pore diffusion coefficient

parameters for the cyl. model:		
50	ϕ_{im} [*read as a real array*]	porosity in the immobile domain
51	D_p/a^2 [*read as a real array*]	effective pore diffusion coefficient
parameters for the lay. model:		
52	ϕ_{im} [*read as a real array*]	porosity in the immobile domain
53	D_p/a^2 [*read as a real array*]	effective pore diffusion coefficient

REACTION PACKAGE

LINE	VARIABLE	DESCRIPTION
44	Text	
45	Text	
46	Text	
47	Logical Flag	True (T) if package is active
48	N_s	Number of species
sorption		
49	Text	
50	Text	
51	Text	
52	Logical Flag	True (T) if package is active
53	model	Type of sorption

OPTIONS:

- model = LINEAR: instantaneous linear sorption isotherm

for each species:

54	$R_{i=1}$ [*read as a real array*]	retardation coefficient for the 1^{st} species
...	R_i [*read as a real array*]	retardation coefficient for the i^{th} species

IF MASS TRANSFER:

mass transfer type = MULTIRATE

for each species, for each zone:

55	$Rim_{i=1,k=1}$ [*read as a real array*]	retardation for the 1^{st} species in the 1^{st} immobile zone
...	$Rim_{i=1,k}$ [*read as a real array*]	retardation for the 1^{st} species in the kth immobile zone
56	$Rim_{i,k=1}$ [*read as a real array*]	retardation for the ith species in the 1^{st} immobile zone
...	$Rim_{i,k}$ [*read as a real array*]	retardation for the ith species in the kth immobile zone

mass transfer type = _DIFFUSION or POWER_LAW or LOGNORMAL_LAW:

for each species:

57	$Rim_{i=1}$ [*read as a real array*]	retardation for the 1^{st} species in the immobile domain
...	Rim_i [*read as a real array*]	retardation for the ith species in the immobile domain

- model = CHTM: linear sorption solved by Contineous History Time Method

only available for a single species and no mass transfer

54	*bd* [*read as a real array*]	bulk density
55	*kf* [*read as a real array*]	forward mass transfer coefficient
56	*kb* [*read as a real array*]	backward mass transfer coefficient

TABLE E.1: Multirate series for diffusion (after Haggerty and Gorelick [1995])

Diffusion geometry	Multirate series[a] for j=1,...,N_{im}-1		Multirate series[a] for j=N_{im}	
	α_j	β_j	α_j	β_j
Layered diffusion	$\frac{(2j-1)^2\pi^2}{4}(D_a/a^2)_i$	$\frac{8}{(2j-1)^2\pi^2}\beta_{tot}$	$\frac{3\left(D_a/a^2\right)_i\left[1-\sum_{j=1}^{N_{im}-1}\frac{8}{(2j-1)^2\pi^2}\right]}{1-\sum_{j=1}^{N_{im}-1}\frac{96}{(2j-1)^4\pi^4}}$	$\left[1-\sum_{j=1}^{N_{im}-1}\frac{8}{(2j-1)^2\pi^2}\right]\beta_{tot}$
Cylindrical diffusion[a]	$r_{0,j}^2(D_a/a^2)_i$	$\frac{4}{r_{0,j}^2}\beta_{tot}$	$\frac{8\left(D_a/a^2\right)_i\left[1-\sum_{j=1}^{N_{im}-1}\frac{4}{r_{0,j}^2}\right]}{1-\sum_{j=1}^{N_{im}-1}\frac{32}{r_{0,j}^2}}$	$\left[1-\sum_{j=1}^{N_{im}-1}\frac{4}{r_{0,j}^2}\right]\beta_{tot}$
Spherical diffusion[b]	$j^2\pi^2(D_a/a^2)_i$	$\frac{6}{j^2\pi^2}\beta_{tot}$	$\frac{15\left(D_a/a^2\right)_i\left[1-\sum_{j=1}^{N_{im}-1}\frac{6}{j^2\pi^2}\right]}{1-\sum_{j=1}^{N_{im}-1}\frac{90}{j^4\pi^4}}$	$\left[1-\sum_{j=1}^{N_{im}-1}\frac{6}{j^2\pi^2}\right]\beta_{tot}$

[a] Where $r_{0,j}$ is the jth root of $J_0(x)$ where J_0 is the zero-order Bessel function of the first kind.

[b] Where $(\beta_{tot})_i = \frac{\phi_{im}\,R_i^{im}}{\phi_m\,R_i^m}$ is the capacity ratio for a specie i.

first-order network reaction .....

55	Text	
56	Text	
57	Text	
58	Logical Flag	True (T) if package is active
59	model	Type of network reaction

OPTIONS:

- model = SERIAL: for a serial reaction network: A $\rightarrow$ B $\rightarrow$ C $\rightarrow$ ...
- model = SERIAL_MOMENT: for a serial reaction network with motion solved by calculating the first and second spacial moments
- model = GENERIC: for a generic network reaction

for each species:

60	$k_{i=1}$ [*read as a real array*]	first-order decay rate for the 1^{st} species
...	k_i [*read as a real array*]	first-order decay rate for the i^{th} species
61	$y_{i=1}$ [*read as a real array*]	yield coefficient for the 1^{st} species
...	y_i [*read as a real array*]	yield coefficient for the i^{th} species

IF MASS TRANSFER:

mass transfer type = MULTIRATE

for each species, for each zone:

62	$kim_{i=1,k=1}$ [*read as a real array*]	first-order decay rate for the 1^{st} species in the 1^{st} immobile zone
...	$kim_{i=1,k}$ [*read as a real array*]	first-order decay rate for the 1^{st} species in the k^{th} immobile zone
63	$kim_{i,k=1}$ [*read as a real array*]	first-order decay rate for the i^{th} species in the 1^{st} immobile zone
...	$kim_{i,k}$ [*read as a real array*]	first-order decay rate for the i^{th} species in the k^{th} immobile zone

mass transfer type = _DIFFUSION or POWER_LAW or LOGNORMAL_LAW:		
for each species:		
64	$kim_{i=1}$ [*read as a real array*]	first-order decay rate for the 1^{st} species in the immobile domain
...	kim_i [*read as a real array*]	first-order decay rate for the i^{th} species in the immobile domain

CONTROL SURFACES PACKAGE

LINE	VARIABLE	DESCRIPTION
62	Text	
63	Text	
64	Text	
65	Logical Flag	True (T) if package is active
66	N_{well}	Number of wells
for each well:		
67	Xwell, Ywell, Rwell, Zbot, Ztop, Flag, NPa	*Xwell, Ywell*: X, Y well coordinates *Rwell*: well radius *Zbot*: well bottom (z coordinate) *Ztop*: well top (z coordinate) *Flag*: integer defining particle behavior after passing thru the well OPTIONS: • flag = 0 → The particle passes thru the well but does not exit the system • flag = 1 → The particle exits the system when crosses the well *NPa*: Expected number of particles arriving at the well (only a rough approximation is needed)

66 N_{plane} Number of control plane

for each plane:

OPTIONS:

- For planes perpendicular or parallel to axes

67 Dist, Type, NPa, Flag

Dist: Distance of the control plane with respect to the x,y coordinate axis

Type: type of plane which can be:

- type = XX → plane parallel to the x coordinate
- type = YY → plane parallel to the y coordinate

NPa: Expected number of particles arriving at the well (only a rough approximation is needed)

Flag: Integer that can be:

- flag = 0 → The particle passes thru the well but does not exit the system
- flag = 1 → The particle exits the system when crosses the well

67 A, B, C, D, NPa, Flag

NPa: Expected number of particles arriving at the well (only a rough approximation is needed)

- For planes oriented in any direction. The plane is described by the equation of a plane:

$$Ax + By + Cz + D = 0$$

Flag: Integer that can be:

- flag = 0 → The particle passes thru the well but does not exit the system
- flag = 1 → The particle exits the system when crosses the well

INJECTIONS OF PARTICLES

LINE	VARIABLE	DESCRIPTION
68	Text	
69	Text	
70	Text	
71	N_{inj}	Number of injections
71	N_{inj}	NOTE: This version considers the injections to be independent from one another.

for each injection:

72	Type (string)	Type of injections

OPTIONS:

- type = POINT

point injection → all particles start the simulation from the same point position.

73	Np, Totmass, Zone, Specie	*Np*: Number of particles *Totmass*: total mass injected *Zone*: Zone which the particles belongs initially (0 = mobile) *Specie*: Specie which the particles belongs initially
74	xinj, yinj, zinj	x, y, z point coordinates

- type = LINE

vertical line injection → particles randomly uniformly distributed in a vertical line.

73	Np, Totmass, Zone, Specie	*see point injection*
74	xinj, yinj, zbot, ztop	*xinj, yinj*: x, y coordinates vertical line *zbot*: z line bottom vertical position *ztop*: z line top vertical position

- type = BLOCK

block injection → particles uniformly distributed, equidistantly, in a block defined by lower grid-cel upper grid-cell index.

73	Np, Totmass, Zone, Specie	*see point injection*
74	idwn, jdwn, kdwn, iup, jup, kup, np11x, np11y, np11z	*idwn, jdwn, kdwn*: lower left cell number in x, y, z direction *iup, jup, kup*: top right cell number in x, y, z direction *np11x, np11y, np11z*: Number of particles per unit length in each cell of the block for the three main directions NOTE: Np has to be equal to $np11x \times dx + np11y \times dy + np11z \times dz$

- type = CIRCLE

circle injection → particles uniformly distributed (randomly) within a vertical cylinder.

73	Np, Totmass, Zone, Specie	*see point injection*
74	x0, y0, zbot, ztop, rcy	*x0, y0*: coordinates origin cylinder *zbot*: z bottom position cylinder *ztop*: z top position cylinder *rcy*: cylinder radius

- type = RADIAL

radial injection → particles uniformly distributed (randomly) on the surface of a vertical cylinder.

73	Np, Totmass, Zone, Specie	*see point injection*
74	xinj, yinj, zbot, ztop, rcp	*xinj, yinj*: coordinates origin cylinder *zbot*: z bottom position cylinder *ztop*: z top position cylinder *rcp*: cylinder radius

- type = PLANE

plane injection → particles uniformly distributed in a vertical plane perpendicular to x direction (not random, equidistant points).

73	Np, Totmass, Zone, Specie	*see point injection*
74	xdist, width, height	*xdist*: x position of the vertical plane *width*: width of the plane in the y direction *height*: height of the plane in the z direction

- type = PLANE_RANDOM

plane injection random → particles uniformly distributed (randomly) in a vertical plane perpendicula

73	Np, Totmass, Zone, Specie	*see point injection*
74	xdist, width, height	*see plane injection*

- type = LINE_BY_POINTS

line injection by points → particles distributed uniformly (not random) in a line specified by points.

73	Np, Totmass, Zone, Specie	*see point injection*
74	x1, y1, z1, x2, y2, z2	*x1, y1, z1*: x,y,z coordinates of the first point *x2, y2, z2*: x,y,z coordinates of the second point

- type = LINE_FLUX_WEIGHTED

line flux weighted → particles are distributed proportional to the darcy velocity.

73	Np, Totmass, Zone, Specie	*see point injection*
74	x1, y1, z1, x2, y2, z2	*see line injection*

- type = READ_FROM_FILE

read from external file.

The format of the external file is:
1 LINE: Heading
2 LINE: Number of particles
3 LINE: For each particle: x, y, z, mass_particle , zone, specie

POST-PROCESSING AND OUTPUT OPTIONS

LINE	VARIABLE	DESCRIPTION
75	Text	
76	Text	
77	Text	
	plume snapshots parameters	
78	Text	
79	Flag, File, Tlen, Ntstep, Tmult	*Flag*: Integer that can be: • flag = 0 → Inactive • flag = 1 → Reading from file *File*: Filename with specific times to take snapshots The format of the file is: 1. Line: Heading 2. Number of times 3. Vertical column with times *Tlen* (used if Flag = 0): Total elapsed time *Ntstep* (used if Flag = 0): Total number of shots *Tmult* (used if Flag = 0): Multiplier → time shots are calculated as $dt(i+1) = Tmult \times dt(i)$
80	Flag	*Flag*: print Cartesian Spatial Moments at Snapshots
81	Flag, Xr0, Yr0	*Flag*: print Radial Spatial Moments at Snapshots *Xr0*: X-position of the origin of coordinates *Yr0*: Y-position of the origin of coordinates
82	Flag	*Flag*: print Particle Cloud at Snapshot

breakthru curve parameters .....

83	Text	
84	Flag	*Flag*: print temporal moments of BTCs
85	Flag	*Flag*: print moments of particle positions at planes
86	Flag	*Flag*: print particle position at planes
87	Flag	*Flag*: print apparent dispersivity at planes
88	Flag, ngrid, method, bw, min	*Flag*: print BTCs *ngrid*: size of the grid used for pdf reconstruction *method*: options → BOX, TRIANGLE, GAUSS, PLUGING NOTE: The method PLUGIN optimizes the bandwidth with an iterative algorithm that minimizes the mean integrated squared error of the density function. In this case the resulting bandwidth is the standard deviation of the Gaussian density function. For most conditions works quite well. *bw*: half bandwidth support for histogram evaluation • bw $< 0 \rightarrow$ bw estimated by the program *min*: minimum value of the histogram bin • min $< 0 \rightarrow$ min estimated by the program *max*: maximum value of the histogram bin • max $< 0 \rightarrow$ max estimated by the program
89	Flag, Freq., Particle	*Flag*: print path *Freq.*: Frequency of printing particles = moves/prints *Particle*: Number of particle to print. If < 0 all particles are printed

AUXILIARY INFORMATION

How does the program read real arrays?

OPTIONS:

- flag = 0: The array is not read from file. Instead the variable is regard as a constant with a value equal to CONST.
- flag = 1: The array is read from file named FILE. This file has GSLIB format such that:

  IVAR = column variable in the GSLIB file

  CONST = after reading the array, all values are multiplied by CONST
- flag = 2: Option specific for reading Darcy velocities from MODFLOW. When this option is specified in line for qx, then the program reads the output binary file from MODFLOW with cell-to-cell budget.

Definition of the origin of coordinates

The origin of coordinates is the left-bottom corner so that:

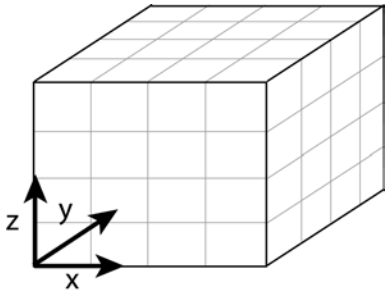

How do we read real arrays?

The Fortran subroutine that reads the input real array follows the algorithm:

for $k = 1$ **to** nz **do**
  for $j = 1$ **to** ny **do**
    for $i = 1$ **to** nx **do**
      read the input values at (i,j,k) ;
      parameter at (i,j,k) = read values × CONST
    end
  end
end

Bibliography

L. M. Abriola and G. F. Pinder. A multiphase approach to the modeling of porous media contamination by organic compounds: 1. Equation Development. *Water Resour. Res.*, 21(1), 1985. doi: 10.1029/WR021i001p00011. URL dx.doi.org/10.1029/WR021i001p00011.

N.R. Adrian, J.A. Robinson, and J.M. Suflita. Spatial Variability in Biodegradation Rates as Evidenced by Methane Production from an Aquifer Spatial Variability in Biodegradation Rates as Evidenced by Methane Production from an Aquifer. *Applied and environmental microbiology*, 60(10), 1994.

R. M. Allen-King, D. P. Divine, M. J. L. Robin, J. R. Alldredge, and D. R. Gaylord. Spatial distributions of perchloroethylene reactive transport parameters in the Borden Aquifer. *Water Resour. Res.*, 42(1):W01413, 2006. doi: 10.1029/2005WR003977. URL http://dx.doi.org/10.1029/2005WR003977.

E. Anderson, Z. Bai, C. Bischof, S. Blackford, J. Demmel, J. Dongarra, J. Du Croz, A. Greenbaum, S. Hammarling, A. McKenney, and D. Sorensen. LAPACK. Users' Guide Third Ed., Society for Industrial and Applied Mathematics, 1999.

M. R. Anderson, R. L. Johnson, and J. F. Pankow. Dissolution of dense chlorinated solvents into groundwater. 3. Modeling contaminant plumes from fingers and pools of

solvent. *Environ. Sci. Technol.*, 26(5), 1992. doi: 10.1021/es00029a005. URL dx.doi.org/10.1021/es00029a005.

R. Andričević and V. Cvetković. Evaluation of Risk from Contaminants Migrating by Groundwater. *Water Resour. Res.*, 32(3), 1996. doi: 10.1029/95WR03530. URL dx.doi.org/10.1029/95WR03530.

R. Andričević and E. Foufoula-Georgiou. Modeling kinetic non-equilibrium using the first two moments of residence time distribution. *Stochastic Hydrol. Hydraul.*, 5:155–171, 1991.

R. Andričević, V. Srzic, and H. Gotovac. Risk characterization for toxic chemicals transported in aquifers. *Advances in Water Resources*, 36, 2012.

A. L. Atchley, R. M. Maxwell, and A. K. Navarre-Sitchler. Human Health Risk Assessment of CO_2 Leakage into Overlying Aquifers Using a Stochastic, Geochemical Reactive Transport Approach. *Environ. Sci. Technol.*, 47(11), 2013. doi: 10.1021/es400316c. URL dx.doi.org/10.1021/es400316c.

A. L. Atchley, R. M. Maxwell, and A. K. Navarre-Sitchler. Using streamlines to simulate stochastic reactive transport in heterogeneous aquifers: Kinetic metal release and transport in {CO2} impacted drinking water aquifers. *Adv. Water Resour.*, 52, 2014.

A. Bagtzoglou, A. F. B. Tompson, and D. E. Dougherty. Spatial distributions of perchloroethylene reactive transport parameters in the Borden Aquifer. *Numer. Methods Partial Differential Equations*, 8:325–340, 1992.

P. Baveye and A. Valocchi. An evaluation of mathematical models of the transport of biologically reacting solutes in saturated soils and aquifers. *Water Resour. Res.*, 25(6), 1989.

A. Bellin and D. Tonina. Probability density function of non-reactive solute concentration in heterogeneous porous formations. *Journal of contaminant hydrology*, 94(1), 2007.

A. Bellin, Y. Rubin, and A. Rinaldo. Eulerian-Lagrangian approach for modeling of flow and transport in heterogeneous geological formations. *Water Resour. Res.*, 31(11), 1994.

I. D. Benekos, C. A. Shoemaker, and J. R. Stedinger. Probabilistic risk and uncertainty analysis for bioremediation of four chlorinated ethenes in groundwater. *Stochastic Environmental Research and Risk Assessment*, 21(4):375–390, 2006. doi: 10.1007/s00477-006-0071-4. URL http://dx.doi.org/10.1007/s00477-006-0071-4.

D. A. Benson and M. M. Meerschaert. Simulation of chemical reaction via particle tracking: Diffusion-limited versus thermodynamic rate-limited regimes. *Water Resour. Res.*, 44(12), 2008a. doi: 10.1029/2008WR007111. URL dx.doi.org/10.1029/2008WR007111.

D. A. Benson and M. M. Meerschaert. Simulation of chemical reaction via particle tracking: Diffusion-limited versus thermodynamic rate-limited regimes. *Water Resour. Res.*, 44(7):W12201, 2008b. doi: 10.1029/2008WR007111. URL http://dx.doi.org/10.1029/2008WR007111.

D. A. Benson and M. M. Meerschaert. A simple and efficient random walk solution of multi-rate mobile/immobile mass transport equations. *Adv. Water Resour.*, 32:532–539, 2009. doi: 10.1016/j.advwatres.2009.01.002. URL http://dx.doi.org/10.1016/j.advwatres.2009.01.002.

B. Berkowitz, A. Cortis, M. Dentz, and H. Scher. Modeling non-Fickian transport in geological formations as a continuous time random walk. *Rev. Geophys.*, 44:RG2003, 2006. doi: 10.1029/2005RG000178. URL http://dx.doi.org/10.1029/2005RG000178.

M. Bianchi, C. Zheng, C. Wilson, G. R. Tick, G. Liu, and S. M. Gorelick. Spatial connectivity in a highly heterogeneous aquifer: From cores to preferential flow paths. *Water Resour. Res.*, 47(5), 2011. doi: 10.1029/2009WR008966. URL dx.doi.org/10.1029/2009WR008966.

D. Bolster, M. Barahona, M. Dentz, D. Fernàndez-Garcia, X. Sanchez-Vila, P. Trinchero, and et al. Probabilistic risk analysis of groundwater remediation strategies. *Water Resour. Res.*, 45:W06413, 2009. doi: 10.1029/2008WR007551. URL http://dx.doi.org/10.1029/2008WR007551.

F. Boso, A. Bellin, and M. Dumbser. Numerical simulations of solute transport in highly heterogeneous formations: A comparison of alternative numerical schemes. *Adv. Water*

Resour., 52:178–189, 2013. doi: 10.1016/j.advwatres.2012.08.006. URL http://dx.doi.org/10.1016/j.advwatres.2012.08.006.

E. J. Bouwer, B. E. Rittmann, and P. L. McCarty. Anaerobic degradation of halogenated 1- and 2-carbon organic compounds. *Environ. Sci. Technol.*, 15(5):596599, 1981.

M. Brusseau. The Impact of DNAPL Source-Zone Architecture on Contaminant Mass Flux and Plume Evolution in Heterogeneous Porous Media. Report SERDP project ER-1614, Department of Defense Strategic Environmental Research and Development Program, 2013.

M. Bundt, F. Widmer, M. Pesaro, J. Zeyer, and P. Blaser. Preferential flow paths: biological hot spots in soils. *Soil Biol. Biochem.*, 33, 2001.

D. K. Burnell, J. W. Mercer, and C. R. Faust. Stochastic modeling analysis of sequential first-order degradation reactions and non-Fickian transport in steady state plumes. *Water Resour. Res.*, 50:12601287, 2014. doi: 10.1002/2013WR013814. URL http://dx.doi.org/10.1002/2013WR013814.

J. Carrera, X. Sánchez-vila, I. Benet, A. Medina, G. Galarza, , and J. Guimer. On matrix diffusion : formulations, solution methods and qualitative effects. *Hydrogeology Journal*, 6(1), 1998.

F. Chapelle. *Groundwater microbiology and geochemistry*. Wiley, Hoboken, New Jersey, 2001. 477 pp.

J. A. Christ, L. D. Lemke, and L. M. Abriola. Comparison of two-dimensional and three-dimensional simulations of dense nonaqueous phase liquids (DNAPLs): Migration and entrapment in a nonuniform permeability field. *Water Resour. Res.*, 41, 2005. doi: 10.1029/2004WR003239. URL dx.doi.org/10.1029/2004WR003239.

J. A. Christ, C. A. Ramsburg, K. D. Ponnell, and L. M. Abriola. Predicting DNAPL mass discharge from pool-dominated source zones. *Journal of Contaminant Hydrology*, 114(1-4), 2010. doi: 10.1016/j.jconhyd.2010.02.005. URL dx.doi.org/10.1016/j.jconhyd.2010.02.005.

T. P. Clement. RT3D - A modular computer code for simulating reactive multispecies transport in 3-Dimensional groundwater systems. Version 1.0. Technical Report PNNL-SA-11720, Pacific Northwest National Laboratory, Richland, 1997.

T. P. Clement. Generalized solution to multispecies transport equations coupled with a first-order reaction network. *Water Resour. Res.*, 37:157–163, 2001.

R.M. Cohen and J.W. Mercer. *DNAPL Site Evaluation*. C.K. Smoley, CRC Press, Boca Raton, FL, 1993.

Z. Cui, C. Welty, and R. M. Maxwell. Modeling nitrogen transport and transformation in aquifers using a particle-tracking approach. *Computers & Geosciences*, 70:114, 2014. doi: 10.1016/j.cageo.2014.05.005. URL http://dx.doi.org/10.1016/j.cageo.2014.05.005.

J. A. Cunningham and Z. J. Fadel. Contaminant degradation in physically and chemically heterogeneous aquifers. *J. Cont. Hydrology*, 94(34):293–304, 2007.

J. A. Cunningham and I. Mendoza-Sanchez. Equivalence of two models for biodegradation during contaminant transport in groundwater. *Water Resour. Res.*, 42(2), 2006. doi: 10.1029/2005WR004205. URL dx.doi.org/10.1029/2005WR004205.

J. A. Cunningham, C. J. Werth, M. Reinhard, and P. V. Roberts. Effects of grain-scale mass transfer on the transport of volatile organics through sediments: 1. Model development. *Water Resour. Res.*, 33(12), 1997. doi: 10.1029/97WR02425. URL dx.doi.org/10.1029/97WR02425.

V. Cvetkovic and R. Haggerty. Transport with multiple-rate exchange in disordered media. *Physical Review E*, 65:051308, 2002.

V. Cvetković and S. Molin. Combining numerical simulations with time-domain random walk for pathogen risk assessment in groundwater. *Adv. Water Res.*, 36, 2012. doi: 10.1016/j.advwatres.2011.06.008. URL dx.doi.org/10.1016/j.advwatres.2011.06.008.

G. Dagan. *Flow and Transport in Porous Formations*. Springer-Verlag, New York, 1989. 465 p.

F. P. J. de Barros and A. Fiori. First-order based cumulative distribution function for solute concentration in heterogeneous aquifers: Theoretical analysis and implications for human health risk assessment. *Water Resour Res.*, 50, 2014. doi: 10.1002/2013WR015024. URL dx.doi.org/10.1002/2013WR015024.

F. P. J. de Barros and W. Nowak. On the link between contaminant source release conditions and plume prediction uncertainty. *Journal of contaminant hydrology*, 116(1-4), 2010. doi: 10.1016/j.jconhyd.2010.05.004. URL dx.doi.org/10.1016/j.jconhyd.2010.05.004.

F. P. J. de Barros and Y. Rubin. A risk-driven approach for subsurface site characterization. *Water Resour. Res.*, 44(1), 2008. doi: 10.1029/2007WR006081. URL dx.doi.org/10.1029/2007WR006081.

F. P. J. de Barros, Y. Rubin, and R. M. Maxwell. The concept of comparative information yield curves and its application to risk-based site characterization. *Water Resour. Res.*, 45(6), 2009. doi: 10.1029/2008WR007324. URL dx.doi.org/10.1029/2008WR007324.

F. P. J. de Barros, D. Fernàndez-Garcia, D. Bolster, and X. Sanchez-Vila. A risk-based probabilistic framework to estimate the endpoint of remediation: Concentration rebound by rate-limited mass transfer. *Water Resour. Res.*, 49, 2013. doi: 10.1002/wrcr.20171. URL http://dx.doi.org/10.1002/wrcr.20171.

M. De Simoni, J. Carrera, X. Sánchez-Vila, and A. Guadagnini. Time domain random walk method to simulate transport by advection-dispersion and matrix diffusion in fracture networks. *Geophys. Res. Lett.*, 28(21), 2001. doi: 10.1029/2001GL013698. URL http://dx.doi.org/10.1029/2001GL013698.

M. De Simoni, J. Carrera, X. Sánchez-Vila, and A. Guadagnini. A procedure for the solution of multicomponent reactive transport problems. *Water Resour. Res.*, 41, 2005.

M. Dentz. Concentration statistics for transport in heterogeneous media due to stochastic fluctuations of the center of mass velocity. *Adv. Water Resour.*, 36, 2014. doi: 10.1016/j.advwatres.2011.04.005. URL http://dx.doi.org/doi:10.1016/j.advwatres.2011.04.005.

M. Dentz and A. Castro. Effective transport dynamics in porous media with heterogeneous retardation properties. *Geophys. Res. Lett.*, 120, 2009. doi: 10.1029/2008GL036846. URL http://dx.doi.org/10.1029/2008GL036846.

M. Dentz, T. Le Borgne, A. Englert, and B. Bijeljic. Mixing, spreading and reaction in heterogeneous media: A brief review. *Journal of Contaminant Hydrology*, 120, 2011.

M. Dilley, R. S. Chen, U. Deichmann, A. L. Lerner-Lam, M. Arnold, P. Agwe, J.and Buys, O. Kjevstad, B. Lyon, and G. Yetman. *Natural Disaster Hotspots: A Global Risk Analysis, Disaster Risk Managment series n.5.* The World Bank Publications, Washington, D.C., WA., 2005.

D. Ding, D. A. Benson, A. Paster, and D. Bolster. Modeling bimolecular reactions and transport in porous media via particle tracking. *Adv. Water Resour.*, 53, 2013. doi: 10.1016/j.advwatres.2012.11.001. URL dx.doi.org/10.1016/j.advwatres.2012.11.001.

L. Donado, X. Sanchez-Vila, M. Dentz, J. Carrera, and D. Bolster. Multicomponent reactive transport in multicontinuum media. *Water Resour. Res.*, 45, 2009. doi: 10.1029/2008WR006823. URL http://dx.doi.org/doi:10.1029/2008WR006823.

Y. Edery, H. Scher, and B. Berkowitz. Modeling bimolecular reactions and transport in porous media. *Geophys. Res. Lett.*, 36, 2009. doi: 10.1029/2008GL036381. URL http://dx.doi.org/10.1029/2008GL036381.

Y. Edery, H. Scher, and B. Berkowitz. Particle tracking model of bimolecular reactive transport in porous media. *Water Resour. Res.*, 46, 2010. doi: 10.1029/2009WR009017. URL http://dx.doi.org/10.1029/2009WR009017.

Environmantal Protection Agency (EPA). Risk Assessment Guidance for SuperfundVolume 1: Human Health Manual (Part A). Rep. EPA/540/1-89/002, Office of Emergency and Remedial Response, U.S. Environmental Protection Agency, 1989.

Environmantal Protection Agency (EPA). Health Effects Assessment Summary Tables. Rep. FY1997 Update, Environmental Criteria and Assessment Office, Office of Health and Environmental Assessment, Office of Research and Development, Cincinnati, OH., 1997.

Environmantal Protection Agency (EPA). Anaerobic biodegradation rates of organic chemicals in groundwater: a summary of field and laboratory studies. Rep., Office of Solide Waste, Washington, DC., 1999.

Environmantal Protection Agency (EPA). Supplementary Guidance for Conducting Health Risk Assessment of Chemical Mixtures. Rep. EPA/630/R-00/002, U.S. Environmental Protection Agency, Washington, DC., 2000.

Environmantal Protection Agency (EPA). Technical protocol for evaluating natural attenuation of chlorinated solvents in ground water. Technical Report EPA/600/R-98/128, US EPA, 1998.

Environmantal Protection Agency (EPA). Calculation and use of first-order rate constants for monitored natural attenuation studies - Ground water issue. Rep. EPA/540/S-02/500, EPA, Washington D.C., 2002.

R. W. Falta, M. B. Stacy, A. N. M. Ahsanuzzaman, M. Wang, and R. C. Earle. Remediation evaluation model for chlorinated solvents. Remchlor user's manual, Center for Subsurface Modeling Support Ground Water and Ecosystems Restoration Division, US EPA R.S. Kerr Environmental Research Center, Ada, Oklahoma, 2002.

R. W. Falta, P. S. C. Rao, and N. Basu. Assessing the impacts of partial mass depletion in DNAPL source zones: I. Analytical modeling of source strength functions and plume response. *Journal of Contaminant Hydrology*, 78(4), 2005.

R.M. Fay and M.M. Mumtaz. Development of a priority list of chemical mixtures occurring at 1188 hazardous waste sites, using the hazdat database. *Food and Chemical Toxicology*, 34(1112), 1996.

C. E. Feehley, C. Zheng, and F. J. Molz. A dual-domain mass transfer approach for modeling solute transport in heterogeneous aquifers: Application to the Macrodisperison Experiment (MADE) site. *Water Resour. Res.*, 36(9), 2000.

D. E. Fennell, A. B. Carroll, J. M. Gossett, and S. H. Zinder. Assessment of indigenous reductive dechlorinating potential at a TCE-contaminated site using microcosms, polymerase chain reaction analysis, and site data. *Environ. Sci. Technol.*, 35(9), 2001.

Fernàndez-Garcia, G. Llerar-Meza, and J. J. Gmez-Hernndez. Upscaling transport with mass transfer models: Mean behavior and propagation of uncertainty. *Water Resour. Res.*, 45, 2009. doi: 10.1029/2009WR007764. URL dx.doi.org/10.1029/2009WR007764.

D. Fernàndez-Garcia and X. Sanchez-Vila. Optimal reconstruction of concentrations, gradients and reaction rates from particle distributions. *J. of Cont. Hydro.*, 2011.

D. Fernàndez-Garcia, X. Sanchez-Vila, and T. H. Illangasekare. Convergent-flow tracer tests in heterogeneous media: combined experimental-numerical analysis for determination of equivalent transport parameters. *Journal of Contaminant Hydrology*, 57(1-2), 2002.

D. Fernàndez-Garcia, T. H. Illangasekare, and H. Rajaram. Conservative and sorptive forced-gradient and uniform flow tracer tests in a three-dimensional laboratory test aquifer. *Water Resour. Res.*, 40, 2004. doi: 10.1029/2004WR003112. URL http://dx.doi.org/10.1029/2004WR003112.

D. Fernàndez-Garcia, T. H. Illangasekare, and H. Rajaram. Differences in the scale-dependence of dispersivity estimated from temporal and spatial moments in chemically and physically heterogeneous porous media. *Adv. Water Resour.*, 28(7), 2005a.

D. Fernàndez-Garcia, T. H. Illangasekare, and H. Rajaram. Differences in the scale-dependence of dispersivity and retardation factors estimated from forced-gradient and uniform flow tracer tests in three-dimensional physically and chemically heterogeneous porous media. *Water Resour. Res.*, 41, 2005b. doi: 10.1029/2004WR003125. URL http://dx.doi.org/10.1029/2004WR003125.

D. Fernàndez-Garcia, X. Sanchez-Vila, and A. Guadagnini. Reaction rates and effective parameters in stratified aquifers. *Adv. Water Resour.*, 31, 2008.

D. Fernàndez-Garcia, P. Trinchero, and X. Sanchez-Vila. Conditional stochastic mapping of transport connectivity. *Water Resour. Res.*, 46, 2010. doi: 10.1029/2009WR008533. URL dx.doi.org/10.1029/2009WR008533.

D. Fernàndez-Garcia, D. Bolster, X. Sanchez-Vila, and D. M. Tartakovsky. A Bayesian approach to integrate temporal data into probabilistic risk analysis of monitored NAPL remediation. *Advances in Resour. Res.*, 43, 2012.

A. Fiori and I. Jankovic. On preferential flow, channeling and connectivity in heterogeneous porous formations. *Math. Geosciences*, 44(2), 2012.

A. D. Fure, J. W. Jawitz, and M. D. Annable. DNAPL source depletion: Linking architecture and flux response. *Journal of Contaminant Hydrology*, 85, 2006.

Liu G., C. Zheng, and S. Gorelick. Limits of applicability of the advection- dispersion model in aquifers containing connected high-conductivity channels. *Water Resour. Res.*, 40, 2004.

L. W. Gelhar. *Stochastic Subsurface Hydrology*. Prentice-Hall, Upper Saddle River, N. J., 1993. 390 pp.

L. W. Gelhar, C. Welty, and K. Rehfeldt. A critical review of data on field-scale dispersion aquifers. *Water Resour Res.*, 28(7), 1992.

D. Gillespie. A general method for numerically simulating the stochastic time evolution of coupled chemical reactions. *J. Comput. Phys.*, 22, 1976.

J. J. Gómez-Hernández. Complexity. *Groundwater*, 44, 2006. doi: 10.1111/j.1745-6584.2006.00222.x. URL http://dx.doi.org/doi:10.1111/j.1745-6584.2006.00222.x.

J. J. Gomez-Hernandez and X. Wen. To be or not to be multi-Gaussian? a reflection on stochastic hydrogeology. *Adv. Water Resour.*, 21(1), 1998.

P. Gouze, T. Le Borgne, R. Leprovost, G. Lods, T. Poidras, and P. Pezard. Non-Fickian dispersion in porous media: 1. Multiscale measurements using single-well injection withdrawal tracer tests. *Water Resour. Res.*, 44, 2008. doi: 10.1029/2007WR006278. URL http://dx.doi.org/10.1029/2007WR006278.

R. Haggerty. STAMMT-L: Solute Transport and Multirate Mass Transfer, Version 3.0. User's manual ERMS549160, Oregon State University, 2009.

R. Haggerty and S. M. Gorelick. Multiple-rate mass transfer for modeling diffusion and surface reactions in media with pore-scale heterogeneity. *Water Resour. Res.*, 31(10), 1995.

R. Haggerty, S. A. McKenna, and L. C. Meigs. On the late-time behaviour of tracer test breakthrough curves. *Water Resour. Res.*, 36, 2000.

R. Haggerty, C. F. Harvey, C. Freiherr von Schwerin, and L. C. Meigs. What controls the apparent timescale of solute mass transfer in aquifers and soils? A comparison of experimental results. *Water Resour. Res.*, 40, 2004. doi: 10.1029/2002WR001716. URL dx.doi.org/10.1029/2002WR001716.

A. Harbaugh, E. Banta, M. Hill, and M. McDonald. MODFLOW 2000 the US Geological Survey Modular ground-water model-user guide to modularization concepts and the ground-water flow process. Open File 00-92, 121pp., Rep. U.S. Geol. Surv., 2000.

C. Harvey and S. M. Gorelick. Rate-limited mass transfer or macrodispersion : Which dominates plume evolution at the Macrodispersion Experiment (MADE) site? *Water Resour. Res.*, 36(3), 2000.

Z. C. Haston and P. L. McCarty. Chlorinated ethene half-velocity coefficients (Ks) for Reductive dehalogenation. *Environ. Sci. Technol.*, 33, 1999.

C. V. Henri and D. Fernàndez-Garcia. Toward efficiency in heterogeneous multi-species reactive transport modeling: A particle-tracking solution for first-order network reactions. *Water Resour. Res.*, 50, 2014. doi: 10.1002/2013WR014956. URL dx.doi.org/10.1002/2013WR014956.

C. V. Henri, D. Fernandez-Garcia, and F. P. J. de Barros. Probabilistic human health risk assessment of degradation-related chemical mixtures in heterogeneous aquifers: Risk statistics, hot spots and preferential channels. *Water Resour. Res. (accepted)*, 2015.

E. Hoehn, J. Eikenberg, T. Fierz, W. Drost, and E. Reichlmayr. The Grimsel migration experiment: Field injection-withdrawal experiments in fractured rock with sorbing tracers. *J. Contam. Hydrol.*, 34, 1998.

H. Huang and B. X. Hu. Nonlocal nonreactive transport in heterogeneous porous media with interregional mass diffusion. *Water Resour. Res.*, 36(7), 2000.

H. Huang, A. E. Hassan, and B. X. Hu. Monte Carlo study of conservative transport in heterogeneous dual-porosity media. *Journal of Hydrology*, 275, 2003.

M. K. Jain and C. S. Criddle. *Metabolism and cometabolism of halogenated C-1 and C-2 hydrocarbon, in Biotransformations: Microbial Degradation of Health Risk Compounds.* Elsevier Sci., New York, 1995. edited by V. P.Singh, pp. 65–112.

B. R. James and S. M. Gorelick. When enough is enough: The worth of monitoring data in aquifer remediation design. *Water Resour. Res.*, 30(12), 1994. doi: 10.1029/94WR01972. URL dx.doi.org/10.1029/94WR01972.

I. Janković and A. Fiori. Analysis of the impact of injection mode in transport through strongly heterogeneous aquifers. *Adv. Water Resour.*, 33(10), 2010. doi: 10.1016/j.advwatres.2010.05.006. URL dx.doi.org/10.1016/j.advwatres.2010.05.006.

J. Jarsj, M. Bayer-Raich1, and T. Ptak. Monitoring groundwater contamination and delineating source zones at industrial sites: Uncertainty analyses using integral pumping tests. *J. Contam. Hydrol.*, 79(3-4), 2005. doi: 10.1016/j.jconhyd.2005.05.011. URL dx.doi.org/10.1016/j.jconhyd.2005.05.011.

V. Kapoor and L. W. Gelhar. Transport in three-dimensionally heterogeneous aquifers: 1. Dynamics of concentration fluctuations. *Water Resour. Res.*, 30(6), 1994.

W. Kinzelbach. The random walk method in pollutant transport simulation, Advances in Analytical and Numerical Groundwater Flow and Quality Modelling, Editor: E. Custodio et al. *NATO ASI Series C*, 224, 1987.

P. K. Kitanidis. Prediction by the mothod of moments of transport in a heterogeneous formation. *J. Hydrol.*, 102, 1988.

P. K. Kitanidis. Particle tracking equations for the solution of the advection-dispersion equation with variable coefficients. *Water Resour. Res.*, 30(11), 1994.

P. K. Kitanidis and P. L. McCarty. *Delivery and Mixing in the Subsurface: Processes and Design Principles for In Situ Remediation (Vol. 4).* Springer, New York, NY, USA, 2012. 325 p.

C. Knudby and J. Carrera. On the use of apparent hydraulic diffusivity as an indicator of connectivity. *Journal Of Hydrology*, 28(3-4), 2006.

C. Knudby and J. S. Carrera. On the relationship between indicators of geostatistical, flow and transport connectivity. *Adv. Water Resour.*, 28(4), 2005.

J. Koch and W. Nowak. Predicting DNAPL mass discharge and contaminated site longevity probabilities: Conceptual model and high-resolution stochastic simulation. *Water Resour. Res.*, 51, 2015. doi: 10.1002/2014WR015478. URL dx.doi.org/10.1002/2014WR015478.

S. Kräutle and P. Knabner. A new numerical reduction scheme for fully coupled multicomponent transport-reaction problems in porous media. *Water Resour. Res.*, 41, 1994.

B. H. Kueper, W. Abbott, and G. Farquhar. Experimental observations of multiphase flow in heterogeneous porous media. *Journal of Contaminant Hydrology*, 5(1), 1989. doi: 10.1016/0169-7722(89)90007-7. URL dx.doi.org/10.1016/0169-7722(89)90007-7.

T. G. Kurtz. The relationship between stochastic and deterministic models for chemical reactions. *The Journal of Chemical Physiscs*, 57(7), 2003.

E. M. LaBolle, G. E. Fogg, and A. F. B. Tompson. Random-walk simulation of transport in heterogeneous porous media: Local mass-conservation problem and implementation methods. *Water Resour. Res.*, 32(3), 1996.

G. F. Lawler. *Introduction to stochastic processes*. Chapman and Hall/CRC, Taylor and Francis Group, 2006. 234 p.

D. R. LeBlanc, S. P. Garabedian, K. M. Hess, L. W. Gelhar, R. D. Quadri, K. G. Stollenwerk, and W. W. Wood. Large-scale natural gradient tracer test in sand and gravel, Cape Cod, Massachusetts: 1. Experimental design and observed tracer movement. *Water Resour Res.*, 27(5), 1991.

Z. Li and M. L. Brusseau. Nonideal transport of reactive solutes in heterogeneous porous media: 6. Microscopic and macroscopic approaches for incorporating heterogeneous rate-limited mass transfer. *Water Resour. Res.*, 36(10), 2000.

P. C. Lichtner, S. Kelkar, and B. Robinson. New form of dispersion tensor for axisymmetric porous media with implementation in particle tracking. *Water Resour. Res.*, 38, 2002. doi: 10.1029/2000WR000100. URL dx.doi.org/10.1029/2000WR000100.

C. Llopis-Albert and J. E. Capilla. Gradual conditioning of non-Gaussian transmissivity fields to flow and mass transport data. 3. Application to the macrodispersion experiment

(MADE-2) site, on Columbus Air Force Base in Mississippi (USA). *J. Hydrol.*, 371(14), 2009.

C. Lu, P. L. Bjerg, F. Zhang, and M. M. Broholm. Sorption of chlorinated solvents and degradation products on natural clayey tills. *Chemosphere*, 83(11), 2011.

Dentz M. and B. Berkowitz. Transport behavior of a passive solute in con- tinuous time random walks and multirate mass transfer. *Water Resour. Res.*, 39(5), 2003.

J. A. MacDonald. Evaluating natural attenuation for groundwater cleanup. *Environ. Sci. Technol.*, 34(15), 2000.

D. M. Mackay, D. L. Freyberg, P. V. Roberts, and J. A. Cherry. A natural gradient experiment on solute transport in a sand aquifer: 1. Approach and overview of plume movement. *Water Resour Res.*, 22(13), 1986.

A.P. Mallawatantri, B.G. McConkey, and D.J. Mulla. Characterization of pesticide sorption and degradation in macropore linings and soil horizons of Thatuna silt loam. *J. Environ. Qual.*, 25, 1996.

R. M. Maxwell and W. E. Kastenberg. Stochastic environmental risk analysis: an integrated methodology for predicting cancer risk from contaminated groundwater. *Stochastic Environmental Research and Risk Assessment*, 13(1-2), 1999. doi: 10.1007/s004770050030. URL http://dx.doi.org/10.1007/s004770050030.

R. M. Maxwell, W. E. Kastenberg, and Y. Rubin. A methodology to integrate site characterization information into groundwater-driven health risk assessment. *Water Resour. Res.*, 35(9), 1999.

R. M. Maxwell, S. F. Carle, and A. F. B. Tompson. Contamination, risk, and heterogeneity: on the effectiveness of aquifer remediation. *Environmental Geology*, 54(8), 2008. doi: 10.1007/s00254-007-0955-8. URL http://dx.doi.org/10.1007/s00254-007-0955-8.

P. L. McCarty. Breathing with Chlorinated Solvents. *Science*, 276(5318), 1997. doi: 10.1126/science.276.5318.1521. URL dx.doi.org/10.1126/science.276.5318.1521.

T. M. McGuire, C. J. Newell, B. B. Looney, K. M. Vangelas, and C. H. Sink. Historical analysis of monitored natural attenuation: A survey of 191 chlorinated solvent sites

and 45 solvent plumes. *Remediation*, 15(1), 2004. doi: 10:1002/rem.20036. URL dx.doi.org/10:1002/rem.20036.

A. M. Michalak and P. K. Kitanidis. Macroscopic behavior and random-walk particle tracking of kinetically sorbing solutes. *Water Resour. Res.*, 36(8), 2000.

F. Miralles-Wilhelm and L. W. Gelhar. Stochastic analysis of sorption macrokinetics in heterogeneous aquifers. *Water Resour. Res.*, 32(6), 1996. doi: 10.1029/96WR00791. URL http://dx.doi.org/10.1029/96WR00791.

F. Miralles-Wilhelm, L. W. Gelhar, and V. Kapoor. Stochastic analysis of oxygen-limited biodegradation in three-dimensionally heterogeneous aquifers. *Water Resour. Res.*, 33 (6), 1997.

B. K. Mishra and C. Mishra. Kinetics of nitrification and nitrate reduction during leaching of ammonium nitrate through a limed Ultisol profile. *J. Indian Soc. Soil Sci.*, 39, 1991.

C. Moler and C. van Loan. Nineteen dubious ways to compute the exponential of a matrix, twenty-five years later. *SIAM Rev.*, 45(1), 2003.

S. Molins, J. Carrera, C. Ayora, and M. W. Saaltink. A formulation for decoupling components in reactive transport problems. *Water Resour. Res.*, 40, 2004. doi: 10.1029/2003WR002970. URL http://dx.doi.org/10.1029/2003WR002970.

E. Morin. *Introduction la pense complexe.* Points, Paris, France, 1990.

I. Neretnieks. Diffusion in rock matrix: An important factor in radionuclide retardation? *J. Geophys. Res.*, 85, 1980.

J. W. E. Page, K. Soga, and T. Illangasekare. The significance of heterogeneity on mass flux from DNAPL source zones: An experimental investigation. *J. Contam. Hydrol.*, 94(3-4), 2007. doi: 10.1016/j.jconhyd.2007.06.004. URL dx.doi.org/10.1016/j.jconhyd.2007.06.004.

S. Painter, V. Cvetkovic, J. Mancillas, and O. Pensado. Time domain particle tracking methods for simulating transport with retention and first-order transformation. *Water Resour. Res.*, 44, 2008.

J. Palanichamy, T. Becker, M. Spiller, J. Kngeter, and S. Mohan. Time domain particle tracking methods for simulating transport with retention and first-order transformation. *Comput. Visual. Sci.*, 2007. doi: 10.1007/s00,791-007-0080-y. URL http://dx.doi.org/10.1007/s00,791-007-0080-y.

P. Panagos, M. Van Liedekerke, Y. Yigini, and L. Montanarella. Contaminated Sites in Europe: Review of the Current Situation Based on Data Collected through a European Network. *Journal of Environmental and Public Health*, 2013, 2013. doi: 10.1155/2013/158764. URL dx.doi.org/10.1155/2013/158764.

J. F. Pankow and J. A. Cherry. *Dense chlrorinated Solvents and other DNAPLS in groundwater*. Waterloo Press, Portland, OR, 1996.

J. C. Parker and E. Park. Modeling field-scale dense nonaqueous phase liquid dissolution kinetics in heterogeneous aquifers. *Water Resour. Res.*, 40, 2004.

J. C. Parker and M. T. van Genuchten. Flux-averaged and volume-averaged concentrations in continuum approaches to solute transport. *Water Resour. Res.*, 20(7), 1984. doi: 10.1029/WR020i007p00866. URL dx.doi.org/10.1029/WR020i007p00866.

A. Paster, D. Bolster, and D. Benson. Connecting the dots: Semi-analytical and random walk numerical solutions of the diffusion-reaction equation with stochastic initial conditions. *Journal of Computational Physics*, 263, 2014.

D. Pedretti and D. Fernàndez-Garcia. An automatic locally-adaptive method to estimate heavily-tailed breakthrough curves from particle distributions. *Adv. Water Resour.*, 59, 2013.

D. Pedretti, D. Fernàndez-Garcia, D. Bolster, and X. Sanchez-Vila. On the formation of breakthrough curves tailing during convergent flow tracer tests in three-dimensional heterogeneous aquifers. *Water Resour. Res.*, 49, 2013. doi: 10.1002/wrcr.20330. URL dx.doi.org/10.1002/wrcr.20330.

B.E. Pivetz and T.S. Steenhuis. Soil matrix and macropore biodegradation of 2,4-D. *J. Environ. Qual.*, 24(4), 1995.

H. Rajaram. Time and scale dependent effective retardation factors in heterogeneous aquifers. *Adv. Water Resour.*, 20(4), 1997.

H. Rajaram and L. W. Gelhar. Plume scale-dependent dispersion in heterogeneous aquifers: 2. Eulerian analysis and three-dimensional aquifers. *Water Resour. Res.*, 29(9), 1993.

P. S. C. Rao and J. W. Jawitz. Comment on "Steady state mass transfer from single-component dense nonaqueous phase liquids in uniform flow fields" by T. C. Sale and D. B. McWhorter. *Water Resour. Res.*, 39(3), 2003. doi: 10.1029/2001WR000599. URL dx.doi.org/10.1029/2001WR000599.

P. S. C. Rao, D. E. Rolston, R. E. Jessup, and J. M. Davidson. Solute transport in aggregated porous media: Theoretical and experimental evaluation. *Soil Sci. Soc. Am.*, 44, 1980.

P. S. C. Rao, J. W. Jawitz, C. G. Enfield, R. Falta, M. D. Annabel, and A. L. Wood. Technology integration for contaminated site remediation: cleanup goals and performance metrics. *Ground Water QualitySheffield*, 2001.

K. R. Rehfeldt, J. Mark Boggs, and L. W. Gelhar. Field Study of Dispersion in a Heterogeneous Aquifer 3. Geostatistical Analysis of Hydraulic Conductivity. *Water Resour. Res.*, 28(12), 1992.

P. Renard and D. Allard. Connectivity metrics for subsurface flow and transport. *Advances in Water Resources*, 51, 2013.

B. E. Rittmann and P. L. McCarty. Model of steady state-biofilm kinetics. *Biotechnol. Bioeng.*, 22(11), 1980.

M. Riva, A. Guadagnini, D. Fernandez-Garcia, X. Sanchez-Vila, and T. Ptak. Relative importance of geostatistical and transport models in describing heavily tailed breakthrough curves at the Lauswiesen site. *Journal of Contaminant Hydrology*, 101, 2008.

P. V. Roberts, M.N. Goltz, and D. M. Mackay. A Natural Gradient Experiment on Solute Transport in a Sand Aquifer 3. Retardation Estimates and Mass Balances for Organic Solutes. *Water Resour Res.*, 22(13), 1986.

C. Rodak and S. Silliman. Probabilistic risk analysis and fault trees: initial discussion of application to identification of risk at a wellhead. *Adv. Water Resour.*, 36, 2012.

S. M. Ross. *Introduction to probability models*. Academic Press, Oxford, 2003. 8th ed., 755 pp.

Y. Rubin. *Applied Stochastic Hydrogeology*. Oxford Univ. Press, Oxford, 2003.

Y. Rubin, A. Bellin, and M. Cushey. Modeling of transport in ground water for environmental risk assessment. *Stochastic Hydrol. Hydraul.*, 8(1), 1994. doi: 10.1007/BF01581390. URL dx.doi.org/10.1007/BF01581390.

S. Rubol, A. Freixa, A. Carles-Brangari, A.M. Fernàndez-Garcia D. and, Romani, and X. Sanchez-Vila. Connecting bacterial colonization to physical and biochemical changes in a sand box infiltration experiment. *J. of Hydrology*, 517, 2014.

M. W. Saaltink, F. Batlle, C. Ayora, J. Carrera, and S. Olivella. RETRASO, a code for modeling reactive transport in saturated and unsaturated porous media. *Geol. Acta*, 2 (3), 2004.

P. Salamon, D. Fernàndez-Garcia, and J. J. Gómez-Hernández. A review and numerical assessment of the random walk particle tracking method. *J. of Contaminant Hydrology*, 87, 2006a.

P. Salamon, D. Fernàndez-Garcia, and J. J. Gómez-Hernández. Modeling mass transfer processes using random walk particle tracking. *Water Resour. Res.*, 42, 2006b. doi: doi:101029/2006WR004927. URL http://dx.doi.org/doi:101029/2006WR004927.

P. Salamon, D. Fernàndez-Garcia, and J. J. Gómez-Hernández. Modeling tracer transport at the made site: The importance of heterogeneity. *Water Resour. Res.*, 43, 2007.

T. C. Sale and D. B. McWhorter. Steady state mass transfer from single-component dense nonaqueous phase liquids in uniform flow fields. *Water Resour. Res.*, 37(2), 2001. doi: 10.1029/2000WR900236. URL dx.doi.org/10.1029/2000WR900236.

X. Sanchez-Vila, J. Carrera, and J. Girardi. Modeling tracer transport at the made site: The importance of heterogeneity. *J. Hydrol.*, 183(1), 1996.

X. Sanchez-Vila, P. M. Meier, and J. Carrera. Pumping tests in heterogeneous aquifers: An analytical study of what can be obtained from their interpretation using jacob's method. *Water Resour Res.*, 35(4), 1999.

X. Sanchez-Vila, A. Guadagnini, and D. Fernàndez-Garcia. Conditional probability density functions of concentrations for mixing-controlled reactive transport in heterogeneous aquifers. *Mathematical Geosciences*, 41(3), 2008.

X. Sanchez-Vila, D. Fernàndez-Garcia, and A. Guadagnini. Interpretation of column experiments of transport of solutes undergoing an irreversible bimolecular reaction using a continuum approximation. *Water Resour. Res.*, 46, 2010. doi: 10.1029/2010WR009539. URL http://dx.doi.org/10.1029/2010WR009539.

S. K. Sandrin, M. L. Brusseau, J. J. Piatt, A. A. Boudour, W. J. Blanford, , and N. T. Nelson. Spatial variability of in situ microbial activity: biotracer tests. *Ground Water*, 42(3), 2004.

M. A. Scholl. Effects of heterogeneity in aquifer permeability and biomass on biodegradation rate calculations-Results from numerical simulations. *Ground Water*, 38(5), 2000.

E. R. Siirila and R. M. Maxwell. Evaluating effective reaction rates of kinetically driven solutes in large-scale, statistically anisotropic media: Human health risk implications. *Water Resour. Res.*, 48(4), 2012. doi: 10.1029/2011WR011516. URL dx.doi.org/10.1029/2011WR011516.

E. R. Siirila, A. K. Navarre-Sitchler, R. M. Maxwell, and J. E. McCray. A quantitative methodology to assess the risks to human health from CO2 leakage into groundwater. *Adv. Water Resour.*, 36, 2014.

R. S. Skeen, J. Gao, and B. S. Hooker. Kinetics of chlorinated ethylene dehalogenation under methanogenic conditions. *Biotechnol. Bioeng.*, 48, 1995.

J.B. Smalley, B.S. Minsker, and D.E. Goldberg. Risk-based in situ bioremediation design using a noisy genetic algorithm. *Water Resour Res.*, 36(10), 2000.

B. T. Smith, J. M. Boyle, J. J. Dongarra, B. S. Garbow, Y. Ikebe, V. C. Klema, and C. B. Moler. Matrix Eigensystem Routines: EISPACK Guide, 2nd ed. Lecture notes in comput. sci., Springer-Verlag, New York, 1976.

K. Soga, J. Page, and T. Illangasekare. A review of NAPL source zone remediation efficiency and the mass flux approach. *J. Hazard. Mater.*, 110(13), 2004.

A. J. Speek. Lifespan oral toxicity study of vinyl chloride in rats. *Food Cosmet. Toxicol.*, 19(3), 1981.

H. F. Stroo, A. Leeson, J. A. Marqusee, P. C. Johnson, C. H. Ward, M. C. Kavanaugh, T. C. Sale, Ch. J. Newell, K. D. Pennell, C. A. Lebrón, and M. Unger. Chlorinated Ethene Source Remediation: Lessons Learned. *Environ. Sci. Technol.*, 46, 2012. doi: 10.1021/es204714w. URL dx.doi.org/10.1021/es204714w.

Y. Sun and T. A. Buscheck. Analytical solutions for reactive transport of N-member radionuclide chains in a single fracture. *Journal of Contaminant Hydrology*, 62–63, 2003. doi: 10.1016/S0169-7722(02)00181-X. URL dx.doi.org/10.1016/S0169-7722(02)00181-X.

Y. Sun, J. N. Petersen, T. P. Clement, and R. S. Skeen. Development of analytical solutions for multispecies transport with serial and parallel reactions. *Water Resour. Res.*, 35(1), 1999.

A. Tamir. *Applications of Markov chains in chemical engineering*. Elsevier, 1998. 604 p.

D. M. Tartakosky. Probabilistic risk analysis in subsurface hydrology. *Geophysical Research Letters*, 34(5), 2007. doi: 10:1029/2007GL029245. URL dx.doi.org/10:1029/2007GL029245.

A. F. B. Tompson, A. L. Schafer, and R. W. Smith. Impacts of physical and chemical heterogeneity on contaminant transport in sandy porous medium. *Water Resour Res.*, 32(4), 1996.

A.F.B Tompson. Numerical simulation of chemical migration in physically and chemically heterogeneous porous media. *Water Resour Res.*, 29(11), 1993.

A.F.B Tompson and L. W. Gelhar. Numerical simulation of solute transport in three-dimensional, randomly heterogeneous porous media. *Water Resour Res.*, 26(10), 1990.

P. Trinchero, X. Sanchez-Vila, and D. Fernàndez-Garcia. Point-to-point connectivity, an abstract concept or a key issue for risk assessment studies? *Adv. Water Resour.*, 31, 2008.

M. Troldborg, W. Nowak, N. Tuxen, P. L. Bjerg, R. Helmig, and P. J. Binning. Uncertainty evaluation of mass discharge estimates from a contaminated site using a fully Bayesian framework. *Water Resour. Res.*, 46, 2010. doi: 10.1029/2010WR009227. URL dx.doi.org/10.1029/2010WR009227.

Y. W. Tsang and C. F. Tsang. A particle-tracking method for advective transport in fractures with diffusion into finite matrix blocks. *Water Resour. Res.*, 37(3), 2001a.

Y. W. Tsang and C. F. Tsang. A particle-tracking method for advective transport in fractures with diffusion into finite matrix blocks. *Water Resour. Res.*, 37(3), 2001b.

UNESCO. Groundwater and global changes: trends, oportunities and challenges. Side publication, United Nations Educational, Scientific and Cultural Organization, Paris, France, 2012.

A. Valocchi and H. A. M. Quinodoz. Application of the random walk method to simulate the transport of kinetically adsorbing solutes. *Groundwater Contamination*, 185, 1989.

M. T. van Genuchten. Convective-dispersive transport of solutes involved in sequential first-order decay reactions. *Comput. Geosci.*, 11(2), 1985.

M. T. van Genuchten and P. J. Wierenga. Mass transfer studies in sorbing porous media. *Soil Sci. Soc. Am. J.*, 1976.

J. Vanderborght, D. Mallants, and J. Feyen. Solute transport in a heterogeneous soil for boundary and initial conditions: Evaluation of first-order approximations. *Water Resour. Res.*, 34, 1998.

F.P. Vinther, F. Eiland, A.M. Lind, and L. Elsgaard. Microbial biomass and numbers of denitrifiers related to macropore channels in agricultural and forest soils. *Soil Biol. Biochem.*, 31(4), 1999.

H. S. Vishwanathan, B. A. Robinson, A. J. Valocchi, and I. R. Triay. A reactive transport model of Neptunian migration from a potential repository at Yucca Mountain. *J. Hydrol.*, 209, 1998.

T. M. Vogel, C. S. Criddle, and P. L. McCarty. Transformations of halogenated aliphatic compounds. *Environ. Sci. Technol.*, 21(8), 1987.

X. H. Wen and J. J. Gómez-Hernández. The constant displacement scheme for tracking particles in heterogeneous aquifers. *Ground Water*, 34(1), 1996.

M. Willmann, G. W. Lanyon, P. Marschall, and W. Kinzelbach. A new stochastic particle-tracking approach for fractured sedimentary formations. *Water Resour. Res.*, 49, 2013. doi: 10.1029/2012WR012191. URL dx.doi.org/10.1029/2012WR012191.

World Health Organization. *Protecting Groundwater for Health Managing the quality of Drinking-water sources*. IWA Publishing, London, UK, 2006. ISBN: 1843390795.

D. F. Young and W. P. Ball. Effects of column conditions on the first-orde rate modeling of nonequilibrium solute breakthrough. *Water Resour. Res.*, 31(9), 1995.

K. Zhang and A. D. Woodbury. A Krylov finite element approach for multispecies contaminant transport in discretely fractured porous media. *Adv. Water Resour.*, 25, 2002.

Y. Zhang and D. A. Benson. Lagrangian simulation of multidimensional anomalous transport at the MADE site. *Geophys. Res. Lett.*, 35, 2008. doi: 10.1029/2008GL033222. URL dx.doi.org/10.1029/2008GL033222.

J. Zhu and J. F. Sykes. Simple screening models of NAPL dissolution in the subsurface. *Journal of Contaminant Hydrology*, 72, 2004.

B. Zinn and C. F. Harvey. When good statistical models of aquifer heterogeneity go bad: A comparison of flow, dispersion, and mass transfer in connected and multivariate Gaussian hydraulic conductivity fields. *Water Resour. Res.*, 39(3), 2003. doi: 10.1029/2001WR001146. URL dx.doi.org/10.1029/2001WR001146.